Max Planck Institut für Physik komplexer Systeme

DYNAMICS OF BACTERIAL AGGREGATES

Theory guided by experiments

Dissertation
zur Erlangung des akademische Grades
Doctor rerum naturalium

Institut für Theoretische Physik
Fakultät für Mathematik und Naturwissenschaften
Technische Universität Dresden

vorgelegt von

WOLFRAM PÖNISCH

Dresden, 2018

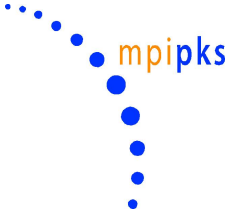

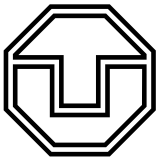

TECHNISCHE
UNIVERSITÄT
DRESDEN

GUTACHTER:

- Prof. Dr. F. Jülicher & Prof. Dr. St. Grill
- Prof. Dr. G. Koenderink

EINGEREICHT AM:
11. September 2017

PROMOTIONSKOMMISSION:

- Prof. Dr. S. Reineke (Vorsitz)
- Prof. Dr. F. Jülicher
- Prof. Dr. St. Grill
- Prof. Dr. G. Koenderink
- Prof. Dr. E. Hieckmann

VERTEIDIGT AM:
18. April 2018

ORT:
Dresden

SUMMARY

The majority of bacteria are organized in surface-associated communities, the so called biofilms. Crucial processes that drive the formation of such biofilms are the motility of bacteria on a substrate, enabling cells to reach each others vicinity, and attractive cell-cell-interactions, driving the formation of microcolonies. These colonies, aggregates consisting of thousands of cells, are the precursors of biofilms.

In this thesis we investigate the role of cell appendages, called type IV pili, in the substrate motion of bacteria and the formation of bacterial microcolonies. Therefore, we study the bacterial dynamics with the help of experiments and theoretical models.

We introduce a novel simulation tool in the tradition of Brownian dynamics simulations. In this computational model, that was developed alongside experimental observations, we study how explicit pili dynamics, pili-substrate and pili–pili interactions drive the cell dynamics. First, we apply our model to investigate how individual cells move on a substrate due to cycles of protrusion and retraction of type IV pili. We show that the characteristic features, in particular persistent motion, can solely originate from collective interactions of pili. Next, we perform experiments to study the coalescence of bacterial microcolonies. With the help of experiments and our computational model, we identify a spatially-dependent gradient of motility of cells within the colony as the origin of a separation of time scale, a feature which is in disagreement with the coalescence dynamics of fluid droplets. Additionally, we show that altering the force generation of pili can cause demixing of cells within bacterial aggregates. Finally, we combine our knowledge of the substrate motion of cells and of the pili-mediated interactions of colonies to identify the main processes (aggregation, fragmentation and cell divisions) that drive assembly of colonies. Starting from experiments, we develop a mathematical model and observe excellent qualitative and quantitative agreement to experimental data of the density of colonies of different sizes.

In summary, hand in hand with experiments, we develop theoretical frameworks to unravel the role of type IV pili in bacterial surface motility, microcolony dynamics and colony formation.

ZUSAMMENFASSUNG

Die Mehrzahl der Bakterien sind organisiert in sogenannten Biofilmen, Ansammlungen von Zellen assoziert mit den unterschiedlichsten Oberflächen. Wichtige Prozesse, die die Bildung solcher Biofilme antreiben, sind die Bewegung einzelner Zellen über die Oberfläche, so dass sich auch weit entfernte Zellen in direkte Nachbarschaft bringen können, sowie anziehende Interaktionen zwischen Zellen, welche die Bildung von Mikrokolonien verursachen. Solche Kolonien können aus tausenden einzelnen Zellen bestehen und sind der Startpunkt für die Bildung eines Biofilms.

In dieser Arbeit untersuchen wir die Rolle von Zellfortsätzen, den sogenannten Typ IV Pili, in beiden Prozessen, der Bewegung über eine Oberfläche und der Bildung von Kolonien. Dafür studieren wir die Dynamik von Bakterien mithilfe von Experimenten und theoretischen Modellen.

Wir haben ein neuartiges numerisches Werkzeug entwickelt, dass es uns erlaubt, die Zelldynamik resultierend aus der expliziten Dynamik von Pili, den durch Pili verursachten Kräfte und den direkten Pili-Pili-Interaktionen zu studieren.

Zuerst wenden wir dieses Modell an um die Bewegung einzelner Zellen auf einer Oberfläche zu untersuchen und erklären, wie die kollektive Dynamik mehrerer Pili charakteristische Eigenschaften der Oberflächenbewegung erzeugen. Insbesondere erklären wir, wie persistente Bewegung der Zellen entstehen kann.

Daraufhin führen wir Experimente durch um die Koaleszenz von bakteriellen Mikrokolonien zu studieren. Mithilfe dieser Experimente und durch Vergleiche mit Simulationen können wir eine ortsabhängigen Gradienten der Zellbewegung innerhalb von Kolonien als Ursache einer Trennung der Zeitskalen der Koaleszenz erklären. Solch ein Verhalten ist nicht mit der Dynamik von viskosen Tropfen zu erklären ist. Weiterhin zeigen wir, wie Änderungen der Krafterzeugung innerhalb der Zellen zur Entmischung von Zellpopulationen innerhalb von Kolonien führen kann.

Zuletzt kombinieren wir unser gewonnenes Wissen über die Bewegung von Zellen auf einer Oberfläche und der Dynamik bzw. den Interaktionen von Mikrokolonien, um die Bildung von Kolonien zu untersuchen. Wir sind in der Lage, die wichtigsten involvierten Prozesse zu identifizieren. Ein eigens entwickeltes mathematischen Modells bietet exzellente qualitative und quantitative Übereinstimmung zum Experiment.

In dieser Arbeit entwickeln wir Hand in Hand mit Experimenten verschiedenste theoretische Modelle um die Rolle von Typ IV Pili während der bakteriellen Bewegung, der Koloniebildung und der Dynamik von Kolonien zu erklären.

LIST OF PUBLICATIONS

PUBLISHED

- V. Zaburdaev and **W. Pönisch**. "Bakterielle Mikrokolonien als frühe Formen multizellulärer Organismen". In: *Forschungsbericht 2017 – Max-Planck-Institut für Physik komplexer Systeme, Dresden. DOI: 10.17617/1.5Q.*
- **W. Pönisch**, C.A. Weber, G. Juckeland, N. Biais, and V. Zaburdaev. "Multiscale modeling of bacterial colonies: how pili mediate the dynamics of single cells and cellular aggregates". In: *New Journal of Physics* 19.1 (2017), p. 015003. DOI: 10.1088/1367-2630/aa5483.
- **W. Pönisch** and V. Zaburdaev. "Relative distance between tracers as a measure of diffusivity within moving aggregates". In: *European Physical Journal B* 91.27 (2018). DOI: 10.1140/epjb/e2017-80347-5.

PREPRINTS

- **W. Pönisch**, K. Eckenrode, K. Alzurqa, H. Nasrollahi, C.A. Weber, V. Zaburdaev, and N. Biais. "Pili mediated intercellular forces shape heterogeneous bacterial microcolonies prior to multicellular differentiation". In: *arXiv preprint arXiv:* 1703.09659 (2017).

IN PREPARATION

- **W. Pönisch**, C.A. Weber, N. Biais, V. Zaburdaev. "Colony formation of bacterial aggregates".
- **W. Pönisch**, C.A. Weber and V. Zaburdaev. "How bacterial cells and colonies move on solid substrates".

ACKNOWLEDGEMENTS

First, I would like to thank Vasily Zaburdaev for giving me the opportunity to work on this project and for his constant and helpful supervision. Whenever I had a problem, his office door was open and we could discuss any scientific question. Additionally, I am grateful to Vasily for allowing me to follow my own ideas.
I would like to thank Frank Jülicher for creating the great scientific environment that we have a the Max Planck Institute for the Physics of Complex Systems and for allowing me to be part of it.
I am grateful to countless fruitful discussions with Christoph Weber and many fresh ideas that helped me to understand my project.
I also want to thank my experimental collaborator Nicolas Biais for allowing me to visit his lab at the Brooklyn College and to make my hands dirty. I also want to thank all people I met while working in his lab and that helped me whenever I had a problem, especially Hadi, Ingrid, Khaled, Kelly and Luis.
I am thankful to Stefan Diez for being a member of my TAC committee and for helpful discussions during our TAC meetings. Thanks also go to the support from the IMPRS CellDevoSys of the MPI-PKS and the MPI-CBG.
I also want to thank Guido Juckeland for inviting me to the GPU-Hackathon and for helping me to understand the numerical limitations of my model.
Of course, big thanks go to the "Collective Dynamics of Cells" - group (Daniel, Daniela, Hui-Shun, Jaeoh, Jens, Lennart, Maxim, Steffi, Wenwen) for many helpful group meetings. In particular, I want to thank Yen Ting for helping me to develop the computational tools needed for my thesis.
I must thank the different colleagues with whom I was sharing an office. Alex, Jun Won and Dario were great office mates and created an optimal working environment. I also want to thank the "EinUhr-Gruppe" (André, Gary, Helge, Johanna, Laura, Matthias, Samuel, Silvanus) for our daily lunchbreaks and many entertaining discussions. Additionally, I am thankful to Alex, André, Gary, Marko, Omar, Rabea and Samuel for proof-reading this thesis and many helpful remarks. Of course, I am grateful to all the PhD students, postdocs and all other colleagues that I met while working at the institute.
I really appreciate the technical and administrative help I received from the IT department (Hubert Scherrer-Paulus, Thomas, Maik and Steffen) and the MPI PKS administration (especially Rita Dohrmann and Ulrike Burkert).
I am deeply grateful to my parents and my sisters Elisabeth and Friederike for supporting me during the last three decades.
I cannot finish this section without thanking Katya. Thank you for your loving support, for your patience when I was working in the evening or on weekends and making every day so enjoyable.

CONTENTS

LIST OF FIGURES

LIST OF TABLES

1 INTRODUCTION

If one asks how bacteria move, one usually thinks about cells that use rotating flagella to swim through water. In reality, most bacteria are associated with substrates and developed different tools to efficiently move over different surfaces, ranging from the human intestine [1], over the ground of lakes [2] and up to the inside of nuclear reactors [3].

In this chapter, we introduce the different ways how bacteria move over surfaces (see section 1.1) and explain in detail how multiple long cell appendages, the pili, can mediate the surface motility of cells. Afterwards, we give the required basics to study trajectories of particles undergoing Brownian motion and discuss how this knowledge helps us to investigate the motility of bacteria (see section 1.2). Next to the motility of single cells, in this thesis we are also investigating how microcolonies, aggregates consisting of up to thousands of cells, behave. In section 1.3 we describe general mechanisms of how microcolonies form due to type IV pili. Additionally, we discuss the role of microcolonies as early biofilms and their connection to multicellularity, a fundamental requirement for complex life. Before describing the objective and structure of the thesis in the final section 1.5, we introduce the model organism studied in this thesis, the bacterium *Neisseria gonorrhoeae*. In particular, we highlight important properties of these cells and briefly explain the relevance of our results for an improved medical understanding of this pathogenic organism (see section 1.4).

1.1 SURFACE MOTILITY OF BACTERIA

For the survival of many bacteria it is essential for them to move, particularly in order to find nutrients. Additionally, the majority of bacteria is organized in surface-associated communities, the so called biofilms [4, 5] (see subsection 1.3.2). In order to form such a biofilm, bacteria first have to come together.

A mechanism of motion, frequently used by many bacteria, is swimming, driven by the rotation of a single flagellum or multiple flagella [6–10]. Many swimming strategies involving flagella have developed during the evolution of life [11], for example "run and tumble" of *Escherichia coli* [6–10], "run and reverse" of *Shewanella putrefaciens* [12] or "run-reverse-flick" of *Vibrio alginolyticus* [13, 14].

Besides the swimming in a free fluid, bacteria possess also a wide range of tools to move directly on top of different types of substrates, so diverse as eukaryotic cells [15], the outer hull of ships [16] and clinical catheters [17]. A commonly known mechanism where flagella play an important role during the collective motility of multiple bacteria on a substrate is called "swarming" [18, 19]. During this process, bacteria, which in most cases possess flagella [18, 20],

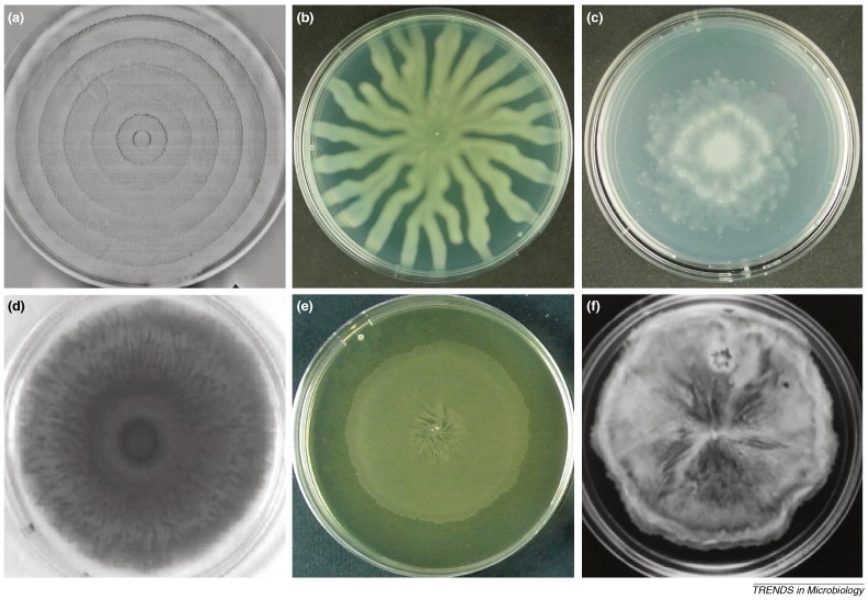

Figure 1.1: Patterns formed by swarming bacteria for (a) *Proteus mirabilis*, (b) *Pseudomonas aeruginosa* (c) *Rhizobium etli* (d) *Serratia marcescens* (e) *Salmonella Typhimurium* and (f) *Escherichia coli*. Image taken from [18].

grow and spread on top of a surface from which they can absorb nutrients. The swarming bacteria often differentiate in a way that cells at the edge are hyperflagellated and form multicellular swarmer cell rafts [21]. The wide range of resulting shapes of the swarming bacteria is shown in figure 1.1.

Apart from flagella, bacteria frequently use so called "type IV pili" to mediate motility. Type IV pili are semiflexible cell appendages that are found in a wide range of bacteria. Some examples are *Pseudomonas aeruginosa*, *Neisseria meningitidis* and *Myxococcus xanthus* [22]. By elongation, attachment and retraction, these pili cause the motility of individual bacteria and cell aggregates, a mechanism reminiscent of a grappling hook (see figure 1.2). Importantly, pili enable cells to move independently of other cells on top of a substrate.

In this thesis, we study how pili mediate the motility of bacteria and how they are involved in the formation of microcolonies. The system we are investigating, the bacterium *Neisseria gonorrhoeae*, is solely using type IV pili to move over substrates and to mediate attractive cell-cell-interactions. For these reasons, we now want to discuss the mechanisms involved in pili-mediated motility in greater detail.

Bacteria possess multiple pili that can emerge homogeneously from the surface of the cells, for example in *Neisseria gonorrhoeae* [23, 24] and *Neisseria meningitidis* [25], or can be locally concentrated, for example at the poles of the rod-shaped *Pseudomonas aeruginosa* [26]. While the pili dynamically change their length, their mean length can be estimated to be around $1-2$ μm [27], thus being comparable to the size of the bacteria [28] (see figure 1.2a and 1.2b). Filaments of up to $10-20$ μm length were also observed experimentally [24, 28].

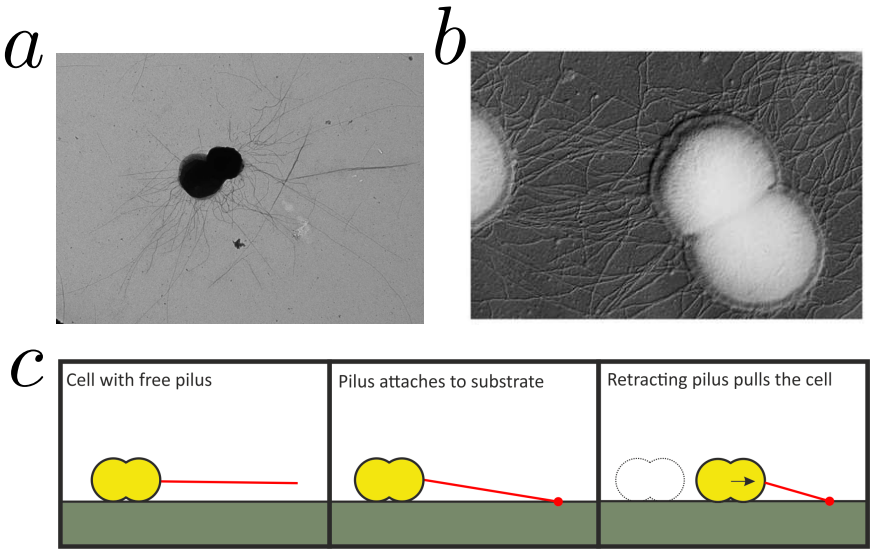

Figure 1.2: Surface-motility mediated by type IV pili. (a,b) Electron microscope images of *Neisseria gonorrhoeae*. The filaments emerging from the surface of the cells are the type IV pili. Image (a) was contributed by Nicolas Biais (Brooklyn College, New York City), image (b) was taken from [29]. (c) Sketch of pili-mediated motility of bacteria. Initially, a pilus is free and protruding. After attachment, the pilus starts to retract and pulls the cell body by a mechanism reminiscent of a grappling hook, causing a displacement.

Individual pili are made of subunits, called pilE. These subunits have an effective size of $0.6 - 0.8$ nm. Thus, an individual pilus having a length in the order of a few microns, consists of thousands of monomers. The resulting filament has the structure of an α-helix [29] with a diameter of around 8.5 nm [30]. It is semiflexible with a persistence length around 5 µm [31]. Subunits not incorporated into the pili are stored in the inner membrane of the cells. They form filaments with the help of a complex molecular machinery, including the ATPases pilF and pilB. The assembled pili are able to extend from the cell membrane through channels, called pilQ, allowing them to bridge the outer membrane (see figure 1.3a). The molecular motor pilT is responsible for the disassembly of the pilus by generating forces of up to $100 - 180$ pN [32–34] (see figure 1.3b). The pilus subunits released after disassembly are recycled into the inner membrane [35]. A detailed description of the molecular details of the pilus machinery is given in [35].

Pili extend and retract from the surface of the cells with velocities of around $1 - 2$ µm/s [23]. The retraction velocity can be altered by oxygen depletion [36] and is regulated by pilT paralogues, in particular pilT2 and pilU. For example, in a pilT2 deletion mutant it was observed that the pilus retraction velocity is reduced considerably [37].

From optical tweezer experiments with pili attaching to trapped silica beads, it was shown that retraction of the pili enables the cell to create drag forces of up to $100 - 200$ pN [32], making pilT to one of the strongest molecular motor known in nature. For comparison,

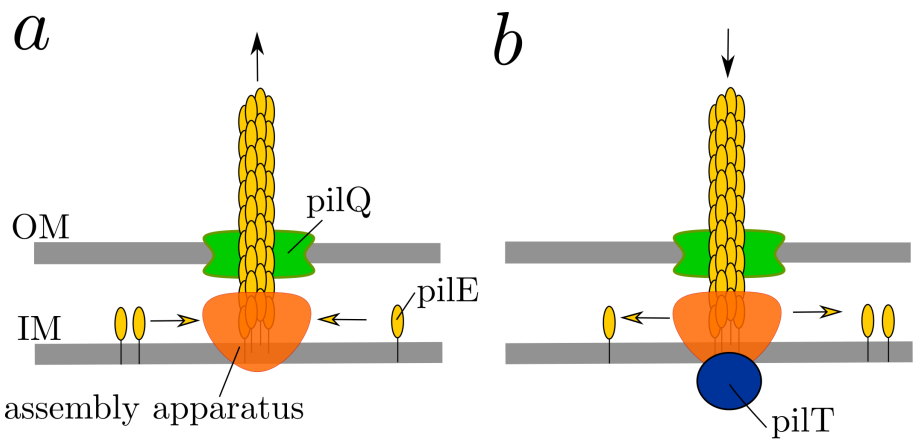

Figure 1.3: Simplified sketch of the type IV pilus machinery. The sketch was adapted from [23, 35]. (a) Assembly of pili. The pilus subunits, called pilE, are moving along the inner membrane (IM) of the bacterium and are assembled by the assembly apparatus. The resulting filament is able to penetrate through the outer membrane (OM) by a channel, called pilQ. (b) Retraction of pili. Due to the molecular motor pilT, the pilus is disassembled, mediating its retraction. Most likely, the subunits are redistributed in the inner membrane.

the forces generated by kinesin and dynein, motors associated with intracellular transport along microtubules, possess characteristic stall forces of less than 6 pN [38]. The cooperative pulling of multiple pili enables the cell to generate forces in the range of nanonewtons [33].

Pili can bind to a substrate. While this binding can be correlated with key residues of the pilus subunits that are involved in adhesion and are only exposed at the tip [39–41], it has also been suggested that pili can possess multiple binding sites along the filament [42, 43]. Pili attached to different substrates exhibit slip-bond behavior, a process where their detachment rate increases with increasing pulling force [34].

The interactions of multiple pili and their cycles of extension, attachment and retraction cause the motion of cells over a substrate, also called "twitching motility" [22]. It is a jerky motion during which cells switch between phases of motion and pauses. This behavior results from collective interactions of multiple pili of a cell [28].

While type IV pili are often involved in the motility of bacteria, they are also frequently used for DNA uptake and exchange [44] and generating attractive cell-cell-interactions, leading to the formation of microcolonies (see subsection 1.3.1).

For completeness, we want to discuss another type of surface motility of bacteria, the so called "gliding motility", a process which is still poorly understood. Cells that glide, including *Salmonella enterica*, *Myxococcus xanthus* [45] and *Bacillus subtilis* [46], exhibit motion over a substrate that is reminiscent of the swarming motility and often involves multiple bacteria. While for some of the bacteria type IV pili seem to mediate the gliding motility, it appears that more than one

mechanism can cause the motility. Many bacteria perform sliding motility without any appendages (like flagella or pili) involved [45].

1.2 RANDOM WALKS AND CHARACTERIZATION OF BACTERIAL MOTILITY

In the first part of this section, we introduce Brownian motion and show how the Langevin equation can be used to study it. The discussion of the Langevin equation allows us to introduce two important quantities, the velocity autocorrelation and the mean squared displacement, both of which are frequently used to characterize the properties of random walks.

In the second part of this section, we formulate and study the master master equation of a simple one-dimensional random walk. Master equations are an important tool for the description of the time evolution of stochastic processes and has been used on multiple occasions within this thesis (see section 3.1 and section 6.2).

In the last part of this section, we give a brief introduction to the motility of bacteria, driven by active processes.

1.2.1 *Brownian motion and the Langevin equation*

In 1828, Robert Brown observed the random motion of pollen grains suspended in water [47]. Only 80 years later, Albert Einstein [48] and Marian Smoluchowski [49] could identify collisions of the pollen with atoms and molecules within the fluid as origin of the random motion. The motion of Brownian particles can be studied by a stochastic differential equation, namely the Langevin equation. The following calculations were taken from [50]. Here, we only present the one-dimensional version of the Langevin equation, higher dimensional forms of this equations can be found in the literature [50, 51].

The Langevin equation describes the force balance of the Brownian particle:

$$\dot{v} = -\mu v + \Gamma(t), \tag{1.1}$$

with the velocity v of the particle, the friction μ and the Langevin force $\Gamma(t)$. Here, the mass m of the particle is included in v, μ and Γ. The stochastic force obeys

$$\langle \Gamma(t) \rangle = 0 \tag{1.2}$$

$$\langle \Gamma(t)\Gamma(t') \rangle = \Gamma_0 \delta(t - t') \tag{1.3}$$

and is also called white noise-force. In this equation, Γ_0 denotes the strength of the noise and $\delta(x)$ is the Dirac delta function.

From the Langevin equation, one can compute the particle velocity, given by

$$v(t) = \exp(-\mu t) \left[v_0 + \int_0^t dt' \, \exp(\mu t') \, \Gamma(t') \right], \tag{1.4}$$

with the initial velocity v_0. The velocity autocorrelation is then given by

$$\langle v(t_1)v(t_2)\rangle = v_0^2 \exp\left[-\mu(t_1+t_2)\right] + \frac{\Gamma_0}{2\mu}\left(\exp\left[-\mu|t_1-t_2|\right] - \exp\left[-\mu(t_1+t_2)\right]\right). \quad (1.5)$$

For $\mu t_1 \gg 1$ and $\mu t_2 \gg 1$ this equation takes a simpler form

$$\langle v(t_1)v(t_2)\rangle = \frac{\Gamma_0}{2\mu}\exp\left[-\mu|t_1-t_2|\right]. \quad (1.6)$$

In the stationary state we get

$$\langle v(t)^2\rangle = \frac{\Gamma_0}{2\mu}. \quad (1.7)$$

By assuming thermodynamic equilibrium we can use the equipartition theorem and determine the strength of the noise, Γ_0, by

$$\frac{1}{2}kT = \frac{1}{2}m\langle v(t)^2\rangle = \frac{\Gamma_0 m}{4\mu}, \quad (1.8)$$

where k is the Boltzmann constant, T is the temperature and m is the mass of the Brownian particle. Then we have

$$\Gamma_0 = \frac{2\mu kT}{m}. \quad (1.9)$$

When we track the trajectory $x(t)$ of an particle, we can define its velocity by

$$v(t) = \dot{x}(t) = \lim_{\Delta t\to 0}\frac{x(t+\Delta t)-x(t)}{\Delta t}. \quad (1.10)$$

For the analysis of experimental data, we cannot reach the limit $\Delta t = 0$, but need to pick a finite Δt. This makes the value of the velocity dependent on the value of Δt and thus it is often difficult to estimate the velocity autocorrelation experimentally. We can define another quantity which only depends on the position of the particle and thus, is independent of the value of Δt, the so called mean squared displacement:

$$\langle (x(t)-x(0))^2\rangle = \int_0^t dt_1 \int_0^t dt_2\ \langle v(t_1)v(t_2)\rangle. \quad (1.11)$$

The mean squared displacement of a Brownian particle is then given by

$$\langle (x(t)-x(0))^2\rangle = \left(v_0^2 - \frac{\Gamma_0}{2\mu}\right)\frac{\left(1-\exp\left[-\mu t\right]\right)^2}{\mu^2} + \frac{\Gamma_0}{\mu^2}t - \frac{\Gamma_0}{\mu^3}\left(1-\exp\left[-\mu t\right]\right). \quad (1.12)$$

For very large values of the time, $\mu t \gg 1$, this equation simplifies to

$$\langle (x(t)-x(0))^2\rangle \simeq 2Dt. \quad (1.13)$$

Here, we define the diffusion coefficient

$$D = \frac{\Gamma_0}{2\mu^2} = \frac{kT}{m\mu}, \quad (1.14)$$

giving an equation that is called the Stokes-Einstein relation. Note that the particle mass m is incorporated in the friction μ and thus, the diffusion coefficient is not dependent on the mass.

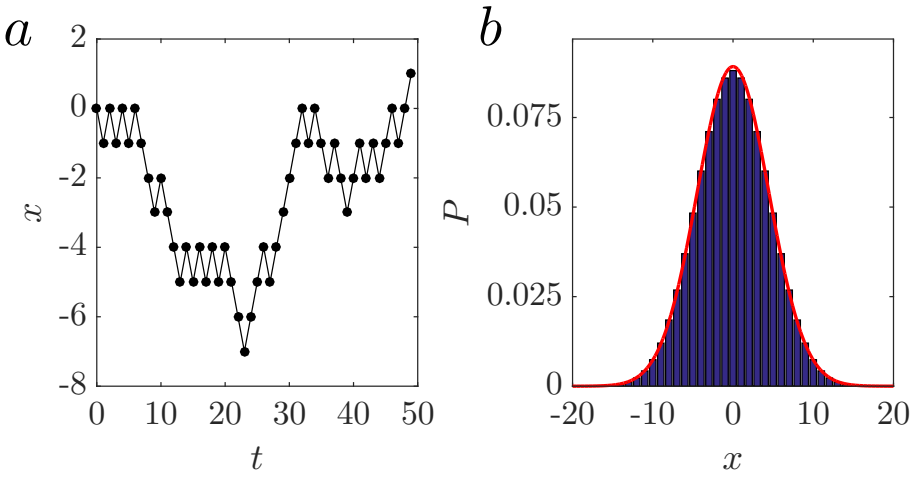

Figure 1.4: One-dimensional random walk. (a) Trajectory of a one-dimensional random walk with constant step length of 1, constant time steps of 1 and $p = q = 0.5$. (b) Discrete probabilities $P(x,t)$ (bars) for a one-dimensional random walk, as given by equation 1.17, at time $t = 50$. The continuous limit of the probability distribution, given by equation 1.18, is shown by the red line.

1.2.2 *Master equation of a simple random walk*

We study how a particle moves randomly on a one-dimensional lattice and how this can be described by a Master equation [52].

The probability of the particle to be at a point x at time t is given by $P(x,t)$. For now, we assume that x and t can only take integer values, $x \in \mathbb{Z}$ and $t \in \mathbb{N}$. The particle jumps at each time step, chosen to be constant, with a probability p to the right and with a probability $q = 1 - p$ to the left. Such a random walk is shown in figure 1.4a. The evolution of the system is then given by

$$P(x,t) = pP(x-1,t-1) + qP(x+1,t-1). \tag{1.15}$$

Additionally, we can write down the rate of change of the probability $P(x,t)$, given by

$$\begin{aligned} P(x,t) - P(x,t-1) = {} & pP(x-1,t-1) + qP(x+1,t-1) \\ & - (p+q)P(x,t-1). \end{aligned} \tag{1.16}$$

The solution of these equations is the binomial distribution,

$$P(x,t) = \frac{t!}{2\left(\frac{t+x}{2}\right)!\left(\frac{t-x}{2}\right)!} p^{\frac{t+x}{2}} q^{\frac{t-x}{2}} \tag{1.17}$$

and for large t it can be approximated by

$$P(x,t) \simeq \frac{1}{\sqrt{2\pi t}} \exp\left[-\frac{(x-t(p-q))^2}{2t}\right], \tag{1.18}$$

which is a Gaussian distribution. The form of these distributions is shown in figure 1.4b.

In the continuum limit, where we consider the infinitesimal step length Δx and time Δt, the master equation has the form

$$P(x,t) = pP(x-\Delta x, t-\Delta t) + qP(x+\Delta x, t-\Delta t). \tag{1.19}$$

By making a Taylor expansions of $P(x,t)$ for Δt and Δx we get

$$P(x,t) \approx (p+q)\left(P(x,t) - \frac{\partial P}{\partial t}\Delta t\right) - (p-q)\frac{\partial P}{\partial x}\Delta t + \frac{p+q}{2}\frac{\partial^2 P}{\partial x^2}\Delta x^2. \tag{1.20}$$

By considering the fact that $p+q=1$ and setting

$$V = \lim_{\Delta t, \Delta x \to 0}(p-q)\frac{\Delta x}{\Delta t}, \tag{1.21}$$

$$D = \lim_{\Delta t, \Delta x \to 0}\frac{1}{2}\frac{\Delta x^2}{\Delta t} \tag{1.22}$$

we get

$$\frac{\partial P}{\partial t} = -V\frac{\partial P}{\partial x} + D\frac{\partial^2 P}{\partial x^2}. \tag{1.23}$$

Here, V is the constant drift and D is the diffusion coefficient. This equation is a special form of the Fokker-Planck equation with constant D and V and is also known as Smoluchowski equation. For $p = 0.5$ the drift vanishes, $V = 0$, and with the initial condition

$$P(x,0) = \delta(x) \tag{1.24}$$

(with the Dirac delta function $\delta(x)$), the resulting probability density function of the one-dimensional random walk is given by

$$P(x,t) = \frac{1}{\sqrt{4\pi D t}}\exp\left(-\frac{x^2}{4Dt}\right). \tag{1.25}$$

By computing the second moment of this distribution,

$$\langle x(t)^2\rangle = 2Dt, \tag{1.26}$$

we get the same expression as computed from the Langevin equation for the mean squared displacement (see equation 1.13).

1.2.3 *Bacterial motility as an active process*

As it was discussed in section 1.1, the motility of bacteria can originate from many mechanisms. Up to now, we assumed that the random motion of the Brownian particle was due to thermal noise, assuming thermodynamic equilibrium.

In reality, the motility of living organisms, in particular moving bacteria, is characterized by an active self-propulsion [7, 53].

Cells are called "active" when energy is taken in and dissipated and due to this processes, the cell executes motion [53]. An example of

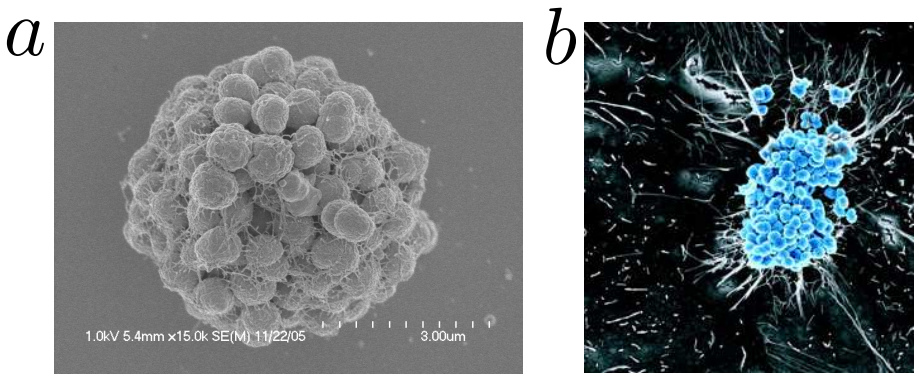

Figure 1.5: Microcolonies of *Neisseria gonorrhoeae*. Electron microscope images of *Neisseria gonorrhoeae* microcolonies. (a) A microcolony growing on a glass surface. The image was contributed by Nicolas Biais (Brooklyn College, New York City). (b) Microcolony growing on top of epithelial cells. Due to the retraction of attached pili, the microvilli of the epithelial cells, located beneath the microcolonies, are stretched and elongated. The figure was adapted from [54].

such a process is the retraction of a pilus, mediated by the molecular motor pilT [23].

Many aspects of the random motion of active particles can be understood within the framework of the Langevin equation introduced above. In the case of active systems, the noise strength is different from equation 1.9 and is affected by active processes driving the system out of thermodynamic equilibrium.

To characterize the random motion of active particles, we can often take the passive models, described in the previous chapters, and replace the origin of the noise Γ, for example by different intercellular processes or hydrodynamic interactions [7].

1.3 BACTERIAL MICROCOLONIES AND THEIR FORMATION

After showing how pili mediate the motion of single cells and how we can study the motility of bacteria, we will now consider bacterial microcolonies, aggregates consisting of several bacteria. In the first part of this section, we introduce microcolonies and their formation, mediated by type IV pili. Such microcolonies are the first step in the formation of early biofilms, surface-associated communities of bacteria. In the second part of this section, we introduce the model organism of this thesis, the pathogenic bacterium *Neisseria gonorrhoeae*.

1.3.1 *Pili-mediated formation of microcolonies*

Besides the motility of individual cells on top of a substrate (see section 1.1), pili can also mediate the formation of microcolonies, bacterial aggregates consisting of up to thousands of cells [55, 56]. For many bacteria, this is one of the main mechanisms to form aggregates [29]. The formation of these microcolonies is driven by pili-

mediated attractive cell-cell-interactions, originating from the binding of two or more retracting pili [29, 54, 57].

For pili-pili-bundling it has been suggested that the strength of interactions is dependent on the geometry of the pili, in particular whether two pili are parallel or antiparallel. Pili protruding from a single cell are in general parallel to each other. Interactions of the pili of these cell would reduce the available pili surface area that can be used for bonds to pili of other cells, without offering any direct benefit. On the other side, pili of different cells are likely to be antiparallel to each other and in this case it would be preferential to form pili-pili-bonds [29]. Although this idea appears plausible, no direct experimental proof for type IV pili is available up to this date. For F-actin filaments it was shown in a recent study that interfilament sliding friction differs for parallel and antiparallel sliding [58].

In figure 1.5, microcolonies of *Neisseria gonorrhoeae* are shown, which formed due to pili-pili-interactions of the individual cells. The colonies themself also possess free pili at their surface that are elongating to the surrounding fluid and can attach to a substrate (for example epithelial cells), enabling the colony to perform motility over the substrate [59, 60]. Because of this, colonies are able to move, collide and coalesce with other colonies, thus introducing an important mechanism of colony growth (see chapter 3 and chapter 6).

Cells benefit from the formation of microcolonies by protecting the cells within the aggregates from external chemical and mechanical threats. Additionally, microcolonies possess more pili adjacent to the substrate, thus increasing the strength of the interactions with the surface and the force the colony is exerting on the surface (for example epithelial cells). These forces can be in the order of nanonewton for a single pili bundle [33], allowing the cells to mediate dramatic changes to the cytoskeleton. These changes can be beneficial for the infection of pathogenic bacteria, for example *Neisseria gonorrhoeae* [54].

The bacterial microcolonies formed by pili-pili-interactions represent the first step of the formation of biofilms.

1.3.2 *Microcolonies as precursors of biofilms*

While one usually imagines bacteria as individual entities, in fact most bacteria organize in biofilms, surface-associated communities of bacterial cells on a substrate, embedded in an exopolysaccharide matrix [61].

The life cycle of a biofilm, here presented for *Myxococcus xanthus* bacteria and depicted in figure 1.6, can be divided into five stages [55, 61, 63]:

1. Planktonic state: In the first phase, individual cells are freely moving, being independent of each other. Cells possessing flagella (for example *Escherichia coli* or *Myxococcus xanthus*) are swimming during this phase, cells having pili only (for example *Neisseria gonorrhoeae* or *Neisseria meningitidis*) are moving on

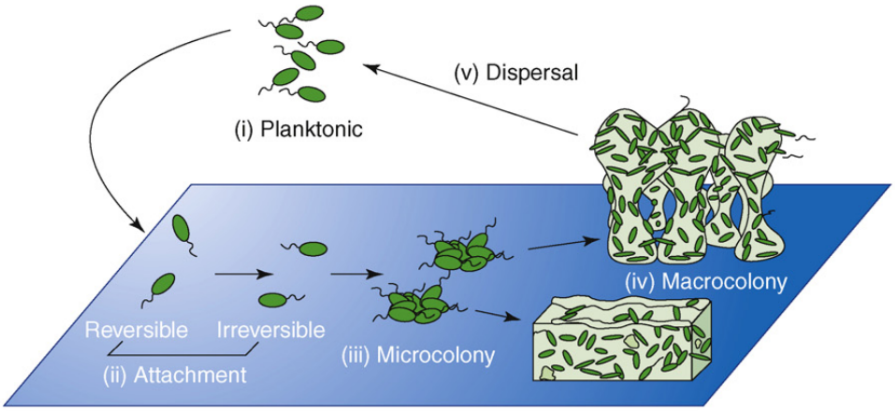

Figure 1.6: Life cycle of a biofilm, taken from [61]. Initially, cells need to find a surface on which they can form the biofilm. This phase is called the planktonic state, where individual cells swim through a fluid. It is followed by the attachment phase, where cells adhere with the help of pili to the surface. This phase can be divided into "reversible" and "irreversible" [62], characterized by how strong the bond with the surface is. The attached cells will form microcolonies due to different growth mechanisms like proliferation and coalescence of colonies. During this step, the pili-mediated surface motility plays an important role. The microcolonies create an exopolysaccharide matrix that also includes dead cells and extracellular DNA, representing the fourth state, the macrocolony. In this state, the colony can take different shapes. In the last step, such macrocolonies dissolve by resetting at least a fraction of cells to the planktonic state, which allows the bacteria to invade the environment.

a substrate. The motion continues until the bacteria come close to the substrate.

2. Attachment state: When cells are close to a substrate, they can adhere, for example by using type IV pili. The adhesion can often be differentiated into ”reversible” and ”irreversible” [61, 62]. They differ in the strength of the binding such that, for the ”reversible” state, it is considerably weaker. Often, cells are initially in a ”reversible” state, followed by the transition to the ”irreversible” state.

3. Microcolony formation: Due to different growth mechanisms (like cell divisions and coalescence of smaller cell aggregates and cells moving on the substrate) microcolonies consisting of a high number of cells can form. These microcolonies continue their growth until they start forming macrocolonies.

4. Macrocolony formation: Macrocolonies often have a mushroom-like shape that originates from pili-mediated interactions of the cells [64]. The cells are separated by fluid-filled void regions, that can take different complex shapes. Additionally, cells within macrocolonies produce an exopolysaccharide matrix, that also includes dead cell debris and extracellular DNA.

5. Dispersal state: Macrocolonies are able to dissolve, releasing single cells into the surrounding fluid and bringing them back to the planktonic state, allowing them to disperse after local resources of nutrients have been depleted.

From this overview of the biofilm life cycle it becomes clear that the formation of biofilms is an expensive process that involves the production of a high amount of molecules that will later form the exopolysaccharide matrix. This cost is outweighed by the advantages a biofilm offers to the individual cells.

Cells within biofilms are better protected from antibiotics than cells in the planktonic state, making them up to 1000 times more resistant to those antimicrobial drugs [65, 66]. Biofilms also enable the cells to withstand strong shear forces [67, 68]. Additionally, biofilms are able to protect individual cells from UV radiation [69] and predators, in particular from unicellular eukaryotic organisms called protozoa [70]. The formation of such biofilms is often triggered by environmental limitations, such as a lack of nutrients [61, 71].

Interestingly, biofilms are not only formed by a single species, but often form polymicrobial aggregates, consisting of more than one bacteria species [72–74].

Additionally, biofilms can contain cells with different fates, such that initially identical cells follow different developmental pathways. Depending on where a cell is positioned within a biofilms, it adopts different properties. The cells can exhibit differences in motility, production of the exopolysaccharide matrix or mechanical properties, mediating the formation of the mushroom-shape of the biofilm during the macrocolony state [75].

In order to organize such complex differentiation within biofilms, individual cells must be able to communicate with each other. The differentiation can be triggered by quorum sensing, intercellular signaling that is driven by the secretion and recognition of different molecules [76]. Additionally, it was recently suggested that mechanical cues may also affect the differentiation of cells within microcolonies and biofilms [77].

Finally, it is interesting to point out that strong similarities exist between differentiation patterns of bacteria within biofilms and the development of multicellular organisms [5], for example during embryogenesis.

1.4 *neisseria gonorrhoeae* AS MODEL ORGANISM TO STUDY BACTERIAL COLONY FORMATION

In this thesis, we investigate how pili mediate the formation of bacterial microcolonies and the motility of cells and microcolonies on a substrate. The model organism of our choice is the bacterium *Neisseria gonorrhoeae*. Due to the fact that these bacteria only possess type IV pili and no other tools to cause cell motility and attractive cell-cell-interactions, it is an ideal organism to study exactly those processes.

The individual bacteria have a dumbbell-shape, which is called a diplococcus [29] (see figure 1.2), and possess around 5-20 pili protruding from the cell membrane [28, 29, 34]. The microcolonies formed by *Neisseria gonorrhoeae* can consist of up to thousands of cells, reaching diameters in the order of $20 - 30$ μm (see figure 1.5).

The bacterium *Neisseria gonorrhoeae* is the causative agent of the sexually transmitted disease gonorrhea. With 80 million reported new infections worldwide every year, gonorrhea is one of the most common sexually transmitted diseases worldwide, causing around 700 reported deaths in 2015 [78, 79]. While the number of reported deaths is, compared to other bacterial diseases, low, it could increase considerably in the future due to the alarming development of antibiotic resistance by *Neisseria gonorrhoeae*.

Antibiotic treatment of the disease gonorrhea reaches back as far as 1897, where Arthur Eichengrün successfully used colloidal silver, called Protargol, as treatment [80]. In recent years, treatment of the disease gonorrhea has been compromised by an alarming rise of resistance to antibiotics. This goes up to the point where only the antibiotic Ceftriaxone is able to guarantee a successful treatment [81–84], although first cases of resistances were reported even for Ceftriaxone [85–87].

It is important to highlight that the bacteria are only able to infect human cells, prohibiting to study *Neisseria gonorrhoeae* with the help of animal models. In order to induce the infection, pili of *Neisseria gonorrhoeae* bind specifically to the human transmembrane glycoprotein CD46 [88]. The epithelial cells associated with the single bacteria and bacterial microcolonies exhibit a higher concentration and elongation of microvilli, membrane protrusion that are involved in adhesion of

eukaryotic cells (see figure 1.5b) [54]. Additionally, pilus attachment and retraction mediates the formation of cortical plaques, cytoskeletal domains with an increased concentration of actin [89]. Due to these dramatic changes of the mechanics of the epithelial cells and their cytoskeleton, cell apoptosis is triggered, which is an important step during the infection process [29, 54].

While we focus on the dynamics of *Neisseria gonorrhoeae* in this thesis, our results can be applied to other pathogenic and highly dangerous bacteria possessing type IV pili, for example *Neisseria meningitidis* and *Pseudomonas aeruginosa*.

1.5 OBJECTIVES AND STRUCTURE OF THIS WORK

In this thesis we want to study how forces, specifically those mediated by type IV pili, can mediate the dynamics of bacteria and bacterial aggregates. The model organism of our choice is the bacterium *Neisseria gonorrhoeae*.

In order to highlight the importance of pili during the life of these bacteria, we start by looking at multiple single cells on top of a substrate. Due to their pili, these cells move over the substrate, a process which is studied in chapter 3. While the cells move, they will start to come close to each other and interact due to the binding of pili to each other. This will mediate the formation of microcolonies (see chapter 4 and chapter 6).

The colonies are then also able to move over the substrate (see chapter 3). In this thesis, we study how single cells and colonies move over on a substrate and how different models can be applied to explain experimental observations.

How individual cells behave within a colony and how this behavior affects processes like the coalescence of two colonies is studied in chapter 4. Here, we compare bacterial microcolonies to liquid droplets. Additionally, we study how wild type cells and different types of mutated cells mix and demix within microcolonies and connect our observations to the differential adhesion hypothesis (see chapter 5).

The three main processes affecting the formation and growth of these colonies are the pickup of single cells due to larger microcolonies, the coalescence of two colonies in order to form a larger colony and the proliferation of the bacteria. The time-dependent distribution of colony sizes is studied in chapter 6 and compared to experimental results.

To study the dynamics of cells and microcolonies, we developed a computational model, allowing us to investigate the role of individual pili interactions during all processes previously mentioned (see chapter 2).

In this thesis, we employ experimental, theoretical and numerical approaches to study how pili lead to bacterial behavior on multiple scales: from individual cells, over single colonies and up to multiple colonies.

2

COMPUTATIONAL MODEL OF BACTERIAL MOTILITY AND MECHANICS

In order to study how pili mediate the dynamics of single bacteria and microcolonies, we developed a computational model of individual cells in which the direct cell-cell-interactions are modeled by explicitly simulating the dynamics of pili and computing the forces mediated by them. This allows us to study quantities that are not (yet) accessible by experiments, for example the properties of the pili and the forces acting on cells within a colony.

The main features of the computational model are described in this chapter, more details can be found in appendix A. The presented model was published in [60]. It allows us to investigate the motion of single cells on a substrate (see chapter 3), the internal dynamics of microcolonies and how they affect the coalescence of microcolonies (see chapter 4) and the self-assembly of mixtures of different cell populations (see chapter 5).

While the model was developed to study the behavior of *Neisseria gonorrhoeae*, it can easily be adapted to investigate the dynamics of a wide range of bacteria possessing type IV pili by changing the used parameters (for *Neisseria meningitidis*) or by changing the geometry of the cells (for *Pseudomonas aeruginosa* or *Neisseria elongata*).

2.1 GEOMETRY OF THE CELLS AND FREE PILI DYNAMICS

The cells of *Neisseria gonorrhoeae* possess a dumbbell shape, also called a diplococcus [29]. In our model, the *in silico* cell consists of two spheres, the so called cocci, that each have a radius R. The positions of the cocci a and b of one cell i are given by $\mathbf{r}_i^{(a)}$ and $\mathbf{r}_i^{(b)}$, such that $|\mathbf{r}_i^{(a)} - \mathbf{r}_i^{(b)}| = d_{cocci} < 2R$. They thus have a fixed distance (see figure 2.1a). The center of the cell is then given by

$$\mathbf{r}_i^{(com)} = \frac{\mathbf{r}_i^{(a)} + \mathbf{r}_i^{(b)}}{2}. \tag{2.1}$$

A cell possesses around 5-20 pili [27, 28, 34] that are randomly created by the cell with a rate γ_{prod} and homogeneously distributed on the surface of the cell [28]. It has been suggested that that the number of pili is limited by the number of domains responsible for pili creation [35]. Thus, we introduce a maximal number of pili N_{max} that limits the amount of pili a cell possesses.

Pili are modeled as springs. They have the shape of a line, with their position being characterized by two points: their start point at the surface of the cell (also called anchor point) and their end point (see figure 2.1a). The distance between these two points is named the contour length of the pilus. It has been suggested by experiments

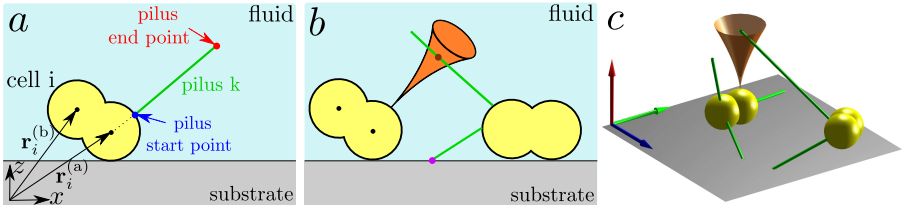

Figure 2.1: Schematic representation of the geometry of the simulations and how pili interact with the substrate and other pili. Figure adapted from [60]. (a) A dumbbell shaped cell i with cocci positions $\mathbf{r}_i^{(a)}$ and $\mathbf{r}_i^{(b)}$ with one pilus. The position of the pilus k is characterized by its start point, which is the anchor point connecting the pilus and the cell, and its end point. (b) Pili can bind to a substrate with their tip or can bind to other pili. The binding of two pili is chosen from the intersection of the beam region of one pilus, resulting from its thermal fluctuations, and the line shape of the second pilus. (c) Three-dimensional representation of the geometry and the pili dynamics in the computational model.

that the pili lengths are exponentially distributed with a characteristic length of $l_c = 1 - 2\ \mu m$ [27, 28].

The persistence length of type IV pili was initially measured by Skerker et al. in 2001 [31] to have a value of 5 μm by observing the thermal fluctuations of fluorescently labeled pili associated with a substrate. Contrary to this result, in 2015 Lu et al. [90] used AFM pulling experiments to estimate the value of the persistence length to be around 1 nm, thus being three orders of magnitude lower than the earlier measured value. A recent theoretical analysis [91] of the effects of pili persistence length l_{pers} on the motility of cells suggests that the persistence length is in the order of microns, thus confirming the results of Skerker et al. Here, we use their value and assume that pili are semiflexible polymers.

In our model, a pilus protrudes perpendicularly from the surface of the cell with a velocity v_{pro}. When a pilus hits the substrate, it will slide along the substrate with its tip. The protrusion of a pilus continues until it switches stochastically to a retraction state. The rate γ_{ret} after which this switching takes place is governed by the characteristic length l_c of the pili, so that $\gamma_{ret} = v_{pro}/l_c$. After switching to a retraction mode, a pilus is no longer able to switch back to a protrusion state. Here, we assume that the velocity of protrusion and the velocity of retraction have the same value

$$v_{pro} = v_{ret} = v_0, \tag{2.2}$$

as has been suggested experimentally [23]. A pilus is removed if the contour length has shrunk to zero due to its retraction. More details about the geometry and the pili dynamics can be found in appendix A.1.

2.2 BINDING OF PILI TO A SUBSTRATE AND TO OTHER PILI

Pili are able to bind stochastically to the substrate with their tip and to other pili along their full length (see figure 2.1b). Information of how these processes are implemented are given in the following subsections.

After attachment, pili start to retract immediately in our model, as has been suggested experimentally [35]. Pili that are attached are not allowed to bind to the substrate or other pili, thus only binary interactions are permitted.

2.2.1 *Pili substrate binding*

The exact mechanism of how type IV pili bind to substrates is not known. For the pili of *Pseudomonas aeruginosa* it has been suggested that pili possess key residues of the pilin subunits that are involved in adhesion and are only exposed at the tip [39–41]. Within the polymer, they are involved in the interactions of the subunits. For other proteins associated with pili it was suggested that they are not only located at the tip of the pili, but can also be rarely found along the filament, so that a pilus may possess multiple binding sites [42, 43].

In our model, we assume that the tip of a pilus binds to the substrate with an attachment rate $\gamma_{\text{att,ps}}$ if the tip is directly on top of the substrate. In particular, the $z-$component of the end point $\mathbf{r}_k^{(e)}$ of the pilus needs to be 0 (see figure 2.1b).

2.2.2 *Pili-pili binding*

Pili mediate attractive interactions between cells by binding to pili of other cells [25, 92, 93]. The experimental observation that cells without pili are not incorporated into bacterial microcolonies [57] suggests that pili are not able to bind to the surface of bacteria.

In our model, pili are characterized as lines with an start points $\mathbf{r}_k^{(s)}$ and end points $\mathbf{r}_k^{(e)}$. In order to describe the binding of two pili, we consider the thermal fluctuations of pili that swipe through a cone-like region in space (see figure 2.1b and 2.1c). The cone-like shape of this region is governed by the beam equation [94], more details are given in chapter A.2. If a pilus, having the shape of a line, and a second pilus having the shape of such a cone, intersect, they can bind stochastically with the rate $\gamma_{\text{att,pp}}$ at a random point of the line segment within the beam volume.

2.3 FORCES AND MOTILITY

We consider two classes of forces that are acting on the cells: excluded volume forces and pili-mediated forces.

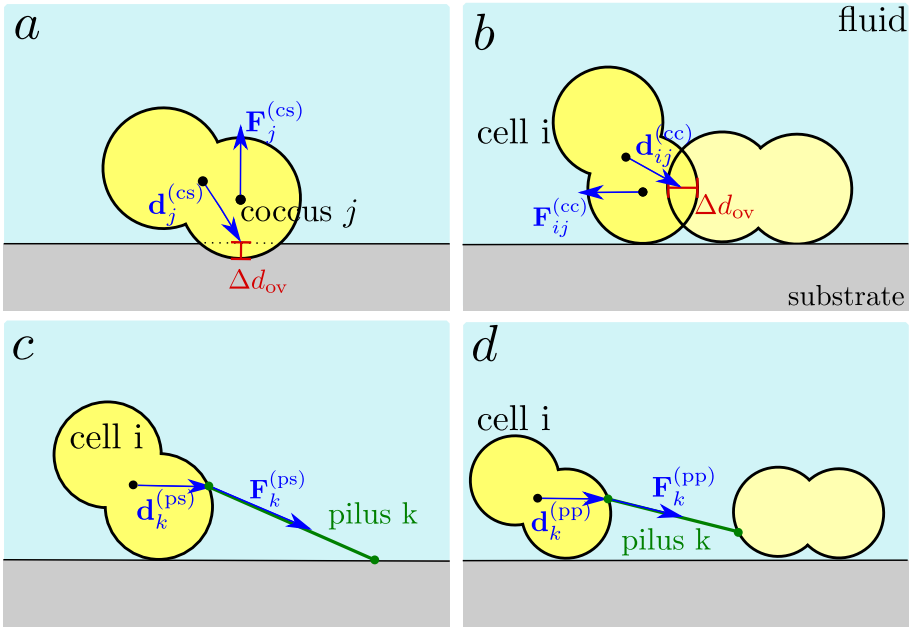

Figure 2.2: Sketch of the different forces that are acting on cells within the model and mediate the cell motion. The figure was taken from [60]. (a) Excluded volume forces $\mathbf{F}_j^{(cs)}$ of a cell overlapping with a substrate and the distance vector $\mathbf{d}_j^{(cs)}$, pointing from the center of the cell pointing towards the point where the force is acting. (b) Excluded volume forces $\mathbf{F}_{ij}^{(cc)}$ of a cell overlapping with a substrate with the overlap length Δd_{ov} and the distance vector $\mathbf{r}_{ij}$, pointing from the center of the cell towards the center of the cocci of cell i and j. (c) Pili-mediated forces $\mathbf{F}_k^{(ps)}$ due to binding to the substrate. The vector $\mathbf{d}_k^{(ps)}$ points from the center of the cell to the start point of the pilus. (d) Pili-mediated forces $\mathbf{F}_k^{(pp)}$ due to binding of two pili. The vector $\mathbf{d}_k^{(pp)}$ points from the center of the cell to the start point of the pilus k.

2.3.1 *Excluded volume forces*

If a cell overlaps with a substrate, located at position $z = 0$ (see figure 2.2a), a repulsive force $\mathbf{F}_j^{(cs)}$ will act from the substrate on coccus $j = a, b$, described by a simple Hookean spring with spring constant k_{cs} in the normal direction.

Additionally, the overlap of two cells, called i and j, results in a repulsive force $\mathbf{F}_{ij}^{(cc)}$ (see figure 2.2b). Again, this is described as a harmonic force with a different spring constant k_{cc}.

2.3.2 *Pili and pili-mediated forces*

Pili are modeled as springs with spring constant k_{pili}. If a pilus k is attached to the substrate or another pilus, it will start to retract and, due to the resulting stretching of the spring, generate a force $\mathbf{F}_k^{(ps)}$ or $\mathbf{F}_k^{(pp)}$. These forces are proportional to the difference between the contour length $l_k^{(cont)}$ of the attached pilus and the length of the pilus if it be not attached, called the free length $l_k^{(free)}$. If a pilus is not stretched but compressed, it is not able to generate any force between cells or to the substrate. While the contour length of the pili is a function of the position of the cells and their pili, the free length is affected by the retraction of the pili. The retraction velocity $v_k^{(ret)}$ of pilus k is affected by the pulling force F and exhibits stalling behavior,

$$v_k^{(ret)} = \max\left[0,\ v_{ret}\left(1 - \frac{F}{F_{stall}}\right)\right], \tag{2.3}$$

with the stalling force F_{stall} [23, 95]. Here, F is the absolute value of $\mathbf{F}_k^{(pp)}$ or $\mathbf{F}_k^{(ps)}$.

Additionally, the pilus detachment rate ($\gamma_{det}^{(sub)}$ for pilus-substrate bonds and $\gamma_{det}^{(pili)}$ for pilus-pilus bonds) is affected by the pulling force:

$$\gamma_{det}^{(sub)} = \frac{1}{t_{d,ps}} \exp\left(\frac{F}{F_{d,ps}}\right), \tag{2.4}$$

$$\gamma_{det}^{(pili)} = \frac{1}{t_{d,pp}} \exp\left(\frac{F}{F_{d,pp}}\right), \tag{2.5}$$

where we define the pili detachment times $t_{d,pp}$ and $t_{d,ps}$ and the pilus detachment forces $F_{d,pp}$ and $F_{d,ps}$. The form of these equations is motivated by Kramer [96] and Bell et al. [97]. From experiments [34], it was also proposed that the detachment rate follows

$$\gamma_{det}^{(sub)} = \frac{1}{t_{d,ps}^{(1)} \exp\left(-\frac{F}{F_{d,ps}^{(1)}}\right) + t_{d,ps}^{(2)} \exp\left(-\frac{F}{F_{d,ps}^{(2)}}\right)}. \tag{2.6}$$

with the detachment forces $F_{d,ps}^{(1)} = 1.28$ pN and $F_{d,ps}^{(2)} = 33.8$ pN and the detachment times $t_{d,ps}^{(1)} = 0.85$ s and $t_{d,ps}^{(2)} = 0.04$ s on a BSA-coated glass surface.

Further information concerning the pili-mediated forces are given in appendix A.3.

2.3.3 *Cell motility*

The total force acting on a cell i is then given by

$$\mathbf{F}_i^{(\mathrm{tot})} = \sum_{\text{cocci } j} \mathbf{F}_j^{(\mathrm{cs})} + \sum_{\text{cells } j} \mathbf{F}_{ij}^{(\mathrm{cc})} + \sum_{\text{pili } k} \mathbf{F}_k^{(\mathrm{ps})} + \sum_{\text{pili } k} \mathbf{F}_k^{(\mathrm{pp})} \tag{2.7}$$

Additionally, the torque acting on cell i is given by

$$\begin{aligned}\mathbf{T}_i^{(\mathrm{tot})} = &\sum_{\text{cocci } j} \mathbf{d}_j^{(\mathrm{cs})} \times \mathbf{F}_j^{(\mathrm{cs})} + \sum_{\text{cells } j} \mathbf{d}_{ij}^{(\mathrm{cc})} \times \mathbf{F}_{ij}^{(\mathrm{cc})} \\ &+ \sum_{\text{pili } k} \mathbf{d}_k^{(\mathrm{ps})} \times \mathbf{F}_k^{(\mathrm{ps})} + \sum_{\text{pili } k} \mathbf{d}_k^{(\mathrm{pp})} \times \mathbf{F}_k^{(\mathrm{pp})}.\end{aligned} \tag{2.8}$$

Here, $\mathbf{d}_j^{(\mathrm{cs})}$, $\mathbf{d}_{ij}^{(\mathrm{cc})}$, $\mathbf{d}_k^{(\mathrm{ps})}$ and $\mathbf{d}_k^{(\mathrm{pp})}$ are the distance vectors pointing from the center of the cell $\mathbf{r}_i^{(\mathrm{com})}$ to the points at which the forces are acting (see figure 2.2).

We assume that the velocity of the cell i is related to the force in the overdamped limit [98], thus its center and the positions of the cocci follow

$$\frac{d\mathbf{r}_i^{(\mathrm{com})}}{dt} = \frac{d\mathbf{r}_i^{(\mathrm{a})}}{dt} = \frac{d\mathbf{r}_i^{(\mathrm{b})}}{dt} = \mu_{\mathrm{trans}} \mathbf{F}_i^{(\mathrm{tot})}, \tag{2.9}$$

where μ_{trans} is the translational mobility of the cells. Additionally, the cell and its cocci rotate due to the torque, where the angular velocity vector is given by

$$\mathbf{w}_i^{(\mathrm{tot})} = \mu_{\mathrm{rotat}} \mathbf{T}_i^{(\mathrm{tot})}, \tag{2.10}$$

where μ_{rotat} is the rotational mobility of the cell.

2.4 SIMULATION DETAILS

The simulations were performed on the local computing cluster of the MPI-PKS, consisting of x86-64 GNU/Linux systems. All machines possess Intel Xeon processors with a clock rate of 2.2 to 3.0 GHz and have between 2 to 4 CPUs. The code was written in C++ and parallelized on CPU by using the library OpenMP. We used the GCC-compiler (version 4.8.1) and were running the simulations on up to 8 cores in parallel.

We used an Euler algorithm to solve the equations of motion with a time step $\Delta t = 5 \times 10^{-6}$ s or smaller. Higher order schemes offer comparable results, but they do not increase the computation speed.

While most parameters within our model are known from experiments (see table 2.1), many parameters play only a minor role within our simulation, e.g.the excluded volume constants k_{cc} and k_{cs} which are in general large [99] (compared to the forces mediated by pili)

and do not affect the simulations as long as they are large enough to not allow overlapping of cells with each other and the substrate (see appendix F.3.1).

If not stated otherwise, the translational and rotational mobility μ_{trans} and μ_{rotat} were chosen such that the viscosity is $10\times$ larger than the viscosity of water. This modification is useful because it allows to increase the time step Δt of the simulation. The used mobilities correspond to a force of 2 pN to move a single cell with the maximal pilus retraction velocity v_{ret}. This force is considerably smaller than the characteristic pilus pulling force F_{stall}, and also much smaller than the detachment forces we used in most parts of this thesis. Thus, we do not expect a qualitative difference in the outcome of the simulations.

For the remaining parameters of the simulation (see table 2.1), in particular the detachment forces ($F_{d,ps}$ and $F_{d,pp}$), the detachment times ($t_{d,ps}$ and $t_{d,pp}$) and the binding rates ($\gamma_{att,ps}$ and $\gamma_{att,pp}$), we sampled over different values. The values over which we sampled are given in appendix F.

PARAMETER	VALUE	REF.
Cocci radius R	0.5 μm	[28]
Cocci distance d_{cocci}	0.6 μm	[28]
Cell-cell excl. vol. const. k_{cc}	2×10^4 pN μm^{-1}	
Cell-sub. excl. vol. const. k_{cs}	4×10^4 pN μm^{-1}	
Translational mobility μ_{trans}	1 μm $(s\ pN)^{-1}$	
Rotational mobility μ_{rotat}	2 $(\mu m\ s\ pN)^{-1}$	
Pilus persistence length l_{pers}	5 μm	[31]
Pili production rate γ_{prod}	15 Hz	[34]
Maximal pili number N_{max}	15	[35]
Pili protrusion velocity v_{pro}	2 μm/s	[23, 28]
Pili retraction velocity v_{ret}	2 μm/s	[23, 28]
Mean pili length l_c	1.5 μm	[28]
Pili spring constant k_{pili}	2000 pN/μm	[100, 101]
Pili stalling force F_{stall}	180 pN	[23, 34]
Pili-pili detachment force $F_{d,pp}$		
Pili-sub. detachment force $F_{d,ps}$		
Pili-pili detachment time $t_{d,pp}$		
Pili-sub. detachment time $t_{d,ps}$		
Pili-pili binding rate $\gamma_{att,pp}$		
Pili-sub. binding rate $\gamma_{att,ps}$		

Table 2.1: Parameters of the computational model. The upper half shows parameters that could either be estimated from experiments or did not affect the outcome of the simulations as long as they were chosen high enough. The lower half shows parameters that were sampled (see appendix F).

3

MOTILITY OF SINGLE BACTERIA ON A SUBSTRATE

Many bacterial cells and microcolonies use type IV pili to attach to different substrates, for example epithelial cells [15] or glass and plastic surfaces [28, 34, 59]. By retracting attached pili, the cells create pulling forces and using these forces, they mediate their motility on the substrate.

Experimentally, it was shown that *Neisseria gonorrhoeae* bacteria moving on a BSA-coated glass substrate exhibit a persistent random motion. The characteristic length of the motion is higher than the average length of the pili [27]. Previously, it was suggested that this behavior cannot be solely explained by a tug-of-war mechanism, known to exist for the bidirectional transport by molecular motors [38]. Instead, it was suggested that one needs to consider directional memory in the form of bundling of multiple pili and correlations between the originating points of pili [34]. Here, we use our computational model (see chapter 2) to study whether we can reproduce the persistent motion over lengths higher than the average pilus length. To this end, we do not consider any process that could account for directional memory [34]. Additionally, a one-dimensional stochastic model highlighting an underlying tug-of-war mechanism provides us with an intuitive understanding of the persistent motion.

Furthermore, we study how the number of pili per cell affects the motion of cells. Experimentally, it has been shown that the more pili a cell possesses, the higher is the persistence time and the diffusion coefficient of a cell [27]. Previous computational models were not able to reproduce such behavior without including directional memory of the pili [34].

For single cell motion on top of a plastic surface it was shown that the distribution of velocities is bimodal and that cells having the shape of a diplococcus have a higher probability to move in the direction perpendicular to their long axis [28]. Here, we use our computational model to address this question.

Studied parameter sets

If not stated otherwise we use the parameters given in table 2.1 while applying the computational model and as input to our stochastic model. Although we investigated a wide range of parameter sets by sampling over different values of the attachment rates, detachment forces and detachment times (see table F.2), here we present only two of them, given in table 3.1. These sets represent different regimes of how cells use pili to move on a substrate.

For the first parameter set, called *slow* (short for slow binding and unbinding dynamics), pili bind strongly but with a low rate to the

substrate. In this regime, we assume that pili rarely attach to the surface and we assume that the force-dependent detachment rate is given by

$$\gamma_{det}^{(sub)}(F) = \frac{1}{t_{d,ps}^{(1)} \exp\left(-\frac{F}{F_{d,ps}^{(1)}}\right)}, \tag{3.1}$$

as motivated by the Kramers rate (see subsection 2.3.2). Here, F is the pulling force, $t_{d,ps}^{(1)}$ is called the detachment time and $F_{d,ps}^{(1)}$ is the detachment force.

	SLOW	FAST
$F_{d,ps}^{(1)}$ [pN]	180	1.28
$F_{d,ps}^{(2)}$ [pN]	—	33.8
$t_{d,ps}^{(1)}$ [s]	10	0.85
$t_{d,ps}^{(2)}$ [s]	—	0.04
$\gamma_{att,ps}$ [s^{-1}]	0.5	15
μ_{trans} [$\mu m\ (s\ pN)^{-1}$]	1	10
μ_{rotat} [$(\mu m\ s\ pN)^{-1}$]	2	20

Table 3.1: Definition of pili-substrate-interactions parameter sets and the mobilities used for modeling the substrate motion of cells.

The second parameter set, called *fast* (short for *fast binding and unbinding dynamics*), is motivated by experiments in which the mean detachment time of a pilus attached to a BSA coated silica bead was measured [34]. Trapping the glass bead in an optical tweezer allowed to create a drag force acting on the pilus. In the experiment, the detachment rate was found to follow

$$\gamma_{det}^{(sub)}(F) = \frac{1}{t_{d,ps}^{(1)} \exp\left(-\frac{F}{F_{d,ps}^{(1)}}\right) + t_{d,ps}^{(2)} \exp\left(-\frac{F}{F_{d,ps}^{(2)}}\right)}, \tag{3.2}$$

with a second characteristic time $t_{d,ps}^{(2)}$ and a second characteristic force $F_{d,ps}^{(2)}$. For the *fast* parameter set, the detachment rate depends on more parameters. In general, the detachment times and forces are considerably smaller, compared to those chosen for the *slow* parameter set. The attachment rate was chosen to be higher than those of the *slow* parameter set. For the *fast* parameter set we assume that pili only bind weakly to the substrate, but will frequently attach to a substrate.

Contrary to the previously defined values of the parameters of the computational model, given in table 2.1, here we chose higher values of the mobilities of the cells, corresponding to smaller frictions, for the *fast* parameter set. The chosen values correspond to the friction of a cell moving within water. We pick higher values of the mobilities because of the low values of the detachment forces of the

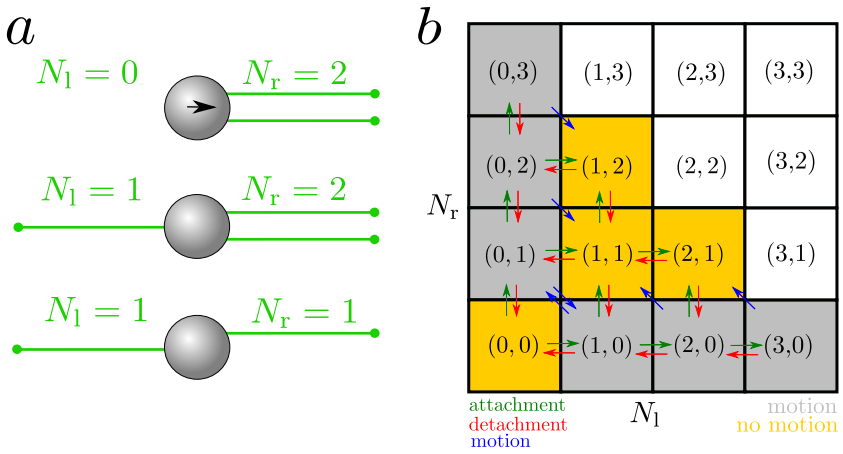

Figure 3.1: (a) Sketch of the stochastic model of cell surface motion. The cell possesses in total 3. The number of pili bound to the left side is given by N_l, the number of pili bound to the right side is given by N_r. The pili can constantly change between states of attachment and detachment, as predicted by the stochastic model. (b) States and transitions of the stochastic model for a cell with three pili on each side. The arrows show the transition between the different states (N_l, N_r), in particular due to attachment of pili, the detachment of pili and the motion of the cell over pilus attachment points. In the model, we assume a cell is moving if a nonzero number of pili is attached only to one side.

fast parameter set. As computed in appendix D.1.1, for a translational friction of $\mu_{trans} = 1\ \mu m\ (s\ pN)^{-1}$, the drag force of a single pilus pulling a cell is given by approximately 2 pN, thus being in the order of the detachment forces, shown in table 3.1. For a mobility $\mu_{trans} = 10\ \mu m\ (s\ pN)^{-1}$, the force only has a value of approximately 0.2 pN, being one order of magnitude smaller than the detachment forces. For the *slow* parameter set, we do not observe any difference for the lower and the higher value of the translational and rotational mobility.

3.1 STOCHASTIC MODEL OF BACTERIAL MOTILITY ON A SUBSTRATE

We apply our computational model, presented in chapter 2, to study the substrate motion of single cells. In addition to this model, we use a mathematical model to investigate the underlying mechanisms of substrate motility of single cells. A simple one-dimensional stochastic model allows us to easily study the tug-of-war mechanism.

The stochastic model, described in this section, shares similarities to a previously published work by Müller et al. [38]. They suggest a stochastic model to study the bidirectional transport of cargo due to two populations of molecular motors, kinesin and dynein, pulling in different directions and having load-dependent transport properties.

In the one-dimensional stochastic system a cell possesses $N_{total} \in \mathbb{N}$ pili on each side, N_l pili being attached on the left side and N_r pili being attached on the right side (see figure 3.1a). Then, we define a

state (N_l, N_r) and study transitions between different states and their effect on the motion of the cell.

In order to compute the probability $P(N_l, N_r)$ one needs to know the transition rates between the different states. An overview over the different transitions that are possible within our stochastic model is shown in fig 3.1b and discussed in the following. The resulting master equation takes the form

$$\frac{dP(N_l, N_r)}{dt} = \sum_{i=0}^{N_{total}} \sum_{j=0}^{N_{total}} T_{lr,ij} P(i,j), \tag{3.3}$$

with the transition matrix T, consisting of all rates describing the transitions between the different states

$$(i,j) \to (N_l, N_r)\,. \tag{3.4}$$

Transition due to the attachment of pili to the substrate

We will consider cells with N_l and N_r attached pili on the left and right side respectively. The attachment of an individual pilus is described by the following transitions

$$(N_l, N_r) \to (N_l + 1, N_r)\,, \tag{3.5}$$
$$(N_l, N_r) \to (N_l, N_r + 1)\,. \tag{3.6}$$

For an individual cell

$$N_{free} = N_{total} - N_l - N_r \tag{3.7}$$

pili are not attached and can bind to the surface. Then the rates of the transitions defined in 3.5 are given by

$$\gamma_a^{(l)} = N_{free}\gamma_{att}, \tag{3.8}$$
$$\gamma_a^{(r)} = N_{free}\gamma_{att}, \tag{3.9}$$

with the pilus attachment rate γ_{att}. Here, we allow the cell to have all pili attached to one side. The transitions mediated by attachment of pili are visualized in figure 3.1b for cells.

Transitions due to the detachment of pili

Again, the cell has N_l pili attached to the left side and N_r pili attached to the right side. The detachment of a pilus corresponds to the transitions

$$(N_l, N_r) \to (N_l - 1, N_r)\,, \tag{3.10}$$
$$(N_l, N_r) \to (N_l, N_r - 1)\,. \tag{3.11}$$

The detachment rate of pili is load-dependent. Before we can define the rates for the transitions caused by pilus detachment, we first need to compute the forces acting on the pili as a function of N_l and N_r.

For a pilus we know that the characteristic force is given by F_{stall} (see equation 2.3). Here, we assume that for a given configuration (N_l, N_r) the pilus switches instantaneously to the stationary state, as computed in appendix D.1. This corresponds to an infinitely large spring constant k_{pili} of the pili.

For the case that the same number N of pili is attached to the left and right size, the drag forces $F_l(N_l, N_r)$ and $F_r(N_l, N_r)$ acting on the individual pili on the left or right side are given by

$$F_l(N, N) = F_{stall}, \tag{3.12}$$

$$F_r(N, N) = F_{stall}, \tag{3.13}$$

thus, the pili reach their stalling force F_{stall} (see equation 2.3). When they have reached this force, they can no longer retract and the system reaches a stationary state. See appendix D.1.2 for more information.

If pili are only attached to one side (left or right), the individual pili pulling forces are given by

$$F_l(N_l, 0) = \frac{F_{stall}}{1 + \frac{F_{stall}\mu_{trans}N_l}{v_{ret}}}, \tag{3.14}$$

$$F_r(0, N_r) = \frac{F_{stall}}{1 + \frac{F_{stall}\mu_{trans}N_r}{v_{ret}}}, \tag{3.15}$$

as derived in appendix D.1.1. Here, the dynamic parameters (the translational mobility μ_{trans} of the cell and the pilus retraction velocity v_{ret}) affect the magnitude of the force because the cell is moving while being in this state. If we estimate the values of all parameters characterizing this force we see that

$$\frac{F_{stall}\mu_{trans}}{v_{ret}} \gg 1, \tag{3.16}$$

so that the resulting forces are usually very small.

The last case we need to consider is attachment of pili on both sides, but with $N_l \neq N_r$. In appendix D.1.3 we show that the drag forces of single pili are then given by

$$F_l(N_l, N_r) = F_{stall} \max\left[1, \frac{N_r}{N_l}\right], \tag{3.17}$$

$$F_r(N_l, N_r) = F_{stall} \max\left[1, \frac{N_l}{N_r}\right]. \tag{3.18}$$

Now we can compute the pilus detachment rate $\gamma_{det}^{(sub)}(F)$ of an individual pilus on the left or right side, given in equation 3.1 and equation 3.2.

The transition rates are then given by

$$\gamma_d^{(l)} = N_l \gamma_{det}^{(sub)}(F_l), \tag{3.19}$$

$$\gamma_d^{(r)} = N_r \gamma_{det}^{(sub)}(F_r). \tag{3.20}$$

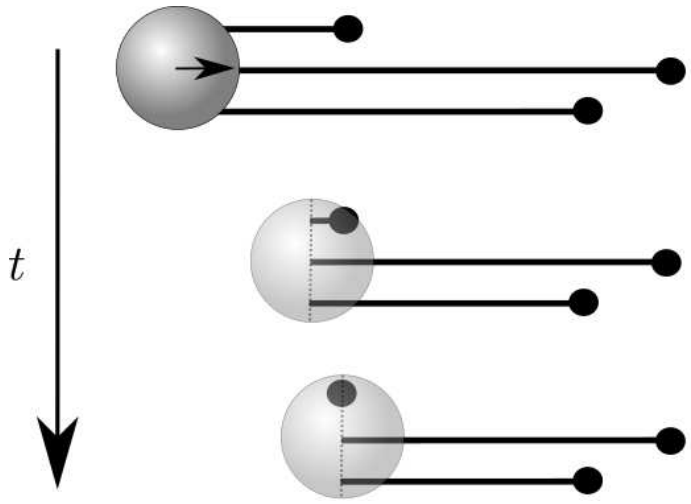

Figure 3.2: Sketch of the transition of pili states due to motion over a pilus attachment point. Initially, all pili are on the right side and pull on the cell. Due to the motion of the cell and the different distances of the pilus attachment points to the cell, at some point the cell moves over one of the pilus attachment points. In the stochastic model we assume that this switches the pilus from the right side to the left one.

Transitions due to the motion of the cell

Next to attachment and detachment, the state (N_l, N_r) can also change due to the motion of the cell in the following way:

$$(N_l, 0) \to (N_l - 1, 1)\,, \tag{3.21}$$

$$(0, N_r) \to (1, N_r - 1)\,. \tag{3.22}$$

This results from the motion of the cell over an attachment point of a pilus (see figure 3.2). A cell can only move if all pili are bound to one side (see next chapter). The attachment points of the pili have the mean distance L from their start points. If we assume that these lengths are exponentially distributed with the mean length L, then the closest pilus has, on average, a distance $\frac{L}{N}$, if N pili are attached. If a cell moves with the velocity v_c, it needs the time $t_v = \frac{L}{N v_c}$ to move over a pilus. Then the rates of the transitions are given by

$$\gamma_m^{(l)} = \frac{N_l v_c}{L}, \tag{3.23}$$

$$\gamma_m^{(r)} = \frac{N_r v_c}{L}. \tag{3.24}$$

Here, we assume that a pilus cannot retract to a zero length while being attached, because at least the domain of the pilus attached to the substrate needs to point out of the cell membrane. Thus, we assume that even a short pilus can still make the transition from one side to the other one.

How we compute the velocity of the cell v_c is shown in the following paragraph.

Describing the motion of the cell

Due to the instantaneous relaxation of pili, corresponding to a large pili spring constant $k_{pili} \longrightarrow \infty$, the cell can only move when all pili are attached on one side, so that we either have a state $(N_l, 0)$ or $(0, N_r)$ (see appendix D.1). A cell will always move in the direction in which the pili are attached, thus it will move to the left for states $(N_l, 0)$ and to the right for $(0, N_r)$.

In appendix D.1.1 we show that the velocity of a cell v_c, having N pili attached on one side, is given by

$$v_c = \frac{v_{ret}}{1 + \frac{v_{ret}}{F_{stall} N \mu_{trans}}}, \tag{3.25}$$

with the pilus retraction velocity v_{ret}, the characteristic pilus force F_{stall} and the translational mobility μ_{trans} (see chapter 2 for a definition of these quantities). By estimating the values of all parameters as close to the experiment as possible for individual cells we have

$$\frac{v_{ret}}{F_{stall} N \mu_{trans}} \ll 1, \tag{3.26}$$

so that the cell velocity of single cells could be approximated by $v_c \sim v_{ret}$.

Solving the stochastic model

In order to compute the steady state solution $P(N_l, N_r)$ of the probability of states (N_l, N_r) we need to write down the complete transition matrix T and set

$$\frac{dP(N_l, N_r)}{dt} = 0 \tag{3.27}$$

for all states (N_l, N_r). This system of equations can be solved numerically with Matlab R2015a.

In order to compute a trajectory of the cells we apply a Gillespie algorithm [102, 103], allowing us to estimate quantities like the mean squared displacement and the velocity autocorrelation function. Therefore, we assume that the transition rates correspond to Poisson processes where, for a given rate γ, the time t of the next event is given by

$$p(t) = \gamma \exp(-\gamma t). \tag{3.28}$$

The algorithm then has the form

1. Compute the six transition times for all three processes (attachment, detachment and the motion transition) from the exponential distribution of times.
2. Pick the smallest transition time.
3. Execute the transition of the smallest transition.

4. Compute the new position of the cell and save the time.
5. Go back to step 1.

We verified that the probability of states agrees with the solution of the system of equations.

Estimating the parameters of the stochastic model

The parameters of the stochastic model, specifically the number of free pili N_{total}, the attachment rate γ_{att} and the mean pili length L, do not necessarily need to coincide with the parameters of the computational model (see table 2.1 and table 3.1). Due to the three-dimensional shape of the cell, a pilus emerging from the cell membrane, first needs to be long enough to reach the substrate, reducing the mean attachment rate of the pili.

In chapter C we will present a simple geometric model that allows us to estimate those parameters as a function of the cell/colony size and the parameters corresponding to the computational model. In this model, we neglect that a cell has the shape of a diplococcus. Instead, we assume that a cell has a spherical shape of radius $R = 0.7$ μm (as estimated in appendix F.3.2 for a single cell) and 15 pili grow stochastically from its surface. The pili protrude perpendicularly from the cell surface, until they collide with the substrate. From this point on, they will slide along the substrate, analogously to the computational model. By considering the mean length of pili, the pilus velocities and the attachment rate of the pili tips (all taken from table 2.1 and table 3.1), we can estimate the effective attachment rate of pili and the mean displacement a pilus is able to mediate on the substrate. The predicted values for the two parameter sets (*slow* and fast) are given in table 3.2. For both parameter sets we observe effective attachment rates γ_{att} that are smaller than the pilus attachment rate $\gamma_{att,ps}$ with the substrate. This results from the fact that each pilus first needs to protrude a certain distance before it collides with the substrate.

	SLOW	FAST
γ_{att} [s^{-1}]	0.09	1.95
L [μm]	1.58	0.59

Table 3.2: Parameters of the stochastic model of cell motility on a substrate, estimated from geometric considerations.

For the mean displacements on the substrate L a pilus can mediate, we observe that the value is larger for the *slow* parameter set, compared to the *fast* parameter set. This behavior originates from the fact that for higher attachment rates, pili will attach within a short time after bringing its tip in the vicinity of the substrate. After attachment, they will immediately start to retract, thus a higher attachment rate corresponds to a shorter mean length of the pili.

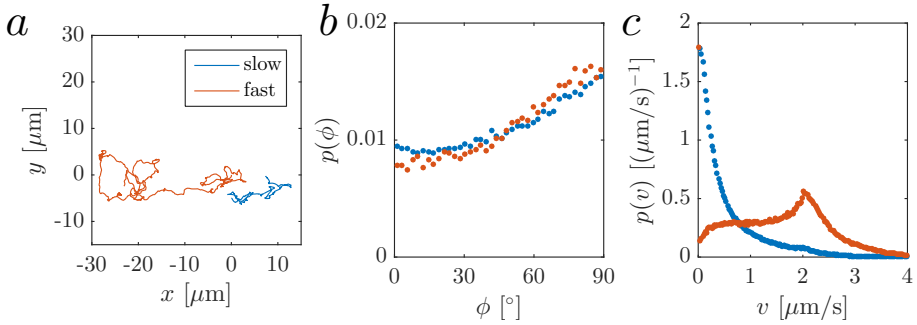

Figure 3.3: (a) Trajectories of *in silico* cell, resulting from the computational model, for the *fast* and *slow* parameter set. (b) Distribution of angles between the direction of motion of a cell (projected on the substrate) and its long axis. Here, 0° corresponds to a motion parallel to the long axis and 90° to a motion perpendicular to the long axis, connecting the two spheres of the diplococcus. (c) Histogram of velocities for both parameter sets.

3.2 COMPARISON OF THEORY AND EXPERIMENT

Now, we will use the presented modeling approaches (the computational model presented in chapter 2 and the stochastic model discussed in chapters 3.1) to study the motility of single cells on a substrate.

We will investigate the motion of single cells and the origin of persistent motion over length scales larger than the length of individual pili [27, 28, 34]. In particular, we will study how a simple tug-of-war mechanism can induce such behavior.

Afterwards, we will study how the pili number affects the motion of individual cells and show that cells with more pili can exhibit a more persistent motion, in agreement with experimental observations [27].

3.2.1 *The role of pili dynamics during the motility of single cells*

Here, we study how individual cells use type IV pili to move on top of a substrate. We first use our computational model (see chapter 2) to study the motility of cells for two different parameter sets, given in table 3.1. The parameters used for our simulations are given in table 2.1. Information about the simulation details are given in appendix F.1. Examples of trajectories projected on the substrate are shown in figure 3.3a.

We first study the distribution of angles between the direction of motion and the long axis of the dumbbell-shaped cell. Experimentally, it was shown that cells prefer to move in the direction perpendicular to their long axis. In our simulations, we see the same behavior for both parameter sets (see figure 3.3b). The intuitive explanation for this behavior is the fact that due to the diplococcus shape, a cell has more pili in the direction perpendicular to its long axis, compared to the direction parallel to its long axis. The more pili a cell possesses, the more likely it is that any pilus attaches in this direction, thus mediating motion in the direction of the attachment point.

From the trajectories, we compute the histogram of absolute velocities of the cells (see figure 3.3c), which exhibits a bimodal behavior similar to cells moving on a plastic substrate coated with BSA [28]. It was shown experimentally that the velocity possessed two peaks, one at 0 μm/s and another peak at a non-zero velocity. In our simulations, we observe a not so pronounced bimodal behavior of the distribution of velocites for the *slow* parameter set. The probability density function decreases with increasing velocities and only exhibits a small peak for the velocity 2 μm/s, corresponding to the characteristic pilus retraction velocity and most likely results from phases where only a single pilus is attached to the substrate. For the *fast* parameter set we observe a different behavior. For 2 μm/s, which is the characteristic pilus retraction velocity v_{ret}, we observe a pronounced peak in the velocity histogram. For 0 μm/s we see another peak, corresponding to a cell that is not moving. Velocities that are larger than the pilus retraction velocity do appear frequently. The origin of this surprising behavior is geometrical. Short retractions of multiple pili can correspond to large displacements of the cell. Thus, while a pilus may retract with the velocity v_{ret}, the cell can move with a higher velocity. This effect is discussed in more detail in appendix D.2. The zero velocity peak for the *fast* parameter set could either originate from the fact that many pili are attached to the substrate and the cell is trapped between them or from a situation where no pilus is attached.

In order to answer this question, we can study quantities that are not so easily accessible in experiments with the help of our theoretical models. More specifically, we can investigate the number of pili that are attached to the substrate and generate an active pulling force (see figure 3.4a) and how this number is changing with time.

For the distribution of the number of attached pili (generating a nonzero pulling force) we observe that the average number is larger for the *slow* parameter set, characterized by strong pili-substrate interactions, compared to the *fast* parameter set with very small pili-substrate detachment forces $F_{d,ps}^{(1)}$ and $F_{d,ps}^{(2)}$. For the *fast* parameter set we observe that in roughly 30 % of the cases there are no pili are attached to the substrate. In this case, the cell is not able to move, thus explaining the peak for zero velocity in the velocity histogram (figure 3.3b). While this result first appears counter-intuitive because it was assumed that cells use pili to move while being permanently attached to a substrate, it was shown experimentally that cells sometimes do not have pili on a glass surface coated with poly-D-lysine or collagen [24]. Additionally, we were computing the mean velocity of a cell as a function of the number of attached pili (generating a nonzero force). For the *slow* parameter set we observe that the cell is the fastest when only one pilus is attached to the substrate. In this case, the cell moves in the direction of this pilus with the characteristic pilus velocity v_{ret} until the length of the attached pilus becomes zero. For larger number of pili however, it appears to be more likely that pili pull in opposite directions and thus trap the cell. For the *fast* parameter set we observe the highest velocity for 2-3 attached pili. This behavior must result from collective interactions of the pili that in-

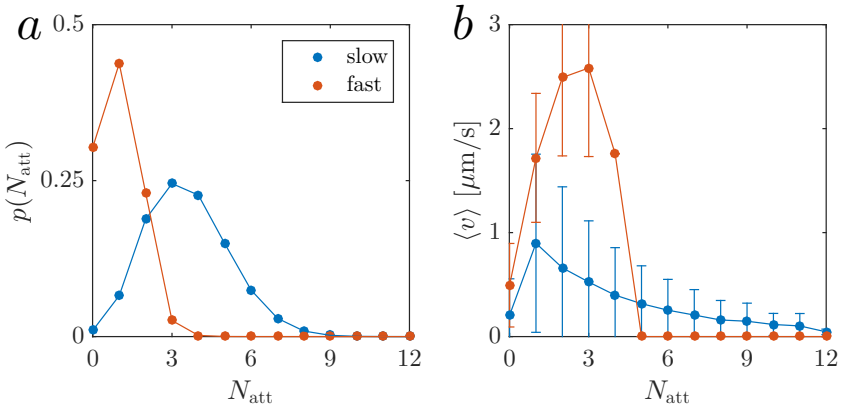

Figure 3.4: (a) Distribution of attached and actively pulling pili for a single cell moving on a substrate. (b) Mean velocity of a cell moving on a substrate as a function of its current number of attached pili. Here, we only count those attached pili that are generating a pulling force and thus participate in the motion of the cell. The error bars show the standard deviation, a measure for the width of the distribution of velocities. For both parameter sets we observe also a non-zero velocity for the case that no pilus is attached. This results from the fact that we compute the velocity from the displacement of the cell within the time interval $\Delta t = 0.5$ s. In this time a pilus can easily attach, mediate a motion and detach.

crease the velocity of the cell, for example by a process discussed in appendix D.2.

From the trajectories, we can also characterize the statistical properties of bacterial motion on a substrate, specifically the mean squared displacement and the velocity autocorrelation function (see figure 3.5).

By computing the mean squared displacement of individual cells for both parameter sets (see figure 3.5a) we observe a diffusive behavior for large times. For this limit, we can compute the diffusion coefficient D, resulting from

$$\mathrm{MSD}(\Delta t) = \langle [\mathbf{r}(t+\Delta t) - \mathbf{r}(t)]^2 \rangle_t \simeq 2d D \Delta t, \tag{3.29}$$

and given in table 3.3. Here, $\mathbf{r}(t)$ is the time-dependent trajectory of the cell, projected on the substrate. The parameter d is the dimensionality of the system, defined to be $d = 2$ because we only consider the motion parallel to the substrate. The values of the diffusion coefficient give a quantitative proof that the cells for the *fast* parameter set are more motile than those of the *slow* parameter set. For short time intervals we observe a superdiffusive behavior, which corresponds to a persistent motion with a characteristic time t_{char}. In order to estimate this characteristic time, we computed the velocity autocorrelation function (see figure 3.5b), described by

$$\mathrm{VACF}(\Delta t) = \langle \mathbf{v}(t+\Delta t)\mathbf{v}(t) \rangle_t = v_{char}^2 \exp\left(-\frac{\Delta t}{t_{char}}\right), \tag{3.30}$$

with the vectorial particle velocity $\mathbf{v}(t)$, the correlation time t_{char} and the characteristic velocity v_{char} (see chapter 1.2). The characteristic

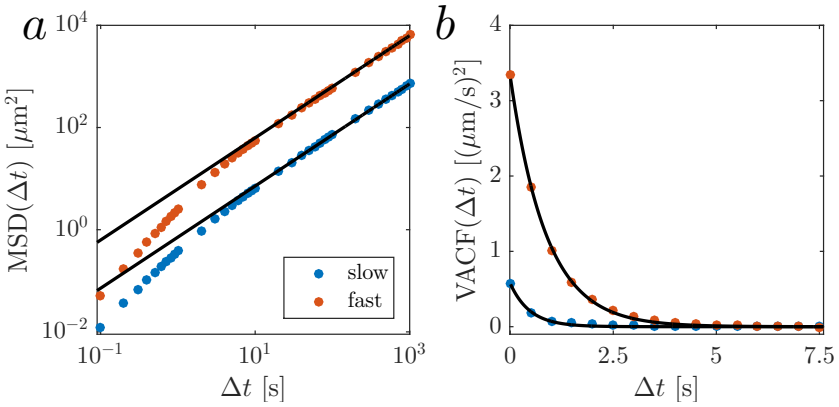

Figure 3.5: (a) Time averaged mean squared displacement of *in silico* single cells moving on a substrate for the parameter sets, given in table 3.1. The black lines show fits of equation 3.29, given in table 3.3. (b) Time averaged velocity autocorrelation function of *in silico* single cells moving on a substrate. The black lines show fits of equation 3.30, where the parameters are given in table 3.3.

	SLOW	FAST
t_c [s]	0.48 ± 0.09	0.87 ± 0.04
v_c [μm/s]	0.76 ± 0.04	1.83 ± 0.02
D [μm²/s]	0.18 ± 0.03	1.57 ± 0.03

Table 3.3: Fitting results of the MSD and VACF of single cell motion on a substrate from the computational model.

times and velocities for the two parameter sets are given in table 3.3. From them, we can compute the characteristic length scale of motion

$$l_{char} = v_{char} t_{char}. \tag{3.31}$$

The mean pili length l_c was chosen to be 1.5 μm in the computational model. For the *slow* parameter set we compute a value around 0.36 μm, thus being considerably smaller than the mean pili length. For the *fast* parameter set we get a length scale of roughly 1.6 μm, thus being slightly larger than the characteristic pilus length that was taken as an input to the model and pointing in the direction of persistent motion that, due to the collective interactions of pili, can exceed the length of individual pili. By comparing these numbers to the experimental values [27], $t_{char} = 1.4 \pm 0.2$ s, $v_{char} = 1.6 \pm 0.1$ μm/s and $l_{char} = 2.2$ μm, we see that the persistence is weaker in our computational model. In subsection 3.2.2 we suggest that this behavior may originate from a underestimation of pili numbers such that a cell possesses possibly more than 15 pili. For higher pili numbers, the persistence can increase and reach lengths that are comparable to the experimental results.

Before we move to the stochastic model, we want to discuss the experiments that lead to the conclusion that cells exhibit persistent

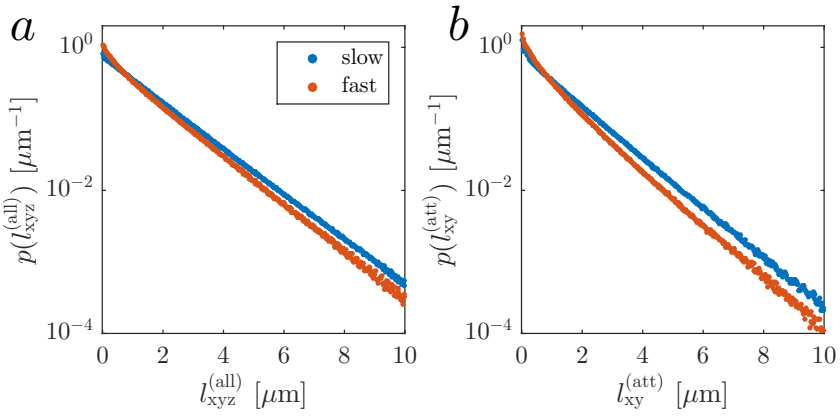

Figure 3.6: Distribution of pili lengths of an *in silico* cell on a substrate. (a) Distribution of the distance of the pili start and end point of all pili. (b) Distribution of the distance of the pili start and end point projected on the substrate of attached pili.

	SLOW	FAST
$\langle l_{xyz}^{(all)} \rangle$ [μm]	1.35	1.16
$\langle l_{xy}^{(att)} \rangle$ [μm]	1.15	0.93

Table 3.4: Mean pili lengths as predicted by the computational model.

motion over distances larger than the mean pili length and want to discuss which pilus length is measured experimentally. Therefore, we were computing the mean pilus length of all pili from our simulations (see figure 3.6). We use two different definitions of the pili length. In the first definition we compute the length of all pili, attached and free, by computing the distance between their start point and end point in three dimensions, called $l_{xyz}^{(all)}$. For the second definition we try to be as close to the experiment as possible, where the pilus length is measured by transmission and electron microscopy [27, 28]. The preparation of the samples could affect the pili, especially those that were not attached to the substrate. They may break, bend or just detach from the cell, but most likely will not keep the position that they had before sample preparation. Additionally, in the experiment one is only measuring the pilus length projected on the substrate. Thus, we define the second length $l_{xy}^{(att)}$ as the distance of the start and end point of attached pili projected on the substrate, called $l_{xy}^{(att)}$. The distribution of these lengths are shown in figure 3.6 for both parameter sets.

By computing the mean values from those distributions (see table 3.4) we find that all lengths are smaller than the mean pili length $l_c = 1.5$ μm that was picked as an input parameter of the simulation. Thus, we suggest that in experiments one does not measure the real mean pili length l_c which is only dependent on the pilus velocity and the rate of switching from the assembly state of the polymer to its disassembly state, but instead we measure the lengths of pili affected by attachment and detachment. The discrepancy between the input

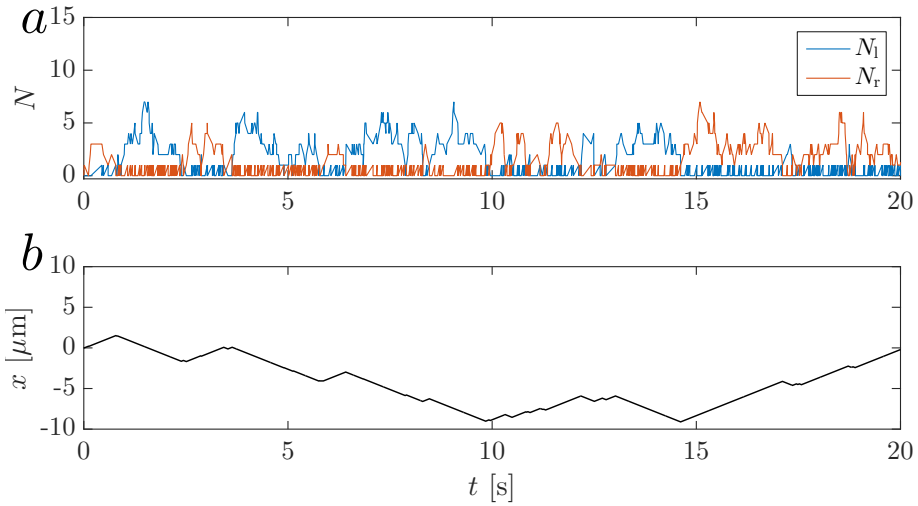

Figure 3.7: Trajectory of a cell moving on a substrate computed by the stochastic model for the *fast* parameter set. (a) Attached pili on the left side, N_l, and on the right side, N_r. (b) Trajectory x of a cell as a function of time t.

length l_c of the model and the measured characteristic pili length originates from the switching from protrusion to retraction of pili after attachment [35]. Considering these effects, in our simulations we find values comparable to those measured experimentally, ranging from 0.9 µm [27] to 1.2 µm [28].

If we assume that the lengths measured experimentally correspond to $l_{xyz}^{(all)}$ or $l_{xy}^{(att)}$, than the measured characteristic length of the persistent motion, estimated to be around 1.6 µm for the *fast* parameter set is considerably higher as the measured length. We clearly observe a persistence over lengths higher than the measured pili length, as suggested from experimental measurements [27].

While the computational model exhibits excellent qualitative and even quantitative agreement to experimental data, due to its complexity it is hard to really understand the processes that drive such behavior. Our weapon of choice to study the underlying processes is a simplified stochastic model, introduced in chapter 3.1.

Here, we study the motion of a cell in one dimension. All parameters either agree with the computational model discussed previously or were estimated as shown in section 3.1 and appendix C.

First, we applied a Gillespie algorithm to construct a trajectory of the cells. An example of such a trajectory is shown in figure 3.7 for the *fast* parameter set. Here, one can see that the cell exhibits phases where more than three pili are attached on one side, while on the other side none or only one pilus is attached. In this case, the cell is moving in the direction of the higher number of attached pili. After a certain time, the cell is able to escape such a state and the dominant side can switch.

We can also compute the probability distribution of states, either by analyzing the trajectories computed by the Gillespie algorithm or by solving the transition matrix. The result is shown in figure 3.8. For

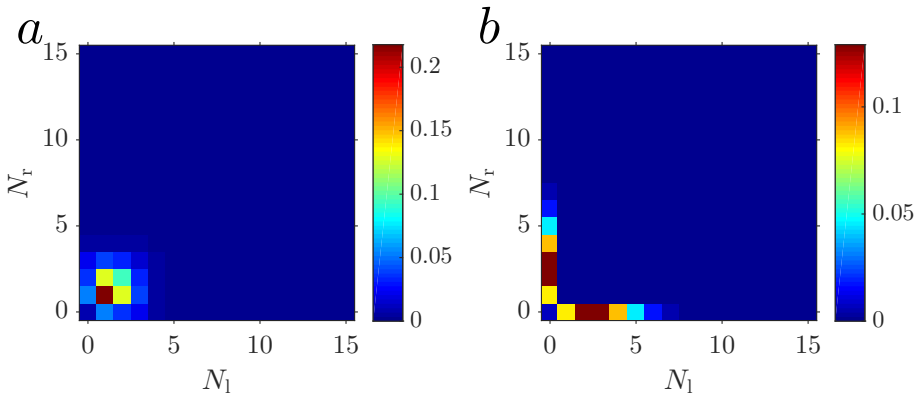

Figure 3.8: Probability of states of a single cell for the stochastic model, for the (a) *slow* parameter set and the (b) *fast* parameter set. The color bar corresponds to the probability of the states.

the two parameter sets we see completely different kinds of behavior. While the cells following the *slow* parameters have the highest probability to have pili attached on both sides at the same time, for the *fast* parameter set cells preferentially have pili only on one side. This observation can explain why cells for this parameter set are more motile, as predicted by the computational model, and agrees with the behavior observed in figure 3.7.

In order to check for consistency, we compute multiple quantities that were previously investigated using our computational model.

We started with the velocity histogram (see figure 3.9a). For the *slow* parameter set we observe a large peak for a zero velocity and a smaller peak for a velocity of roughly 2 µm/s, corresponding to the characteristic pilus retraction velocity. Due to the discrete nature of states in the model, all other velocities have negligible probabilities. The observed behavior shows qualitative agreement to the one observed for the computational model (see figure 3.3b). For the *fast* parameter set we only observe a peak for 2 µm/s, corresponding to the persistent motion of the cell in one direction.

The stochastic model predicts that in less than 5% of time no pilus is attached to the surface. This can be also seen in figure 3.9b where we show the histogram of attached pili. The distributions for both parameter sets, in agreement to the computational model, differ such that on average more pili are attached for the *slow* parameter set.

Additionally, we can compute the mean squared displacement and the velocity autocorrelation function for the one-dimensional trajectories and from them estimate the diffusion coefficient D of the cellular motion and the characteristic velocity v_{char} and time t_{char} of the persistent motion. Analogously to the results of the computational model, we observe a diffusive regime for large times for the mean squared displacement (see figure 3.3c), from which we computed the diffusion coefficient D, given in table 3.5. The values have the same order of magnitude as those computed from the trajectories simulated by the computational model (see table 3.3). Again, the cells following

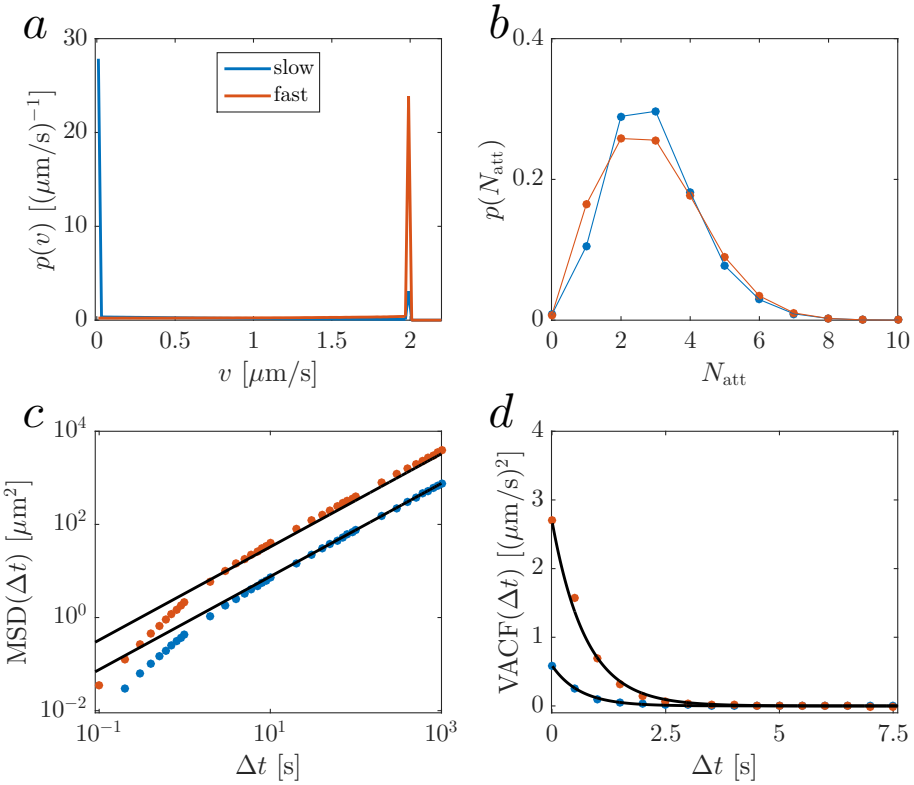

Figure 3.9: Statistical properties of single cell motion, computed from the stochastic model. (a) Histogram of velocities of a cell moving on a substrate for the *slow* and *fast* parameter set (see table 3.1). (b) Probabilities of number of attached pili for a cell moving on a substrate modeled by the stochastic model. (c) Time averaged mean squared displacement of single cells moving on a substrate for the parameter sets, given in table 3.1, as predicted by the stochastic model. The black lines show fits of equation 3.29 with parameters given in table 3.5. (d) Time averaged velocity autocorrelation function of *in silico* single cells moving on a substrate. The black lines show fits of equation 3.30 with parameters given in table 3.5.

	SLOW	FAST
t_c [s]	0.61 ± 0.02	0.74 ± 0.02
v_c [μm/s]	0.77 ± 0.02	1.64 ± 0.02
D [μm²/s]	0.38 ± 0.01	1.64 ± 0.04

Table 3.5: Fitting results of the MSD and VACF of single cell motion on a substrate from the stochastic model.

the *fast* parameter set are considerably faster than those following the *slow* parameter set.

By computing the characteristic times t_{char} and velocities v_{char} from the velocity autocorrelation (see figure 3.3d and table 3.5), we again see qualitative agreement to the computational model. On first sight, the characteristic lengths, having values of 0.47 μm for the *slow* parameter set and 1.21 μm for the *fast* parameter set, are smaller than the persistence lengths computed from in the computational model. If we compare the lengths to the mean pilus displacement L (see table 3.2), we observe that the persistence length for the *fast* parameter set is, indeed, higher than the mean pili length in the stochastic model. This behavior is qualitative similar to the results of our computational model and shows that the suggested tug-of-war mechanism can mediate persistent motion.

3.2.2 *Pili number dependence of the single cell motility*

After studying the substrate motion of a single cell with parameters that were motivated by experiments, we now focus on the pili-mediated motion of bacteria as a function of the number of available pili. Previously, this dependence was studied experimentally by the group of Dr. Berenike Maier (Universität Köln) [27]. They used a derepressible *pilE* strain of *Neisseria gonorrhoeae* and were able to show that the more pili a cell possesses, the longer the characteristic time of the persistent motion.

First, using our computational model, we simulated cells with a fixed number of pili N_{pili} and computed the characteristic time, velocity and length of the motion, the diffusion coefficient and the average number of pili attached to the substrate (see figure 3.10) with the help of our computational model 2.

In our simulations we observe that the diffusion coefficient is rapidly rising with increasing number of pili for the *fast* parameter set. For the *slow* parameter set, the diffusion coefficient is considerably smaller and decreases with increasing number of pili (see figure 3.10a).

Additionally, we computed the characteristic time t_{char} (see equation 3.30 and figure 3.10b) and found that in both cases the times increase with higher pili numbers. For the *fast* parameter set we observe a behavior that is almost identical to experimental results [27].

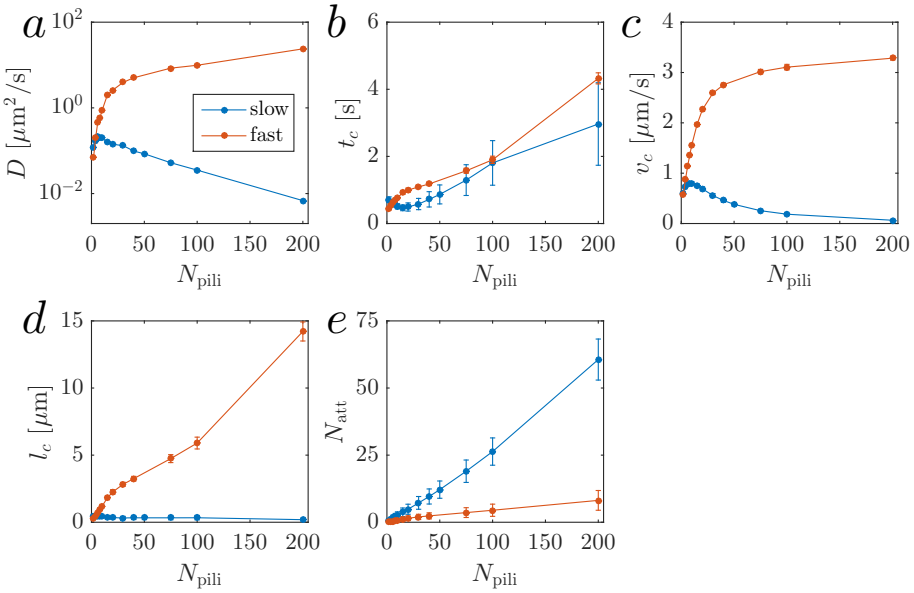

Figure 3.10: Cell motion as a function of the number of pili as modeled by the computational model for the *slow* and *fast* parameter set (see table 3.1). (a) Diffusion coefficient D of an individual cell as function of the number of pili. The diffusion coefficient was estimated from the time-averaged mean squared displacement and fitted with the equation 3.29. (b,c) From the velocity autocorrelation function it was possible to estimate the characteristic time t_{char} and velocity v_{char} of the motion (see equation 3.30). (d) By multiplying the time t_{char} and the velocity vc we computed the characteristic length of the persistent motion of a cell on a substrate. The mean pili length is an input parameter of the simulation and has a value of 1.5 µm, thus for higher numbers the persistent motion can go over length scales considerably longer than the length of individual pili. (e) Mean number of pili attached to the substrate. The error bars show the standard deviation, a measure for the width of the distribution.

The characteristic velocity v_{char} is also increasing for the *fast* parameter set (see figure 3.10c). With a higher number of pili cells move with higher velocities and for longer times in a given direction. Contrary to this behavior, for the *slow* parameter set, the velocity v_{char} is decreasing with increasing number of pili N_{pili}.

From the velocity v_{char} and t_{char} we can also compute the persistence length of motion l_{char} (see figure 3.10d) and see that for the *fast* parameter set this length can clearly exceed the characteristic pili length $l_c = 1.5\ \mu m$. For the *slow* parameter set, the persistence length is smaller than the mean pili length and only changes weakly with pili number.

The last quantity we studied is the average number of pili attached to the substrate (see figure 3.10e). In both cases, the number is increasing with increasing number of pili. Additionally, the numbers for the *fast* parameter set are considerably smaller than those for the *slow* parameter set, resulting from the weaker binding properties that we assume for this parameter set and the constant attachment and detachment of the pili.

In order to understand the origin of the increasing motility with an increasing number of pili, we applied our stochastic model to study the motion of single cells with a changing number of pili. The results are shown in figure 3.11.

Again, we observe that the diffusion coefficient D, the characteristic time t_{char}, the velocity v_{char} and the resulting persistence length of motion l_{char} increase with higher numbers of pili N_{pili} for the *fast* parameter set. For the *slow* parameter set we observe a similar but weaker behavior. This result does not agree with the computational model for the characteristic time t_{char}. Additionally, for the *fast* parameter set, the characteristic time t_{char} increases much faster with increasing number of pili compared to the computational model. This results from the fact that the cell is "locked" in a state where a large number of pili is attached on one side. If a pilus attaches on the other side, it will pull against them and a large force will act on the pilus, forcing it to detach. This process is magnified by the fact that we assume that the detachment rate increases exponentially with force (see equation 3.2). While a similar mechanism can also appear for cells modeled by the computational model, here the cell is not only moving in one dimension but two, and will also be affected by a rotational diffusion. Due to this diffusion, the effective diffusion coefficient and the persistence time t_{char} may decrease and thus could cause the observed behavior. Additionally, the number of attached pili is higher for high numbers of pili for the *fast* parameter set, compared to the *slow* parameter set.

We suggest that the difference of the predictions between the two modeling approaches originate from the neglected pili dynamics in the stochastic model. There, we assume that an attached pilus reaches its final force (computed in appendix D.1) instantaneously. For very low detachment forces, the probability that a pilus detaches before it even comes close to the final force cannot be neglected. We compute the probability density function of detachment times for the

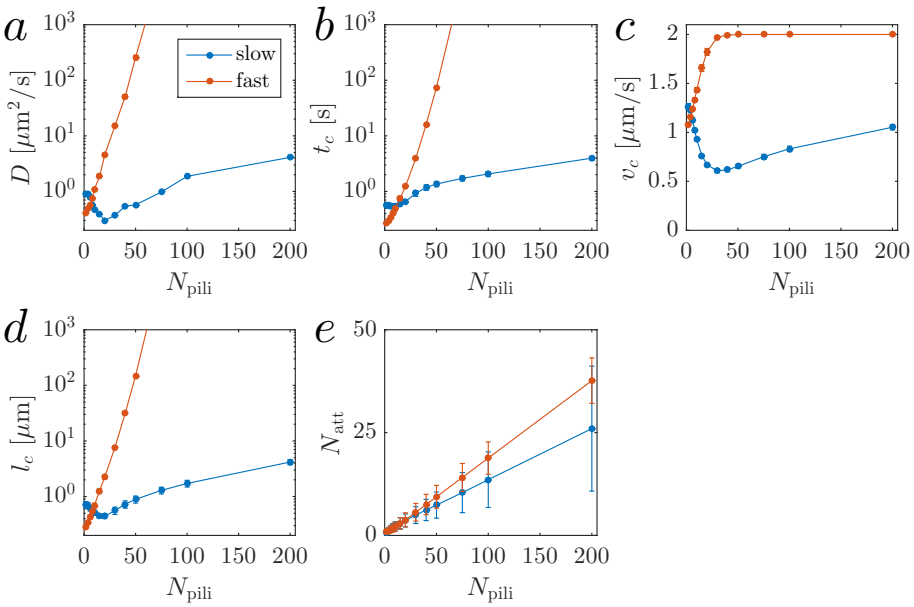

Figure 3.11: Properties of the cell motion as a function of the number of pili as modeled by the stochastic model for the *slow* and *fast* parameter set (see table 3.1). (a) Diffusion coefficient D of a cell as function of the number of pili. The diffusion coefficient was estimated from the time-averaged mean squared displacement and fitted with equation 3.29. The value of the diffusion coefficient for the *fast* parameter set is growing rapidly. (b,c) We used the velocity autocorrelation function 3.30 to estimate the characteristic time t_{char} and velocity v_{char} of the motion. (d) Characteristic length l_{char} of the persistent motion of a cell on a substrate. (e) Mean number of pili attached to the substrate. The error bars show the standard deviation, a measure for the width of the distribution.

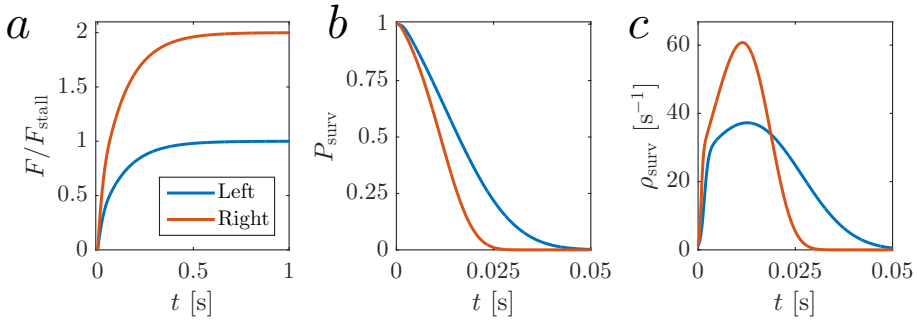

Figure 3.12: Dynamics of pili forces for a single cell. Here, we study the case of a cell having two pili attached to the left side and one pilus attached to the right side. The system and its solution are introduced in appendix D.1. The parameters were taken from table 2.1. Additionally, we study the detachment dynamics given by the *fast* parameter set. (a) Forces as a function of time, as derived in appendix D.1.3. (b) Survival probability of individual pili to not detach from the substrate. (c) Probability density function of survival times.

case where two pili of a single cell are attached on one side and pull against one pilus, attached to the other side. How to compute these forces is shown in appendix D.1.3 and visualized in figure 3.12a. The detachment rate γ_d then follows from equation 3.2. The probability for each pilus on both sides to detach can be obtained from

$$\dot{P}_{\text{surv}}(t) = -\gamma_d(t) P_{\text{surv}}(t), \tag{3.32}$$

$$P_{\text{surv}}(0) = 1. \tag{3.33}$$

The solution of this equation is given by

$$P_{\text{surv}}(t) = \exp\left[-\int_0^t dt'\, \gamma_d\left(t'\right)\right] \tag{3.34}$$

and the result is shown in figure 3.12b. The probability density function of detachment times is then given by

$$\rho_{\text{surv}}(t) = -\dot{P}_{\text{surv}}(t) = \gamma_d(t) \exp\left[-\int_0^t dt'\, \gamma_d\left(t'\right)\right]. \tag{3.35}$$

The resulting distribution is shown in figure 3.12c. This distribution of detachment times does not follow an exponential distribution, as one would expect if the detachment would be described by a Poisson process, but has a more complex shape with peaks around $0.01 - 0.02$ s. If we now estimate the corresponding mean detachment rates of the individual pili, we see that they are in the order of 100 Hz. For a pilus under a load $F_{\text{stall}} = 180$ pN, the detachment rate reaches more than 5000 Hz for the *fast* parameter set in our stochastic model with instantaneous dynamics. Thus, the pili in the computational model are not getting detached from the substrate with such high rates as the ones in the stochastic model. Such a process may be able to reduce the motility of the cell and will reduce its persistent motion.

To summarize this section, we have shown that our models predict an increase of the characteristic time and diffusion coefficient of

bacteria for increasing numbers of pili. The characteristic length scale of motion can exceed the characteristic length of the pili and for cells with $20 - 30$ pili it can reproduce the experimentally observed behavior [27], assuming that in experiments the counted number of pili gives a considerably smaller number than the real number of pili a cell possesses. The origin of this discrepancy may be the sample preparation process for the transmission electron microscope or the fact that only attached pili are counted and free pili are ignored.

3.3 SUMMARY

In this chapter, we presented two different approaches to investigate the motion of individual cells of the bacterium *Neisseria gonorrhoeae* on a substrate. We compared the results of our simulations to published experimental data. We were able to show that the computational model agrees with the experiments.

Previously, it was suggested that the persistent motion of individual cells and the increasing motility with higher numbers of pili requires a mechanism of directional memory, provided by re-elongation of fully retracted pili or bundling of pili [34]. Here, we show that these mechanisms are not needed to generate persistent motion over distances that are larger than the mean length of the pili. In agreement with previous experiments [27], our model is also able to reproduce a increasing motility with higher numbers of pili. This is particularly true for fast binding and unbinding dynamics, suggesting that pili bind weakly to a substrate, but therefore frequently with high attachment rates, compared to the other times scales involved.

The mechanism that is driving the persistent motion of cells is reminiscent of a tug-of-war, a process that was earlier investigated for bidirectional transport by molecular motors [38]. When a single pilus is trying to pull against the side with the larger number of pili, it will feel a larger force and, due to the exponential form of the detachment rate (see equations 3.1 and 3.2), more easily detach on its "weaker" side. Thus, one side will win for a certain time interval, in which the cell moves in this direction. During this time, new pili can attach to the winning side, while shorter pili may detach or switch to the opposite side and detach. This way, there are constantly pili attached on the winning side and the cell moves persistently into one direction. The cell can only escape such an attracting state (many pili on the winning side, no pili on the other side) by stochastically decreasing the number of pili on the winning side such that the pili on the losing side have a chance to take the leading role. While the tug-of-war mechanism is closely related to the one suggested by Müller et al. [38], we expanded their model by introducing a new length scale. This length results from the displacement a pilus can mediate and allows us direct characterization of persistent motion.

In our simulations we found that for fast binding and unbinding dynamics (described by the *fast* parameter set), cells often do not have any pili attached to the substrate. *In vivo*, the cells and colonies are

confronted with strong flows and thus will need to be constantly attached to the substrate. Thus, it may be preferential to bind stronger to the substrate. In this case, slow binding and unbinding dynamics and stronger attachment (described by the *slow* parameter set) may be a better choice to describe the behavior of single cells moving on a substrate due to their pili.

When several bacteria come close to each other, their pili can bind and the cells will form microcolonies. In the next chapter, we will study the dynamics of such colonies and the internal dynamics of cells within such colonies.

4

COALESCENCE AND INTERNAL DYNAMICS OF BACTERIAL MICROCOLONIES

When two microcolonies of *N. gonorrhoeae* are moving over a substrate and reach immediate vicinity, they can interact due to the binding of their pili. In this case, the pili will mediate an attractive force between the colonies that will lead to their coalescence: two smaller colonies merge and form a new, larger colony (see figure 4.1). This is a fundamental step during the formation of microcolonies [59]. Due to the fact that the merging of two microcolonies is accompanied by a rearrangement of cells within the colony, studying coalescence will also help us to learn about the internal dynamics of colonies.

One way to characterize the dynamics of the coalescence is to quantify the properties of the bridge (also called "neck") forming between the two colonies (see figure 4.1). In particular, the bridge height h is defined as the diameter of the bridge. For viscous liquid droplets it was shown by Frenkel [104] and Eshelby [105] that the initial closure of the bridge can be described by

$$h(t) = h_0 \sqrt{\frac{t}{t_h}}, \tag{4.1}$$

with the characteristic time

$$t_h = \frac{h_0 \eta}{2\chi}. \tag{4.2}$$

Here, η is the viscosity of the liquid droplet and χ its surface tension. While equation 4.1 is only valid for the initial closure of the bridge, a more general equation describing the full coalescence was given by Flenner et al. [106],

$$h(t) = 2^{\frac{2}{3}} h_0 \sqrt{\left[2 - \exp\left(-\frac{t}{2t_h}\right)\right]^{-\frac{2}{3}} \left[1 + \exp\left(-\frac{t}{2t_h}\right)\right]^{-\frac{4}{3}} \left[1 - \exp\left(-\frac{t}{t_h}\right)\right]}. \tag{4.3}$$

This equation corresponds to an relaxation of the area of the bridge. Here, we analyze the coalescence of *N. gonorrhoeae* microcolonies and estimate the time scales, characterizing the bridge closure. This allows us to check whether bacterial colonies exhibit properties similar to those of viscous liquid droplets.

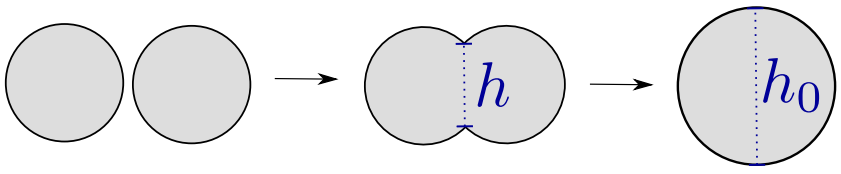

Figure 4.1: Definition of the bridge height.

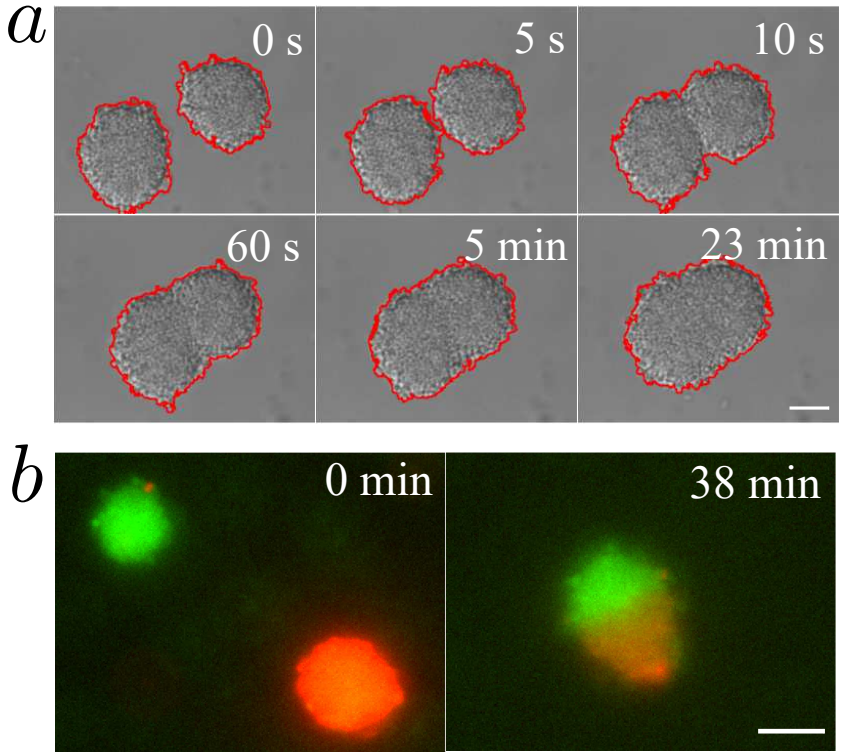

Figure 4.2: (a) Coalescence of colonies of *N. gonorrhoeae*. The red lines show the detect edges of the colonies. Bar = 10 μm. (b) Coalescence of differently labeled colonies of *N. gonorrhoeae*. The green colonies consists of cells labeled with YFP, the red colony consists of cells labeled with tdtomato. Bar = 10 μm.

In order to study the dynamics within a microcolony, we then apply our computational model (see chapter 2) and characterize quantities that are not accessible experimentally. We sampled over a wide range of parameters, in particular the detachment forces, detachment times and the attachment rate of pili. The simulation and their results were previously published in [60].

4.1 EXPERIMENTS ON MICROCOLONY COALESCENCE AND THEIR INTERNAL DYNAMICS

We studied the coalescence and internal dynamics of *Neisseria gonorrhoeae* microcolonies by performing experiments of colony coalescence and single cell tracking within microcolonies. Therefore, we applied the experimental protocols, depicted in appendix B and the algorithms described in appendix E to analyze the experimental images. The experimental coalescence data were contributed by the Nicolas Biais (Brooklyn College), the experiments studying the motility of cells within colonies were performed by the author of this thesis in the lab of Nicolas Biais. The analysis of the data was performed by the author.

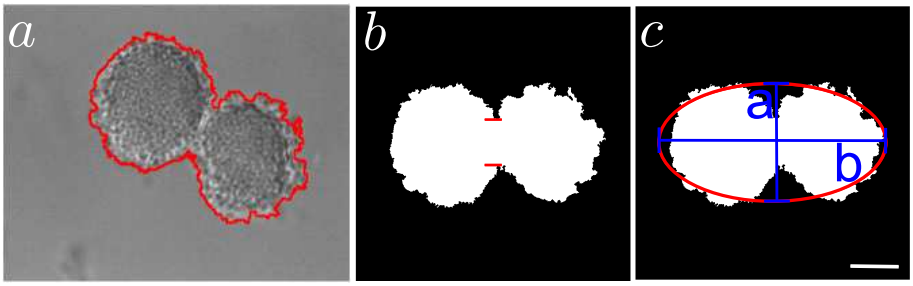

Figure 4.3: Quantification of the time scales involved in *N. gonorrhoeae* colony coalescence. (a) Detected edges of the midplane of two coalescing colonies as described in appendix E.1. (b) Image of the bridge detected in the binary image of two coalescing microcolonies. (c) image of the ellipse fitted to the binary image of two coalescing microcolonies and of its short and long axis a and b. Bar = 10 μm.

4.1.1 *Coalescence of* N. gonorrhoeae *microcolonies*

In order to study how bacterial colonies coalesce, the microcolonies first self-assembled and were then brought on top of a BSA coated coverglass. The coating was used to minimize the interactions of the pili with the substrate. Then, the colonies were brought close to each other, either by their own motion over the substrate, or by using an optical tweezer. We used a DIC microscope to image the midplane of two equally sized microcolonies performing a coalescence (see figure 4.2a).

From these experiments we made two important observations. Initially, the colonies approach each other rapidly until they collide. This process takes only a few minutes. Afterwards, the coalescence appears to be either slowed down or arrested and the colony exhibits the ellipsoidal shape.

Additionally, we mixed colonies made from two distinctly labeled cells. Specifically, colonies formed by cells labeled with YFP and td-tomato were brought together. Besides of the labeling of the cells, they exhibit the same behavior as wildtype cells. When two colonies consisting of the two cell populations came close to each other, they started to coalesce (see figure 4.2b). We observe that the cells of the colonies almost do not mix and exhibit a flat contact region.

To quantify these observations, we characterized the time scales of coalescence by measuring the time-dependence of two quantities: the height of the bridge forming between the two colonies and the ratio of the short and long axis of an ellipse fitted to the shape of the detected edge of the colonies. The way how we determined this quantities is depicted in appendix E and figure 4.3.

The time-dependence of the bridge height h of two coalescing microcolonies is shown in figure 4.4a. We fitted two different functions to describe the time-dependent behavior of the bridge height,

$$h(t) = 2^{\frac{2}{3}} h_0 \left[2 - \exp\left(-\frac{t+t_0}{2t_h}\right)\right]^{-\frac{1}{3}} \left[1 + \exp\left(-\frac{t+t_0}{2t_h}\right)\right]^{-\frac{2}{3}} \times \left[1 - \exp\left(-\frac{t+t_0}{t_h}\right)\right]^{\frac{1}{2}} \tag{4.4}$$

and

$$h_2(t) = h_0 \sqrt{1 - \alpha \exp\left(-\frac{t}{t_1}\right) - (1-\alpha)\exp\left(-\frac{t}{t_2}\right)}. \tag{4.5}$$

For both equations, the bridge height converges towards the diameter of a sphere having the combined volume of both initial aggregate large times t. Equation 4.4 is similar to the function determined by Flenner et al. (see equation 4.3). When two colonies attract each other due to bundling of their pili, they will approach each other until they collide and during this process start the closure of their bridge. In figure 4.2a one can see that after this initial collision the bridge is already closed considerably within 10 s. In order to reduce the effect of this initial collision, we introduced the offset time t_0 in equation 4.4. Equation 4.5 assumes that the closure of the bridge has two time scales, the initial approach of the colonies that takes time t_1 and the closure of the bridge, t_2. The equation corresponds to a exponential relaxation of the area. Here, the parameter α guarantees that the bridge converges towards h_0.

We fitted these two functions to the experimental data, as shown in figure 4.4a, and present the fitting parameters in table 4.1 for two different experiments.

We observe that the relaxation time t_h as predicted by Flenner et al. [106] for the closure of the bridge corresponds to the larger time scale t_2 of the double exponential function and is the order of $5-10$ minutes. The lower time scale t_1 is only in the order of a few seconds and corresponds to the initial collision of the colonies. Because of this collision, the offset time t_0 was introduced and is also in the order of a few minutes.

In order to estimate the time scale of the relaxation of the ellipsoidal colony, forming after the coalescence of the two colonies, towards the final spherical shape, we fitted an ellipse to the midplane of the colony and computed the axis ratio of the short axis a and the long axis b (see figure 4.3c). For the late coalescence, we assume that the ratio converges towards 1, following the equation

$$\gamma = \frac{a}{b} = 1 - \beta \exp\left(-\frac{t}{t_\gamma}\right). \tag{4.6}$$

The fitted parameters for the same experimental movies as for the bridge height are shown in table 4.1. The behavior of the axis ratio is shown for one experiment in figure 4.4b. The relaxation time t_γ is

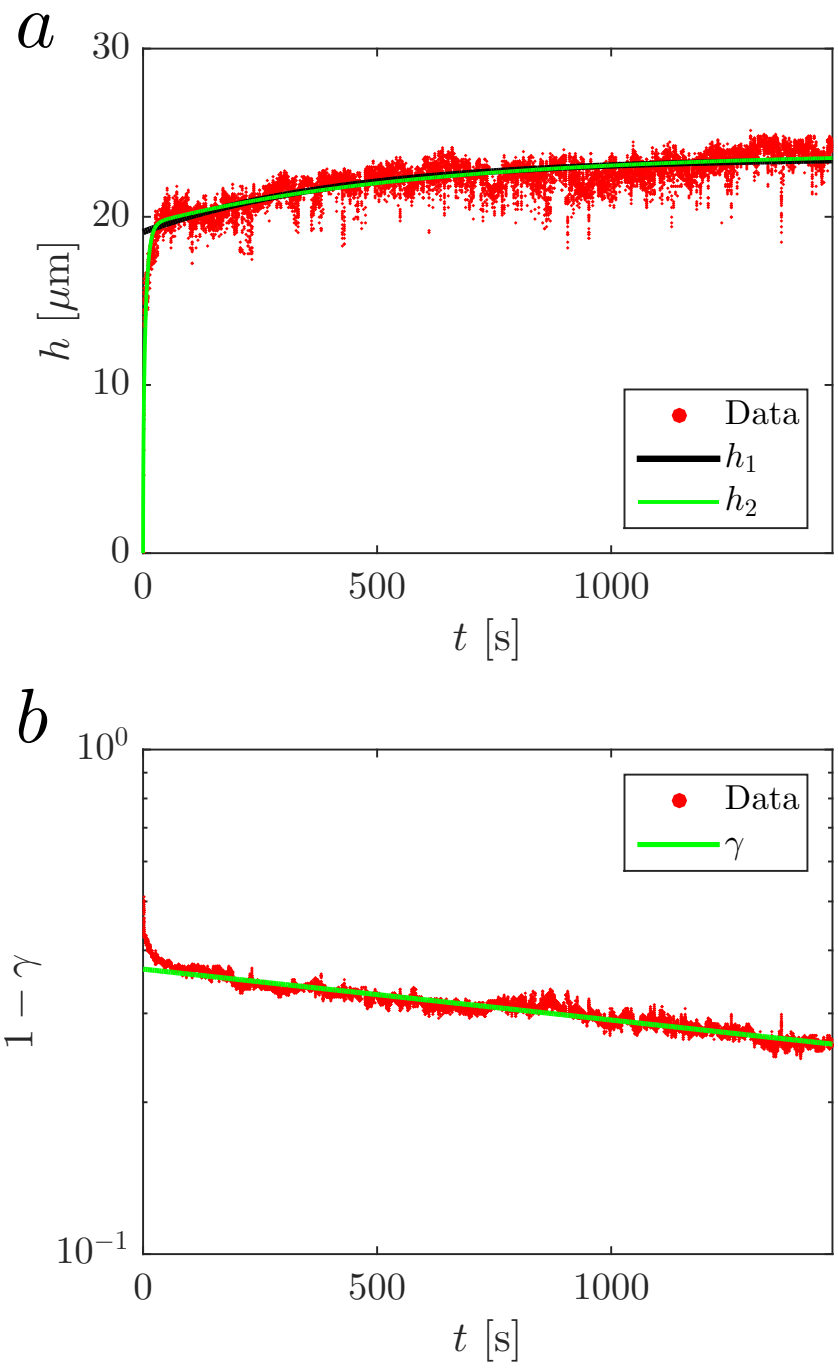

Figure 4.4: (a) Bridge height during the coalescence of *N. gonorrhoeae* microcolonies. Here, experimental data for the movie shown in figure 4.2 are presented and the fitting results for t_1 and t_2. (b) Axis ratio of the short and long axis of a ellipse fitted to the midplane of two coalescing colonies of *N. gonorrhoeae* microcolonies. Additionally, the time scale of the bridge closure is estimated by an exponential function (see green line and equation 4.6).

	EXPERIMENT 1	EXPERIMENT 2
h_0 [μm]	18.7 ± 0.1	19.1 ± 0.1
t_h [s]	230.3 ± 6.6	447.1 ± 6.4
t_0 [s]	468.4 ± 14.1	400.6 ± 8.2
h_0 [μm]	23.9 ± 0.1	24.2 ± 0.1
α	0.67 ± 0.01	0.41 ± 0.01
t_1 [s]	7.6 ± 0.2	3.5 ± 0.3
t_2 [s]	635.2 ± 19.3	925.4 ± 14.0
β	0.37 ± 0.02	0.43 ± 0.01
t_γ [s]	4304 ± 21	4597 ± 16

Table 4.1: Fitting results of the bridge closure and axis ratio relaxation parameters for *N. gonorrhoeae* microcolonies. The fitting functions are given in equation 4.4, 4.5 and 4.6.

larger than one hour and thus considerably larger than the bridge closure time t_h. The fact that a relaxation time can be defined suggests, that the colony will finally approach a spherical shape.

Up to now we did not discuss the role of cell divisions during the bridge closure and the shape relaxation of microcolonies. The division time t_{div} of *N. gonorrhoeae* has been shown to be in the order of 2-4 hours for conditions similar to those of our experiments [59, 107] and thus exceeds the characteristic time of coalescence. Additionally, when the change of volume of a sphere is given by the time t_{div}, the radius of the same colony follows $R \propto V^{1/3}$ and will grow with a characteristic time $3t_{div}$, thus being in the order of multiple hours. Such a time is larger than any other time characterizing the coalescence dynamics.

In order to understand the reason for the discrepancy between the time the colony needs to close its bridge (which is in the order of a few minutes) and the time the late ellipsoidal colony relaxes towards the spherical shape (which is in the order of hours) we need to study the internal dynamics of the microcolonies.

4.1.2 *Motility of cells within* N. gonorrhoeae *colonies*

To study the dynamics of individual bacteria within microcolonies, we were tracking those cells and analyzed their motility as a function of their position within the colony.

We mixed wildtype cells and a small fraction of fluorescently labeled cells (around 5-10 %). The cells were labeled with tdtomato and otherwise exhibit completely similar properties as the wildtype cells. Then, we allowed the cells to self-assemble into microcolonies and used a fluorescence microscope to track the cells within the midplane of the colonies (see appendix B). Next to the fluorescence channel which allowed us the tracking of the cells, we also recorded the co-

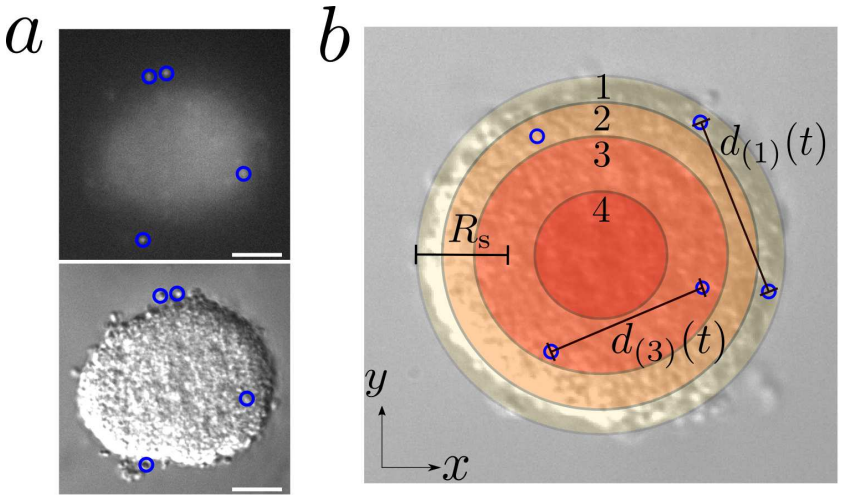

Figure 4.5: (a) Representation of the detection of fluorescently labeled cells. The upper image highlights the detection the fluorescently labeled cells. The lower image shows the position of individual cells relative to microcolony. Bar = 10 µm. (b) In order to be able to reduce the effect of rotations of the microcolonies on the trajectories of single cells, we computed the mean squared relative distance of cell pairs. Both cells were defined to be a pair if they could be found in a similar region, defined by their distance from the surface R_s.

lony on a DIC channel to detect the shape of the colony and to estimate the distance of the tracked cells from the colony surface (see figure 4.5a).

The colonies we were looking at interact, analogous to single cells, with the substrate due to their pili. Thus, they exhibit motion over the surface (see chapter 3). This affects the detected trajectories of the cells. Due to this process, it is not justified to just compute the mean squared displacement of the cells to quantify their motility (see section 1.2). Instead, we computed a quantity we call the mean squared relative distance δ_{MSRD}, the mean squared displacement of the scalar distance d of two cells. In appendix G we show that the time averaged mean squared distance of two particles exhibiting each a diffusive motion, each with diffusion coefficient D, and having an absolute distance d is given by

$$\delta_{MSRD}(\Delta t) = \langle [d(t+\Delta t) - d(t)]^2 \rangle_t = 4D\Delta t. \tag{4.7}$$

It is important to highlight that this quantity is not dependent on the initial distance of the two cells. The last step needed to estimate the diffusion coefficient of cells as a function of their distance R_s from the surface of the colony R_s is to group cells, depending on R_s. Therefore, we define four regions with increasing distances from the surface (see figure 4.5b) and only compute the diffusion coefficient of cells within the same region (see figure 4.6a). We observe that cells on the surface are highly motile, while cells within the bulk of the colony do not exhibit any detectable motility. The offset δ_0 in the mean squared relative distance, as seen in figure 4.6a, is originating from tracking errors [108] and corresponds to displacements in the order of one

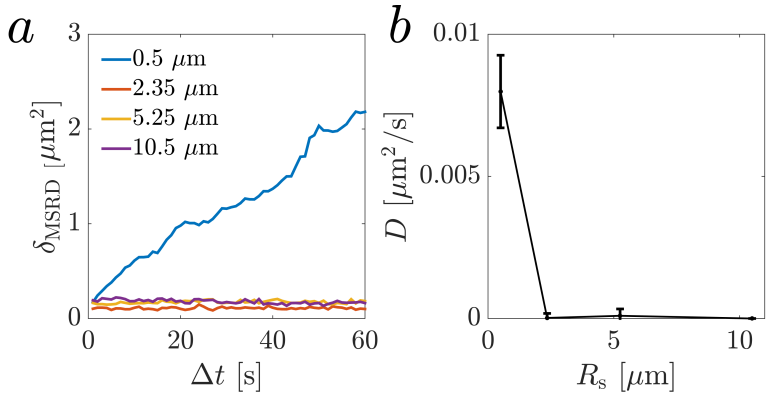

Figure 4.6: δ_{MSRD} as a function of time and diffusion coefficient D from the experimental data as a function of the distance R_s from the surface.

to two pixel (equivalent to $0.13 - 0.26$ µm). In order to compute the diffusion coefficients, we fit a function of the form

$$\delta_{MSRD}(\Delta t) = 4D\Delta t + \delta_0 \tag{4.8}$$

and observe a pronounced gradient of the diffusion coefficient as a function of the distance from the surface of the colony (see fig. 4.6). Cells at the surface of the colony exhibit a considerable motility, while cells within the bulk, specifically being more than one cell size (around 1 µm) away from the colony surface, do not show any measurable motility.

Thus, our main experimental observation are the gradient of motility within a colony and the appearance of multiple time scales during the coalescence of colonies. Now we want to find some rational explanation of these effects and choose our computational model as ideal tool for investigating these processes.

4.2 MODELING MICROCOLONY COALESCENCE AND INTERNAL DYNAMICS

We first show that our model (see chapter 2) is able to reproduce the behavior observed in experiments and summarized in the previous section and check how it depends on the chosen parameters of the simulation. Afterwards, we study the motility of cells within the colonies and look for correlating gradients of multiple quantities related to the properties of the pili network, the structure of the colony or the involved force fluctuations.

For our simulations, we sampled over a wide range of parameters to study the coalescence and the internal dynamics of microcolonies (see table F.3 and F.4). Particularly, we studied the role of the pili-pili-detachment time $t_{d,pp}$, the detachment force $F_{d,pp}$ and the attachment rate $\gamma_{att,pp}$. Here, we will only present the dynamics of colonies for two parameter sets (see table 4.2). The sets are named after the ratio of their detachment forces $F_{d,pp}$ and the stalling force $F_{stall} = 180$ pN. For the parameter set called *weak*, the stalling force is larger than the

	STRONG	WEAK
$F_{d,pp}$ [pN]	360	120
$t_{d,pp}$ [pN]	50	50
$\gamma_{att,pp}$ [Hz]	0.5	0.5

Table 4.2: Definition of *weak* and *strong* pili-pili-interactions parameter sets.

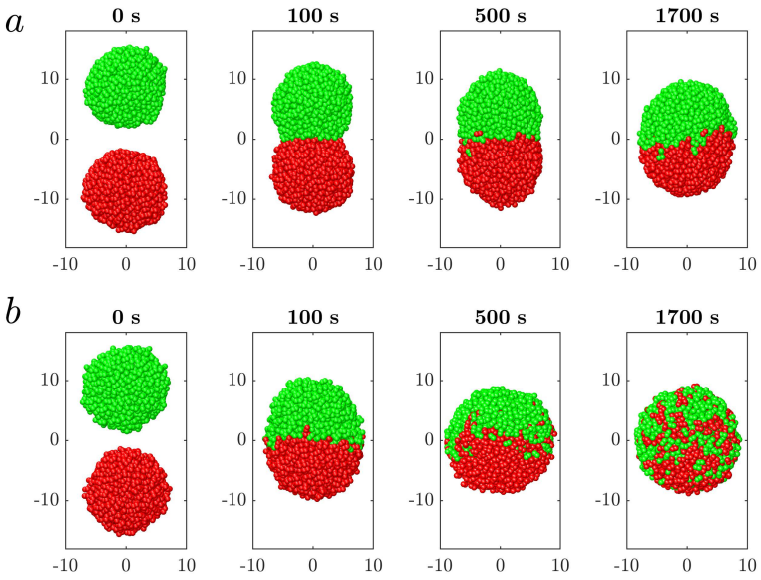

Figure 4.7: Coalescence of *in silico* microcolonies for the (a)*strong* and (b) *weak* parameter set. The two initial colonies consist of 1000 cells each.

detachment force, and the pili are expected to unbind more easily. For the parameter set called *strong*, the pili-pili-bonds are stronger.

All other parameters used in our simulations, are given in table 2.1.

4.2.1 *Coalescence of* in silico *colonies*

We first apply the computational model (see chapter 2) to study the coalescence of two, equally sized, colonies that consist of up to 1500 cells each (see figure 4.7). In these simulations, we ignore the interactions with a substrate. The reason for this simplification is the fact that in the experiment we use a substrate with reduced interactions. Additionally, in experiments we observe that colonies have spherical shapes and are wetting the substrate only weakly. Thus, the pili-mediated interactions between cells are considerably stronger than those with the substrate, allowing us this simplification. More information how the simulations were initialized and analyzed are given in appendix F.2.

For the *strong* parameter set, we observe properties similar to those observed experimentally. After coalescence, the two colonies only weakly mix and they exhibit a sharp interface between the initial colo-

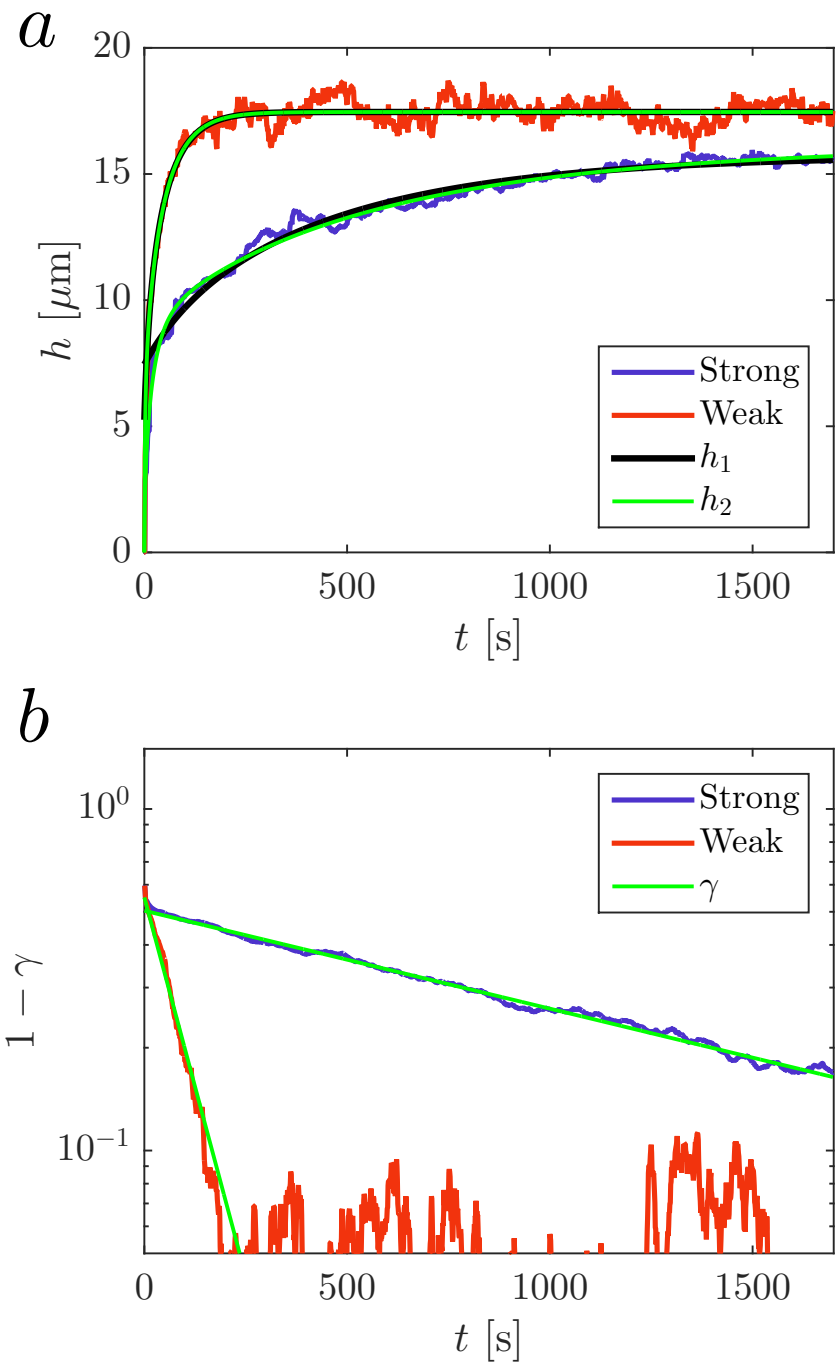

Figure 4.8: (a) Bridge height during the coalescence of *in silico* microcolonies for the *weak* (red) and the *strong* (blue) parameter set. Here, data for the movie shown in figure 4.7 are presented and the fitting results for t_1 and t_2. (b) Axis ratio of the short and long axis of a ellipse fitted to the midplane of two coalescing colonies of *N. gonorrhoeae* microcolonies. The time scale of the bride closure is estimated by an exponential function (see green line and equation 4.6).

	STRONG	WEAK
h_0 [μm]	12.5 ± 0.1	13.9 ± 0.1
t_h [s]	241.5 ± 5.5	28.4 ± 1.2
t_0 [s]	103.8 ± 5.2	4.4 ± 1.4
h_0 [μm]	16.1 ± 0.1	17.5 ± 0.1
α	0.30 ± 0.01	0.13 ± 0.03
t_1 [s]	28 ± 3	3.6 ± 6.4
t_2 [s]	655.7 ± 5.2	57.2 ± 3.0
β	0.50 ± 0.01	0.55 ± 0.03
t_γ [s]	1514 ± 88	98.0 ± 8

Table 4.3: Fitting results of the bridge closure and axis ratio relaxation parameters for *in silico* microcolonies. The fitting functions are given in equation 4.4, 4.5 and 4.6.

nies (see figure 4.7a). To study the dynamics of the bridge closure, we fitted, similarly to our analysis of the experiment, the two functions given in equation 4.4 and equation 4.5 to the bridge height (see figure 4.8a) and we observe a fast initial time scale t_1, corresponding to the initial approach of the colonies and a slower time scale, t_2 or t_h, that are the same for both functions and corresponds to the closure of the bridge (see table 4.3). For the *strong* parameter set they are, similar to the experimental results, in the order of minutes. To characterize the late coalescence towards the spherical shape, we again assume that the axis ratio of an ellipse, fitted to the midplane of the ellipsoidal colony (similar to figure 4.3), is relaxing exponentially towards 1, with the characteristic time t_γ (see equation 4.6). For the *strong* parameter set we observe the same discrepancy of the time scales as the one observed experimentally (see figure 4.8b), the bridge closure time is roughly three times smaller than the relaxation time towards the spherical shape (see table 4.3).

For the *weak* parameter set we observe that the coalescence takes place much faster (see figure 4.7b) than the coalescence of the *strong* parameter set. The two colonies do mix and do not exhibit a clear interface, as observed experimentally. For the bridge closure, we also observe two time scales t_1, corresponding to the initial approach, and a second time scale corresponding to the closure, t_2 or t_h (see figure 4.8a). The times are in the order of one minute, making them considerably smaller than those of the experiment or the simulations with *strong* pili-pili-interactions.

4.2.2 *Internal dynamics of* in silico *colonies*

With the help of our computational model, we can study the motility of individual cells within microcolonies and different quantities that may affect the behavior of the cells. Analogously to the simu-

lations of microcolony coalescence (see subsection 4.2.1), we ignore interactions with a substrate. Again, we only present the results for two different parameter sets characterizing the pili-pili-interactions, *weak* and *strong*, as defined in table 4.2.

We started with computing the time-averaged mean-squared displacement (MSD)

$$\delta_{MSD}(\Delta t) = \langle [\mathbf{r}(t+\Delta t) - \mathbf{r}(t)]^2 \rangle_t = 6D\Delta t, \tag{4.9}$$

of individual cells, where $\mathbf{r}$ is the position of the cell in three dimensions and D is its diffusion coefficient. Additionally, we measured the mean-squared relative distance (MSRD, see equation 4.7 and appendix G) of cell pairs. The time-dependence of both quantities was studied as a function of the cell distance from the surface of a microcolony. Therefore, cells were grouped in multiple regions, that differ in their distance from the surface of the *in silico* microcolony (see appendix F.3 for more details). The MSD exhibits a linear time-dependent behavior, corresponding to diffusive motion (see figure 4.9a and figure 4.9b). Additionally, the MSD shows a higher motility of cells close to the surface of the colony, compared to cells within the colony bulk for both parameter sets (see figure 4.9a-d).

By computing the MSD and the MSRD it is possible to estimate the diffusion coefficient D of the cells as a function of their distance from the colony surface. In both cases, we observe similar results, as can be seen in figure 4.9e and figure 4.9f.

One can define the characteristic length scale l_D of the gradient of the diffusion coefficient D, by fitting a function of the type

$$D = D_0 + D_r \exp\left(\frac{l}{l_D}\right), \tag{4.10}$$

where D_0 is the offset of the diffusion coefficient, D_r is the magnitude of the gradient and l_D is the characteristic length scale of the gradient of motility. The fitting of this function is visualized in figure 4.9e and figure 4.9f. The resulting values of D_0, D_r and l_D are given in table 4.4.

For the *weak* parameter set the diffusion offset D_0 and the magnitude of the gradient D_r are larger than for the *strong* parameter set, corresponding to a stronger motility of the cells within and on the surface of the colony. It appears that the characteristic length scale l_D is independent of the chosen parameter set and in the order of the size of an individual cell.

In order to study the origins of the gradient of the diffusion coefficient, we studied multiple quantities connected to the dynamics of the pili. For the number of attached and actively pulling pili of a cell, we observe a slight decrease close to the surface of the colony, as shown in figure 4.10a. Additionally, the mean number of pulling pili is lower for weaker pili-pili-interactions. For the total number of pili a cell possesses, we do not observe any spatially dependent gradient within the colony. Instead, the cells possess roughly 15 pili, corresponding to the maximal number N_{max} (see section 2.1 and table 2.1). This is a result of the average life time of the pili (see figure 4.10b), which

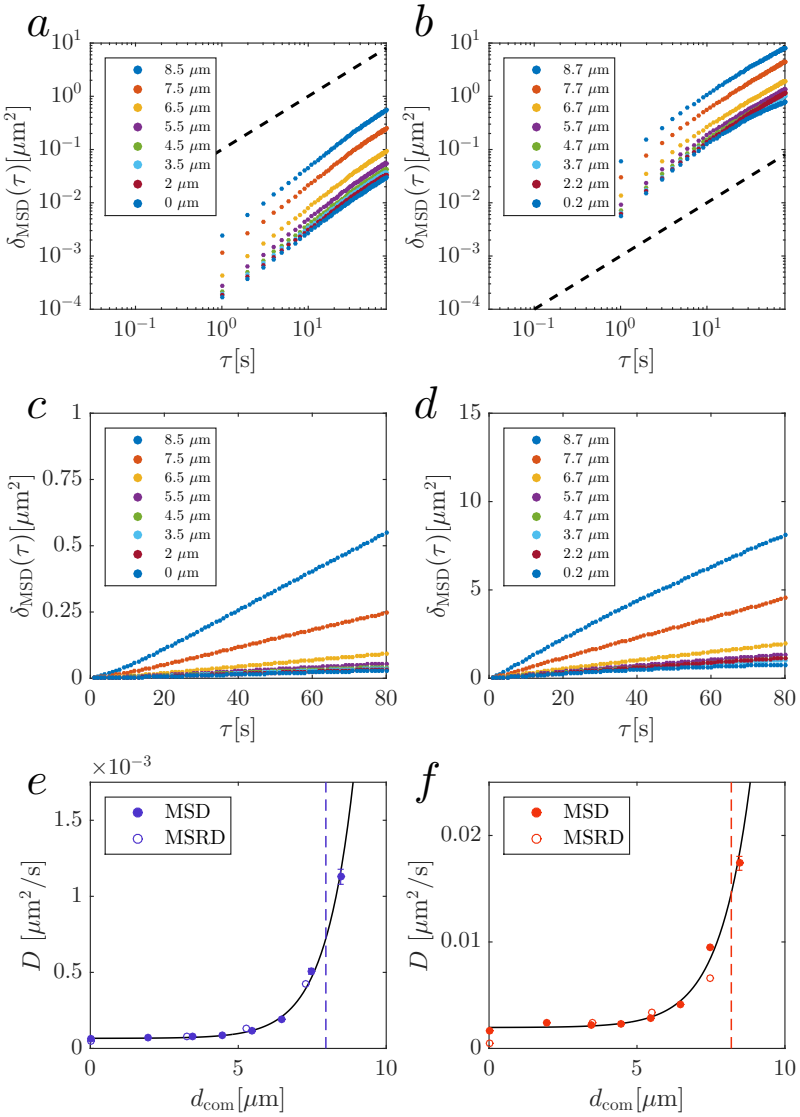

Figure 4.9: Motility of cells within *in silico* microcolonies for the *strong* parameter set (a,c,e) and the *weak* parameter set (b,d,f). (a,b) Double-logarithmic representation of the time-dependent mean-squared displacement for cells with different distances from the center of the colony. The MSD exhibits a linear, diffusive, behavior. The black line gives the slope of a linear function. (c,d) MSD for both parameter sets, but with linear axes instead of double-logarithmic ones. (e,f) Diffusion coefficient D of the cells as a function of their distance from the center of the colony. D was computed by measuring the MSD (filled circles) and by measuring the MSRD (hollow circles). The gradient can be characterized by equation 4.10, as shown by the black line, with the characteristic length scale l_D. The vertical lines s show the average colony size R_{col}, estimated by the cell number density (equation 4.11).

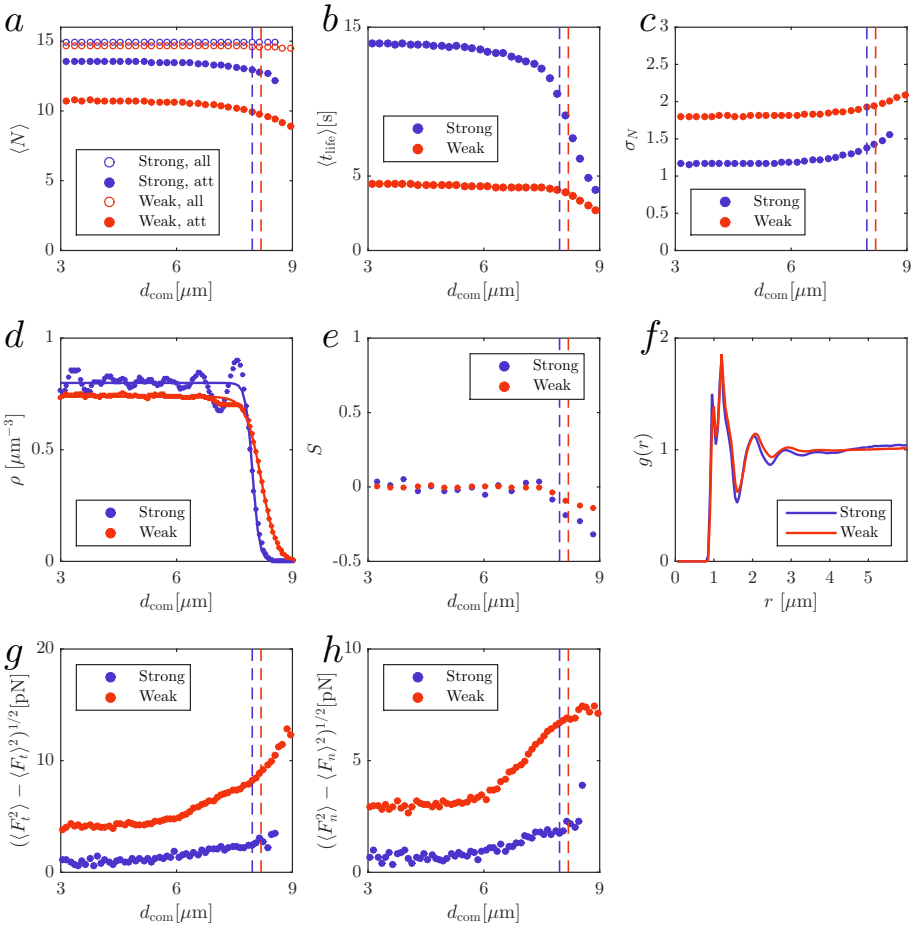

Figure 4.10: Internal dynamics of *in silico* microcolonies. Here, the red data highlights the *weak* parameter set and the blue data the *strong* parameter set. The vertical lines that can be seen in most plots show the average colony size R_{col}, estimated by the cell number density (equation 4.11). (a) Mean of the number of all pili (hollow circles), and of the pili which generate a pulling force on cells as a function of d_{com}. (b) Mean life time of the pili of cells within a microcolony. (c) Variance of the number of actively pulling pili as a function of the distance of the cells from the colony center d_{com}. (d) Cell number density of cells within a colony. The lines highlight a fit with the function 4.11. (e) Nematic order parameter S (see equation 4.12) of the cell main axis relative to the vector pointing from the center of the colony to the center of the cell as a function of the distance from the center of the colony d_{com}. (f) Pair correlation function $g(r)$ of bulk cells as a function of the distance r between the cells. The graph agrees for both parameter sets. (g,h) Variance of the absolute values of the tangential force F_t and the normal net force F_n acting on a cell relative to the surface of the colony.

	STRONG	WEAK
D_0 [$\mu m^2/s$]	$(6.64 \pm 0.95) \times 10^{-5}$	$(1.97 \pm 0.46) \times 10^{-3}$
D_r [$\mu m^2/s$]	$(1.97 \pm 2.31) \times 10^{-7}$	$(5.7 \pm 15.3) \times 10^{-6}$
l_D [μm]	0.98 ± 0.19	1.07 ± 0.38
ρ_0[μm^{-3}]	0.80 ± 0.03	0.74 ± 0.03
R_{col} [μm]	7.97 ± 0.02	8.19 ± 0.02
ω [μm]	0.18 ± 0.03	0.40 ± 0.02

Table 4.4: Parameters characterizing the internal dynamics of *in silico* microcolonies.

is for both parameter sets much larger than the time corresponding to the pili production rate of 15 Hz (see table 2.1). Not surprisingly, for the *weak* pili-pili-interactions, the average life time is smaller than the life times for the *strong* interactions. We observe a pronounced gradient of life times. Pili on the surface possess a considerably smaller life time, compared to pili within the bulk of the colony.

Next to the spatially dependent number of pili and their life time, we can also measure the fluctuations of the number of actively pulling pili that a cell has as a function of the position of the cell within the colony. We observe a weak increase of the standard deviation of the pili number near the surface for the *weak* and the *strong* parameter set (see figure 4.10c).

Besides the dynamics of the pili network, we were also studying the structure of the colony and the arrangement of the cells. An important measure to characterize the structure is the density ρ of cells (see figure 4.10d). We can compare its profile to the density profile of liquid–liquid or liquid–vapor interfaces [109–111], which has the form

$$\rho(d_{com}) = \frac{\rho_0}{2}\left(1 - \tanh\left[\frac{d_{com} - R_{col}}{\omega}\right]\right), \tag{4.11}$$

with d_{com} being the distance from the center of the colony, ω the width of the density profile and ρ_0 the density within the colony bulk. For the *strong* parameter set, the colony possesses a slightly smaller radius and a slightly higher density (see table 4.4), compared to *weak* pili-pili-interactions for the same number of cells in the colony. Additionally, stronger interactions reduce the width of the interface. The higher density may reduce the motility of cells in the colony and thus contribute to the observed gradient of motility by reducing the available volume for motion and by introducing jamming effects.

For the *strong* interactions, we observe a pronounced peak of the cell density near the surface of the microcolonies which originates from the nematic order of the diplococcus-shaped cells close to the colony surface (see figure 4.10e). The nematic order parameter was determined by computing the angle α between the axis connecting the two cocci of a cell and the vector pointing from the center of the

colony to the center of the cell. Then, the nematic order parameter S [112] is defined to be

$$S = \left\langle \frac{3\cos^2\alpha - 1}{2} \right\rangle . \tag{4.12}$$

Within the microcolonies, the cells possess an overall random distribution of their directions, which corresponds to a nematic order parameter S close to 0. At the surface of the colonies, we observe a bias towards a tangential orientation of cells with $S < 0$ and that may cause the peak of the spatially dependent cell density ρ.

In order to learn more about the arrangement of cells within the colonies, we were computing the pair-correlation function $g(r)$ [113] of the bulk cells (see appendix F.3 for more information). We observe an almost identical shape of the pair correlation function for the two parameter sets with correlations only reaching up to 3–4 µm, corresponding roughly to distance to the centers of the next neighbors and pointing towards more fluid-like properties of colonies [110].

The pili forces are directly translated into the motion of cells. Here, we computed the absolute values of the normal and tangential components of the sum of the pili-mediated and the excluded volume forces, relative to the vector pointing from the center of the colony to the center of the cell. Then, we computed the square root of the variance (see figure 4.10g and figure 4.10h). In both cases and for both parameter sets we observe an increase of the force fluctuations near the surface of the colonies, which is translated into the higher motility of the cells. Additionally, for *strong* pili-pili-interactions the force fluctuations are smaller than for *weak* interactions. This is a consequence of the shorter pili life times and the resulting more frequent rearrangement of the pili network.

4.3 DIFFERENCES BETWEEN EXPERIMENT AND SIMULATION

We need to discuss a discrepancy between our simulations and the experimental results. While the simulations for the *strong* parameter set exhibit qualitative similarities for the coalescence dynamics to the experimental data, the observed gradient of motility predicts values for the diffusion coefficient which are one order of magnitude lower than those observed experimentally (see figure 4.6 and 4.9). However, the gradient of the diffusion coefficients exhibits similar properties for the *weak* parameter set. For this parameter set the complete coalescence dynamics have time scales of a few minutes or less, which are considerably smaller to those observed in the experiment (see figure 4.4 and figure 4.8). We suggest that this behavior originates from the fact that the pili network within a colony is more complex than described by our computational model. While pili within a bacterial colony form dense networks where multiple pili can interact with each other, in our simulation we consider binary interactions only. While the pili of cells on the surface form less bonds to other pili and are thus less efficiently embedded into the pili network within our

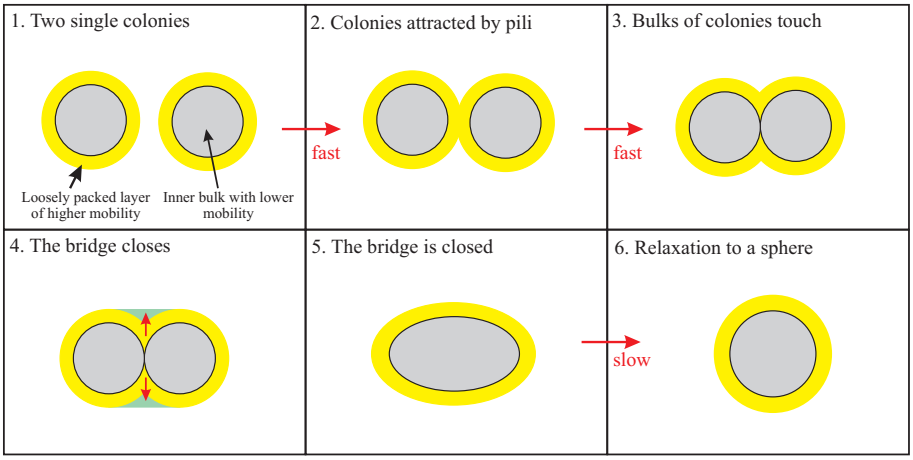

Figure 4.11: Sketch of the layer-bulk model and how it affects the coalescence of microcolonies. The cells within the bulk region of the colony (gray) possess a weak motility only, cells at the outer layer of the colony (yellow) are weakly packed and highly motile. The shown image represents an idealization of two distinct regions. In our experiments and simulations, the motility is characterized by a gradient (see subsections 4.1.2 and 4.2.2).

simulation, cells within the bulk of the colony are tightly embedded into the network and exhibit a considerably weaker motility.

After showing that our computational model can reproduce our experiments qualitatively and allows us to learn more about the properties of the pili network and the involved forces within a microcolony, we will now discuss the connection between the observed gradient of motility and the peculiar behavior of the colony coalescence.

4.4 THE LAYER-BULK MODEL AND ITS ORIGIN

During the coalescence of microcolonies, the colonies initially approach each other within seconds, followed by the closure of the bridge (with a time scale in the order minutes) and finally followed by the relaxation from an ellipsoidal towards a spherical shape with a time scale on the order of one hour or more.

We suggest that these dynamics are mediated by the gradient of motility, where a colony possesses an outer layer of highly motile cells and an inner bulk consisting of cells that exhibit a weak motility only.

How such a gradient can mediate the observed dynamics of colony coalescence is visualized in figure 4.11. Initially, both colonies attract each other due to pili-pili-interactions and will collide within seconds. This approach continues until the outer layer regions intersect and the bulk regions of both colonies touch. Then, the two colonies are no longer able to continue the fast approach. Cells at the outer layer move towards the intermediate region of the dumb-bell shaped colony and close the bridge, so that the bridge closes and the colonies reaches a more ellipsoidal shape. The time scale of this process is in the order of minutes. This appears reasonable, because our measurements

of the MSRD and the MSD show that cells of the outer layer move over distances in the order of 1 μm within 1-2 minutes. In order to close the bridge of a colony having a diameter of 20 μm, they need to move a comparable distance. Finally, the resulting ellipsoidal colony relaxes towards a spherical shape. This process is no longer governed by the dynamics of the outer layer, but by the properties of the bulk. Due to the weak motility of the cells within the bulk, which possess a diffusion coefficient that is at least one order of magnitude smaller than those for the surface cells, the characteristic time scale for this process is in the order of one hour for colonies having a diameter of roughly 20 μm. In the next chapter we show how the size of the colonies affects the discussed time scales.

In order to study the origin of the gradient of motility within a colony, responsible for the coalescence dynamics, we studied multiple quantities from our computational model that are, to the present day, not accessible experimentally (see figure 4.10). While these quantities allow us to learn more about the origin of the gradient of motility, it remains to be unraveled what the general properties of the bulk regions are, more specifically if the bulk exhibits more fluid-like or more solid-like properties. From the measurement of the MSD and the MSRD we found that for large times of $\Delta t = 100$ s cells exhibit a diffusive motion. For the pair-correlation function of cells within *in silico* microcolonies we observe only correlations for direct neighbors, pointing towards fluid-like behavior. By calculating the nematic order parameter of the cells, we observe a lack of order of the cells which does also points towards a fluid-like behavior of the bulks. Another observation which points towards more fluid-like properties is the fact that we can define a time scale of the relaxation of ellipsoidal colonies towards a spherical shape, which is reminiscent of the coalescence of liquid droplets and their relaxation towards a spherical drop. We do not observe an arrest of the coalescence. Thus, we suggest that a bacterial microcolony exhibits fluid-like properties with a gradient of motility of the individual cells within the colony.

To estimate whether a chemical gradient of nutrients, oxygen or waste metabolic products is involved the formation of the gradient of motility, we estimate the effective diffusion coefficient of these molecules within a colony. Therefore, we assume that a microcolony has properties of a porous medium. From the dependence of the colony radius from the number of cells (see appendix F.3.2) and the volume of the single cells we could estimate the volume fraction $\phi = 0.65 - 0.7$. The effective diffusion coefficient D_{eff} of a solute in a porous medium with such a volume fraction is estimated by

$$D_{eff} = D_{aq} \frac{1-\phi}{1-\frac{1}{2}\ln(1-\phi)}, \tag{4.13}$$

as shown in [114]. Here, D_{aq} is the diffusion coefficient of the solute in water. For bacterial microcolonies we then find

$$D_{eff} = 0.18 - 0.23\ D_{aq}. \tag{4.14}$$

The diffusion coefficient of a wide range of different solutes associated with biofilms, for example oxygen, glucose or urea, were found to follow $D_{aq} \geqslant 100\ \mu m^2/s$ [115]. Thus, the lower limit of the effective diffusion coefficient within a microcolony is given by $D_{eff} \geqslant 18\ \mu m^2/s$. From the mean squared displacement

$$\Delta r^2 = 6 D_{eff} \Delta t \tag{4.15}$$

we find for the length corresponding to the characteristic colony size $\Delta r = 15\ \mu m$ the time $\Delta t = 2.1$ s. Within only a few seconds nutrients, oxygen or waste metabolic products are able to diffuse out of or into the colony. Thus, we exclude chemical gradients as origin of the observed gradient of motility.

4.5 COLONY SIZE DEPENDENT COALESCENCE

We can use the computational model (see chapter 2) to predict how the size of the coalescing colonies affect the involved time scales. Here, we only investigate the *strong* parameter set and study cases in which the initial colonies were consisting of 50 to 1500 cells each.

By computing the bridge height and the axis ratio of the ellipse fitted to the midplane of the colonies we were able to estimate the involved time scales.

By plotting the time scales t_γ as a function of the number of cells within the colony N, we found that $t_\gamma \propto N^{2/3}$ (see figure 4.12a and figure 4.12b). The radius R of the colony scales with the colony volume $N \propto R^3$, so that $t_\gamma \propto R^2$, the relaxation time is proportional to the surface of the colonies. We can use this scaling to study the behavior of the bridge closure for colonies of varying size (see figure 4.12c). By estimating the final size of the colonies after relaxation h_∞ (see appendix F.3.2), we could rescale the final height of the colony. Additionally, we were rescaling the time of the closure of the bridge with the relaxation time t_γ. By rescaling these two quantities, we observe a collapse of the time-dependent bridge height on a single master curve. Thus, the bridge closure time t_h is proportional to the surface of the colonies,

$$t_h \propto R^2. \tag{4.16}$$

For liquid droplets the time scale of bridge closure scales with the colony radius [104, 116] ,

$$t_h \propto R. \tag{4.17}$$

Such a relation was also found to explain the fusion of cellular aggregates [106, 117, 118]. For bacteria, it appears that such models of viscous liquid droplet coalescence are not able to explain the coalescence of *N. gonorrhoeae* microcolonies.

We suggest that this behavior originates from the gradient of motility within the microcolonies. Additionally, the colonies may possess viscoelastic properties. In this case, the scaling of droplets of different

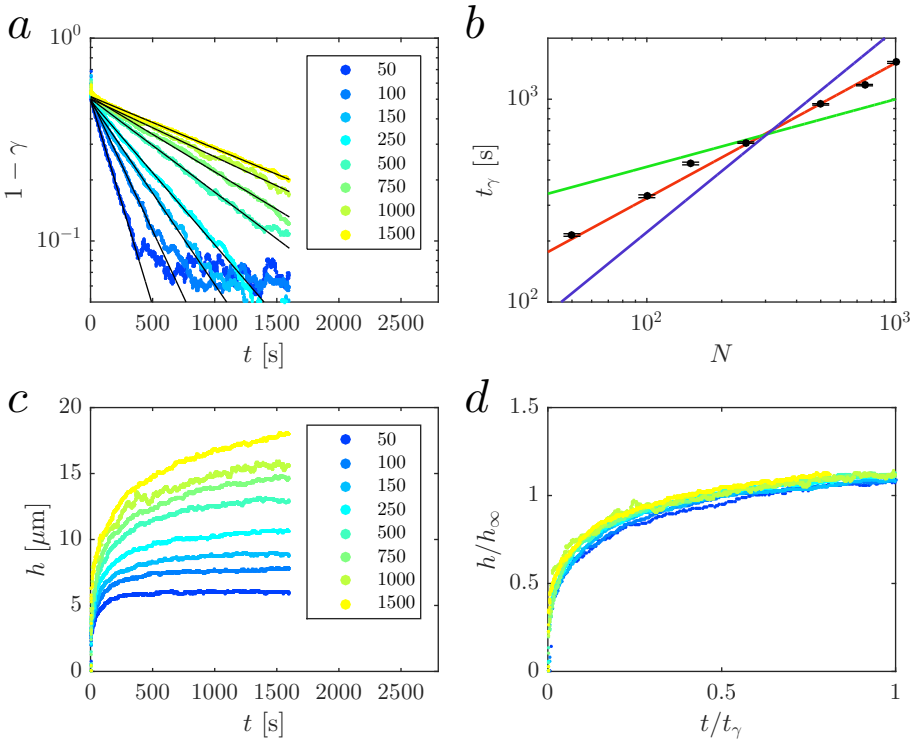

Figure 4.12: [Colony-size dependent coalescence of *in silico* microcolonies. (a) Ratio of short and long axis γ for colonies consisting of different numbers of cells as a function of time. Here, we assume that $1-\gamma$ can be described by equation 4.6, which allows us to compute the relaxation time t_γ. (b) Colony shape relaxation time t_γ as a function of the number of cells in the colony. It follows $t_\gamma \propto N^{2/3}$ (red line). The green line corresponds to $t_\gamma \propto R$, the blue line to $t_\gamma \propto R^3$. (c) Bridge height as a function of time for different cell numbers of the initial two of colonies. (d) Rescaling of the bridge height with the final colony radius, h_∞ (see figure F.2a), and of the time with the relaxation time $t_\gamma \propto R^2$. In this case, the curves collapse.

sizes can differ from the previous predictions [119–121] and show a more complex behavior, that for example depend on the material properties.

4.6 SUMMARY

In this chapter we studied the dynamics of pili-mediated microcolony fusion and how the internal dynamics of the colonies can affect the coalescence. Our experiments and simulations suggest that, while the colonies exhibit fluid-like behavior locally, the resulting aggregates exhibit a more complex behavior. Particularly, we observe a gradient of motility where cells near the colony surface are more motile than cells in the bulk. Additionally, the size-dependent scaling of the colonies cannot be explained by simple models of liquid droplet coalescence.

In order to study the internal properties more detailed in the future and to find clear evidence whether bacterial colonies exhibit fluid-like behavior, it is necessary to study its rheological properties with the help of experiments and simulations [122, 123] . Such experiments will help to study the role of the viscoelastic properties of the cells and colonies and the adaptation of colonies and their internal dynamics towards different mechanical cues.

After studying the dynamics of colonies consisting of only one population of cells with similar properties, in the following chapter we will study the behavior of colonies of different cell populations with altered properties of their pili dynamics.

5

DEMIXING OF BACTERIAL MICROCOLONIES

In the previous chapter, we studied the motion of individual cells within bacterial aggregates and how they drive the coalescence of microcolonies. Pili-mediated forces play a fundamental role in the dynamics of microcolonies.

Here, we will study how the dynamics of colonies are altered after manipulating the pili-mediated forces. In experiments we see that within minutes microcolonies, consisting of not just one type of cells but of cells with pili having different properties, are capable of mixing or demixing. We will present and discuss previously published and new experiments and compare the outcome of these experiments to our computational model. The resulting behavior exhibits qualitative similarities to the differential adhesion hypothesis.

Our results concerning mixtures of ΔpilT (cells that are not capable to retract their pili) and wildtype cells were previously published [60, 124].

5.1 DEMIXING OF WILDTYPE AND MUTANT BACTERIA

Oldewurtel et al. [57] have extensively investigated the cell sorting of mixtures of wildtype cells and different mutants (see figure 5.1). In their experiments, two cell populations were labeled fluorescently. They started with individual cells of the two populations on top of a glass surface and analyzed the structure of the microcolonies after 3-5 hours of assembly. We will start with discussing mixtures of cells that, besides of their fluorescent labeling, have the same properties as wildtype cells of *Neisseria gonorrhoeae*. Here, we refer to those cells as "wildtype cells". For such mixtures, uniform mixing of the cell populations within the colony was observed (see figure 5.1a) [57, 124]. For a mixture of wildtype cells and mutant cells that do not possess pili, called ΔpilE, the wildtype cells form microcolonies. The mutant cells are not able to move on the substrate or to interact with each other, thus they are not incorporated within any microcolonies (see figure 5.1b). Additionally, it was possible to study the mixture of wildtype cells and hyperpiliated cells, having a higher mean number of pili. The hyperpiliation was realized by using strains with three copies of the *pilE* gene. In this case, the cells with the lower number of pili formed the outer shell of the microcolonies, the mutant cells were found within the bulk. By post-translational modification of the major subunit of the pili, Oldewurtel et al. were able to create mutants with altered pili-pili detachment forces. They were able to show that for those mutants, the detachment forces of wildtype-wildtype and mutant-mutant pili bonds were considerably higher than those of wildtype-mutant bonds. In this case, the wildtype and mutant cells each form colonies on their own. While these colonies can also in-

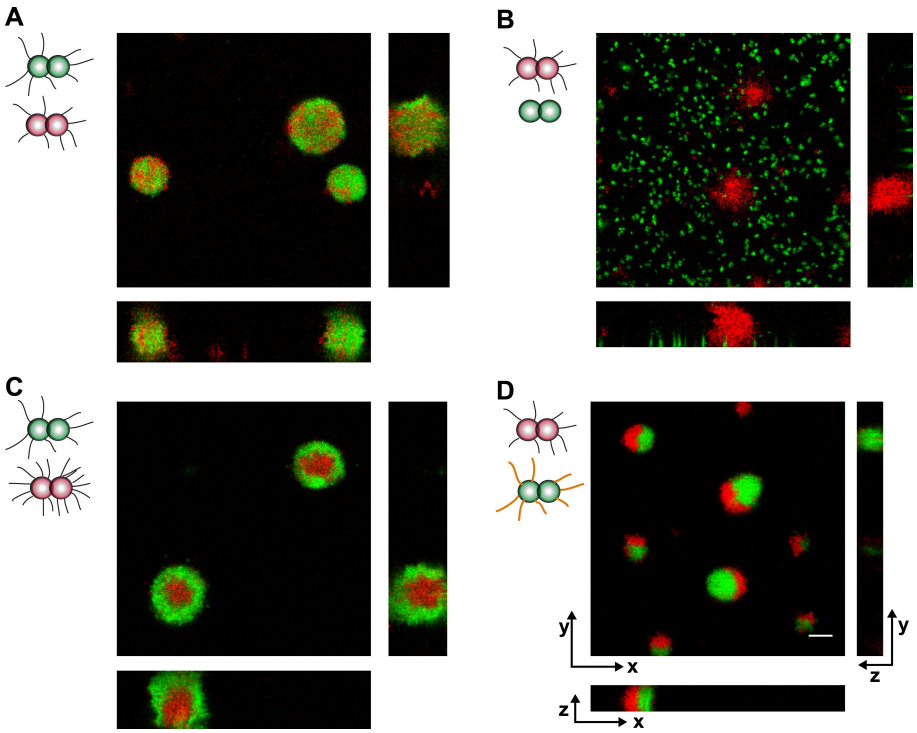

Figure 5.1: Confocal microscopy images of mixing and demixing of different types of *Neisseria gonorrhoeae* cells. The figure was taken from [57]. (a) Mixture of two differently labeled populations of wildtype cells. (b) Mixture of wildtype cells (red) and mutant cells without any pili (green). (c) Mix of wildtype cells (green) and hyperpiliated cells (red), possessing a higher mean number of pili. (d) Mixture of wildtype cells (red) and cells with altered pili-pili interactions (green). The individual cell populations form distinct colonies that are also able to interact with each other.

teract with each other and form larger colonies, from figure 5.1d it becomes clear that the cells prefer to be close to cells of the same kind.

Next to reporting about the the work of Oldewurtel et al. [57], we also studied the mixture of wildtype cells of *Neisseria gonorrhoeae* and mutant cells with ΔpilT mutants after three hours of assembly. The presented experimental data was contributed by Prof. Nicolas Biais (Brooklyn College, New York, USA). While the ΔpilT mutant cells are able to create pili which are able to protrude from the cell membrane and bind to other pili, they are no longer able to retract and the cells are not able to actively create forces on their own. For these cells, we do not observe motion on a substrate. For the mixture of wildtype cells and the ΔpilT mutants we observe that the mutant cells are concentrated at the outer shell of the colonies, while the wildtype cells are found within the bulk of the colonies (see figure 5.2b). In order to quantify this behavior, we measured the intensity profile of the two fluorescently labeled cell populations, giving us quantitative evidence of demixing (see figure 5.2d). In a agreement with the experiments of Oldewurtel et al. [57], we observed uniform mixing of two differently labeled populations of wildtype cells (see figure 5.2a and 5.2c). Details of the labeling of these cells are given in appendix B.

5.2 APPLICATION OF THE COMPUTATIONAL MODEL TO STUDY COLONY DEMIXING

Now, we want to apply the computational model, introduced in chapter 2, to investigate the sorting dynamics for mixtures of different cell populations. The parameters used for our simulations are given in table 2.1.

If not stated otherwise, we pick for the pili-substrate interactions a detachment force $F_{d,ps} = 180$ pN, a detachment time $t_{d,ps} = 10$ s and an attachment rate $\gamma_{att} = 0.5$ Hz. This corresponds to the *slow* parameter set, defined in table 3.1. For the pili-pili-interactions we set the detachment force $F_{d,pp} = 360$ pN, the detachment time $t_{d,ps} = 50$ s and the attachment rate $\gamma_{att,pp} = 0.5$ Hz, corresponding to the *strong* parameter set of table 4.2. Here, we are not interested in a direct reproduction of experimental data, but we want to investigate whether, for given cell-cell-interactions, similar mechanisms lead to comparable internal structures of microcolonies . Thus, the parameters describing the pili-pili- and pili-substrate interactions may differ from the values expected experimentally.

For wildtype cells, we found that colonies form within one hour and remain stable after formation, as can be seen in figure 5.5a.

Next, we simulated a 50:50 mixture of WT and ΔpilT mutant cells. For ΔpilT mutant cells, the pilus retraction velocity was set $v_{ret} = 0$. In figure 5.3b we show the initial state and the microcolonies that formed after one hour. We observe a behavior that agrees with experimental results: while the mutant cells are concentrated at the surface of the colonies, the wildtype cells are mainly found in the bulk of

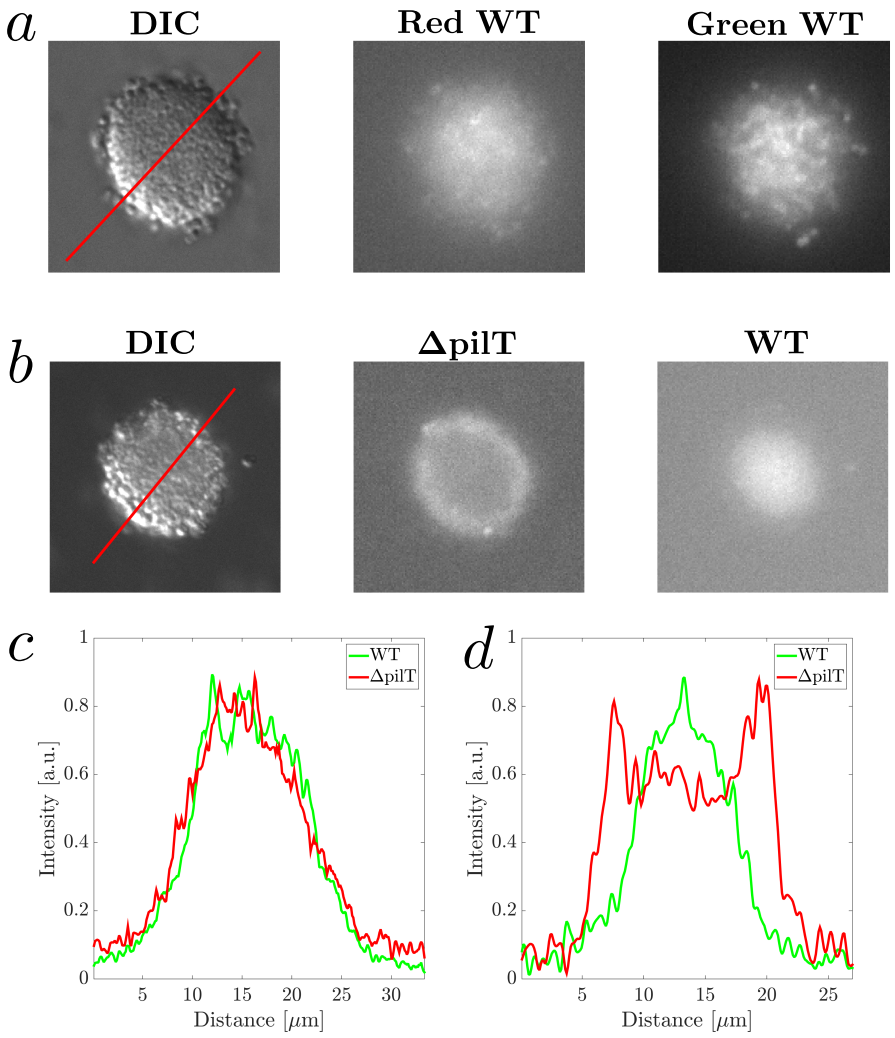

Figure 5.2: Demixing of a mixture of wildtype cells and a ΔpilT mutant of *Neisseria gonorrhoeae*. The figure was adapted from [124]. (a) DIC (differential interference contrast microscopy) and fluorescence images allowed to detect the positions of two populations of WT cells. Here, green represents labeling with YFP, and red represents tdtomato labeling. (b) DIC and fluorescence images allowed to detect the positions of a colony formed from wildtype cells (labeled with YFP) and ΔpilT mutants (labeled with mcherry). The mutant cells are concentrated at the edge of the colonies. (c,d) We quantify the intensity profile along the red lines in (a,b). The intensity is assumed to be directly proportional to the concentration of the cells. For a mixture of two wildtype populations we do not see any demixing, for a mixture of wildtype cells and ΔpilT mutants, the demixing is observed.

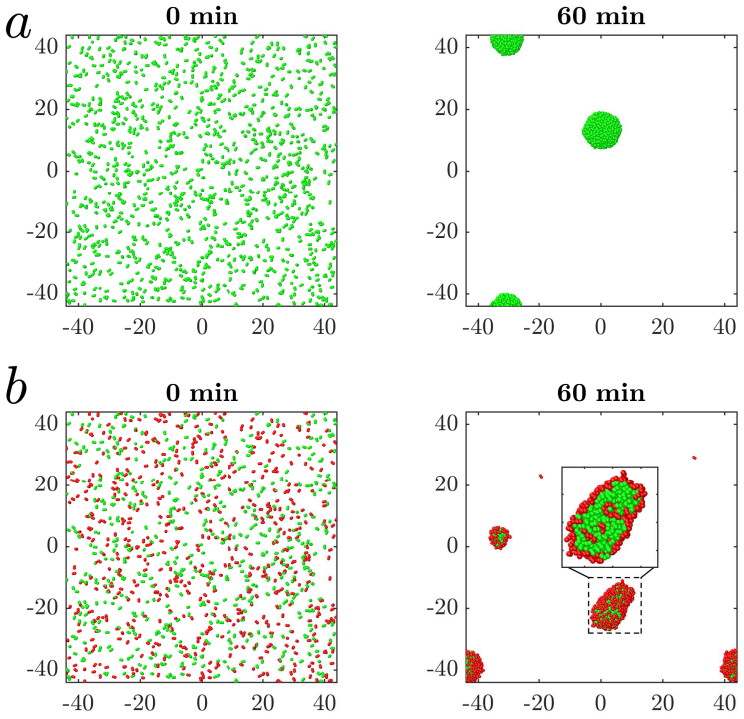

Figure 5.3: Top view of the assembly of *in silico* microcolonies of wildtype cells and ΔpilT mutant cells. The figure was adapted from [60]. (a) Assembly of 1200 cells on a substrate. After initializing cells homogeneously on the substrate (left), colonies begin to form after a few minutes. They grow by single cells colliding with the less motile colonies. After one hour, almost all cells are assembled into colonies. (b) Mixture of normal cells (green) and ΔpilT mutants (red). These mutants have pili which cannot pull. The colonies form within one hour. The inset depicts a close-up in of a typical colony and shows that the mutant cells accumulate at the surface of the colony.

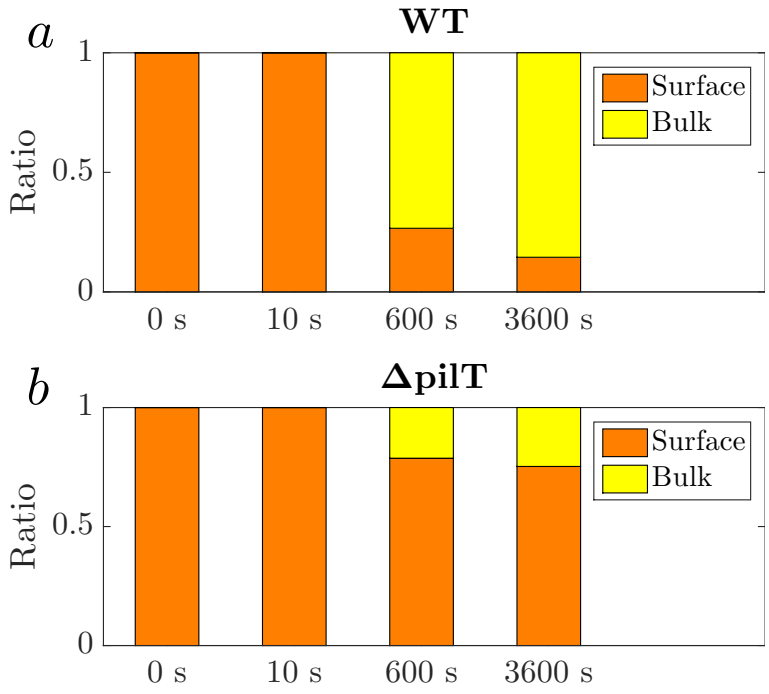

Figure 5.4: Ratio of surface and bulk cells for *in silico* wild-type and ΔpilT cells. If a cell is part of the colony surface or bulk was estimated by computing the alpha shape of the cells. The figure was adapted from [60]. (a) Ratio of wild-type (WT) cells at the surface (orange) and inside of the colony (yellow). The colonies form such that within 10 minutes (600 s), the wild-type cells can be found preferentially inside of the colonies. (b) Ratio of mutant cells identified as surface (orange) and bulk (yellow) cells. A larger fraction of ΔpilT mutants can be found on the surface of the colonies.

the colonies. We could also quantify this behavior by directly identifying which cells are surface cells of a colony and which cells can be found within the bulk of the colony. We determined surface cells by computing the alpha shape of the *in silico* microcolony [125, 126] (alpha radius $R_\alpha = 1$ μm). More information about how the alpha shape helps us to identify surface cells and technical details are given in appendix F.4. For the wildtype cells and the mutant cells we computed the fraction of cells that belong to the colony surface and the fraction that belongs to the bulk (see figure 5.4). We observe that wildtype cells are preferentially located in the bulk of colonies, the ΔpilT mutant cells are located at the surface of the colonies.

Next to the demixing of wildtype cells and ΔpilT mutants, we could also simulate the demixing dynamics for the cell populations investigated by Oldewurtel et al. [57] (see figure 5.1). Similarly to the experiment, in the simulations we do not observe any demixing of two populations of wildtype cells (see figure 5.5a). When we mix wildtype cells and cells without any pili, we observe that the cells with pili form microcolonies. Cells without pili are not able to move or to interact via pili. Thus, they are not incorporated into microcolonies (see figure 5.5b). In order to simulate the mixture of two cell

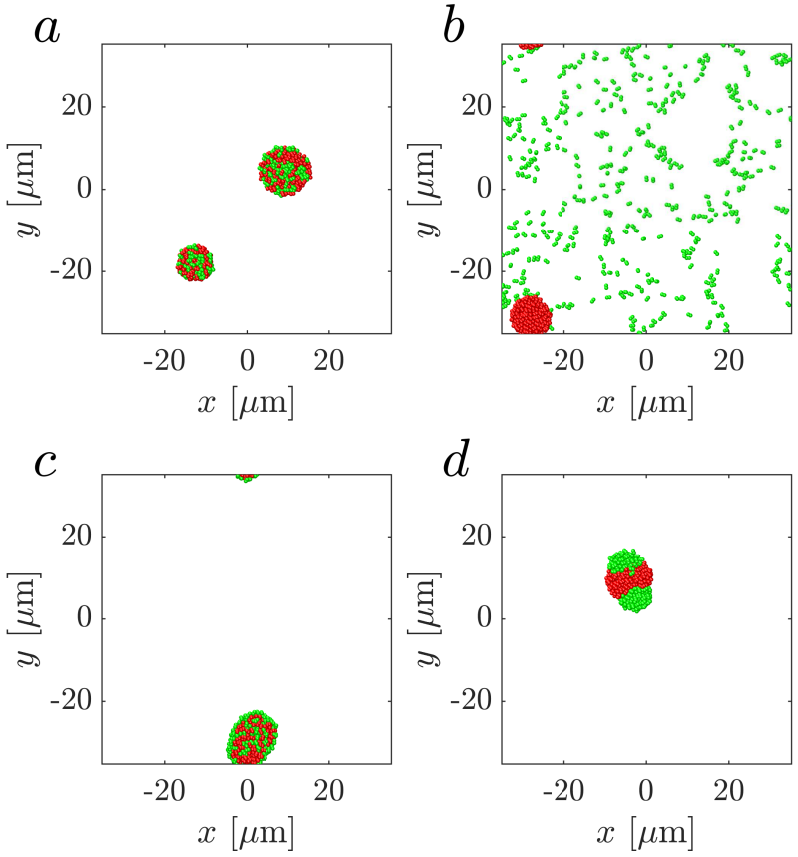

Figure 5.5: Top view of the mixing and demixing of different types of *in silico* cells, simulated from the computational model. Here, we try to mimic the midplane of the colonies by only showing cells that have a maximal distance of 6 μm from the substrate. (a) Mixture of two differently labeled populations of normal cells. (b) Mixture of normal cells (red) and mutant cells without any pili (green). (c) Mix of normal cells (green) and cells with an increased mean pili number (red). (d) Mixture of normal cells (red) and cells with altered pili-pili interactions (green). Similar to the experiment, the individual cell populations form distinct colonies.

population with different number of pili, we changed the maximal number of pili N_{max} a cell possesses and the pilus production rate γ_{prod} of pili. For the first cell population, these parameters where chosen to be $N_{max} = 15$ and $\gamma_{prod} = 15$ Hz (equivalent to table 2.1). For the second population, we chose $N_{max} = 25$ and $\gamma_{prod} = 25$ Hz. We observe, that the cells with less pili are located at the surface of colonies, the cells with a higher number of pili are preferentially located within the bulk (see figure 5.5c). Analogously to our analysis of a mixture of ΔpilT cells and wildtype cells, we could verify the demixing by identifying surface and bulk cells with the help of the alpha shape of the cells.

The last case we considered is the mixture of cells with different pili-pili binding properties. Therefore, we defined two populations a and b and redefined the pilus-pilus detachment forces $F_{d,pp}$ in the following way: $F_{det,pp}^{(aa)} = 360$ pN, $F_{det,pp}^{(ab)} = 180$ pN and $F_{det,pp}^{(bb)} = 540$ pN. We observe that each cell population creates distinct microcolonies. The chosen values were motivated by experimental results [57]. These colonies are also able to attract each other and will form larger aggregates (see figure 5.5d).

5.3 BACTERIAL CELL SORTING AND THE DIFFERENTIAL ADHESION HYPOTHESIS

In 1955 Townes and Holtfreter published a study describing the spontaneous self-organization of dissociated amphibian cells *in vitro*, forming structures that were identical to those known from *in vivo* measurements [127]. Eight years later, Steinberg was able to explain this behavior with the so called "differential adhesion hypothesis" [128, 129].

In the "differential adhesion hypothesis" it is assumed that cells have properties comparable to liquids. Similarly to a water droplet consisting of a high number of mobile molecules, a tissue consists of a high number of moving cells. If one mixes different populations of cells, possessing different mechanical and adhesive properties, the cells tend to rearrange such that they are able to maximize the relative bonding energies between the interfaces of the cells. Dependent on the specific properties of the cells, one can observe mixing or demixing of the cell populations [129].

Such a behavior has also been observed experimentally for microcolonies of *Neisseria gonorrhoeae* [57] (see figure 5.1). With the help of our computational model, we were able to reproduce the experimentally observed behavior for mixtures of two populations of bacteria with different properties of their pilus machinery (see section 5.2).

The fact that the "differential adhesion hypothesis" is able to explain the mixing behavior of different bacteria populations is to be expected, because the hypothesis it is based on very general principles of demixing of fluids. Surprising is the observation that such a behavior for mixtures of wildtype cells and mutants can be generated without directly altering the adhesive properties of the cells and

their pili. For the ΔpilT mutant we observe demixing of cells in experiments (see figure 5.2) and in our simulations (see figure 5.3). For those cells, the direct interactions of the pili of the two cell populations are identical, but the force generation of the mutant cells is malfunctioning. Thus, we observe demixing of cells within bacterial aggregates due to alterations of the active force generation, instead of differences in the passive adhesive properties.

5.4 SUMMARY

In this chapter, we studied the demixing of two cell populations of *Neisseria gonorrhoeae* for mixtures of wildtype cells and different types of mutants. The observed behavior agrees with general predictions of the "differential adhesion hypothesis". Differences in the adhesive properties of the cells can cause demixing of the populations. We were able to identify a new mechanism of demixing, which is not based on the passive adhesive properties, but differences in the active force generation.

After studying how differences in the force generation of pili in bacteria can lead to demixing of microcolonies, in the next chapter we will study the dynamics of the formation of microcolonies from single cells.

6

SELF-ASSEMBLY OF MICROCOLONIES

In the previous chapters we studied how bacterial cells and colonies move on a substrate (see chapter 3) and how two smaller colonies coalesce to form a larger colony (see chapter 4). Now, we study how these processes mediate the self-assembly of *Neisseria gonorrhoeae* microcolonies.

We investigate how aggregation, proliferation and fragmentation drive colony formation experimentally and with the help of a master equation, describing how the colony size density behaves as a function of time.

6.1 AGGREGATION OF COLONIES IN THE EXPERIMENT

To study how colonies form, we investigate how individual cells assemble to microcolonies on a glass substrate by computing the time-dependence of the size distribution of aggregates.

The data was contributed by Nicolas Biais (Brooklyn College, New York) and analyzed previously in the group of Vasily Zaburdaev (Max Planck Institute for the Physics of Complex Systems, Dresden, Germany). It consist of binary images of the detected edges of bacterial aggregates that were forming on top of the substrate (see figure 6.1a and 6.1b). In total 20 movies of colony assembly, each of a duration of 189 minutes, were analyzed.

In the experimental data we observe that a fraction of individual cells and small aggregates were not moving during the complete duration of the movie. The cells are immobile either due to the lack of pili or due to the lack of the ability to retract them. In order to estimate the number of cells that do not move, we sum up all binary images of each movie and threshold this image (details in appendix E.4). An example for the resulting binary image is shown in figure 6.1c. These images later allowed us to estimate the properties of the non-moving aggregates.

From the binary images of the aggregates, we can estimate their areas A. From the area, we can estimate the number of cells N in the aggregates by assuming that the number is proportional to the volume $V \propto R^3$ of a sphere of radius R with the same projected area as the one measured,

$$N \propto R^3 \propto A^{\frac{3}{2}}. \tag{6.1}$$

We take the proportionally coefficient computed from our computational model (see appendix F.3.2) as direct input to compute the number from the area of aggregates, given by

$$N = 2.92 \frac{R^3}{\mu m^3} = 2.92 \left(\frac{A}{\pi \, \mu m^2} \right)^{\frac{3}{2}}. \tag{6.2}$$

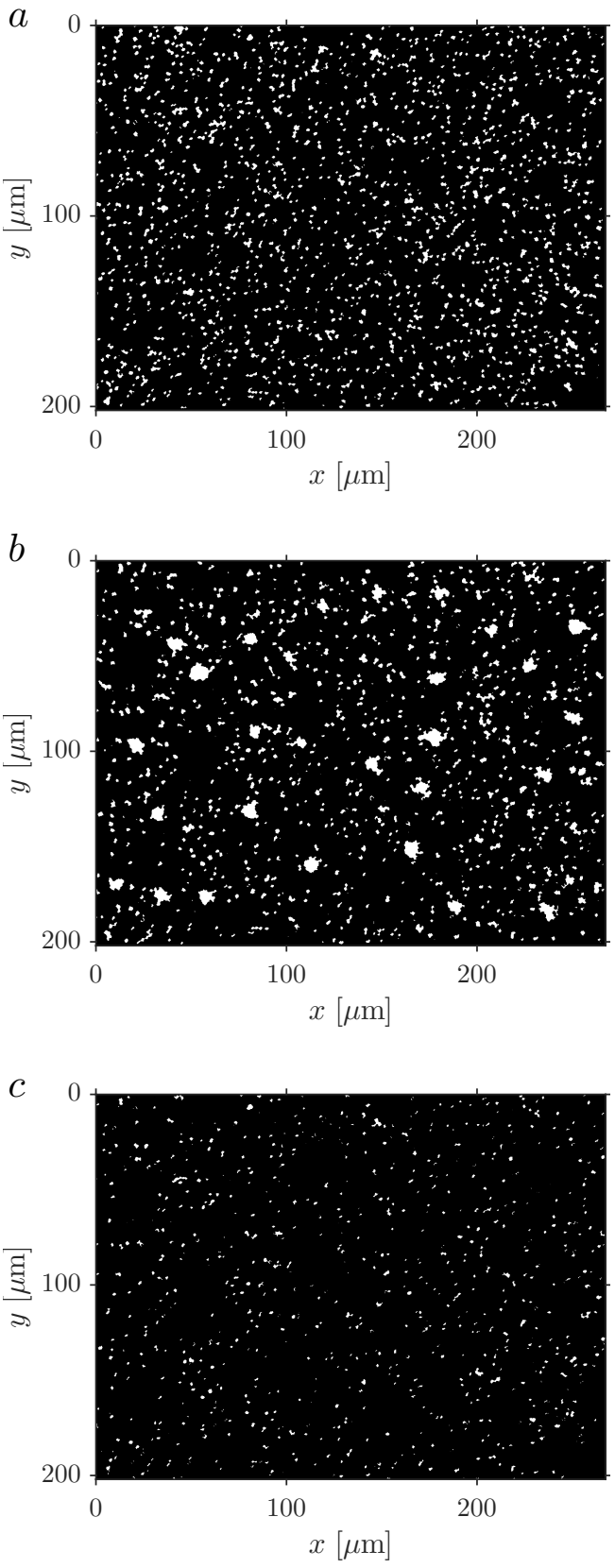

Figure 6.1: Binary images of colony assembly on a substrate at time (a) $t = 0$ min and (b) $t = 180$ min. Additionally, in figure (c) we show the binary image of the fraction of aggregates that were not moving during the experiment.

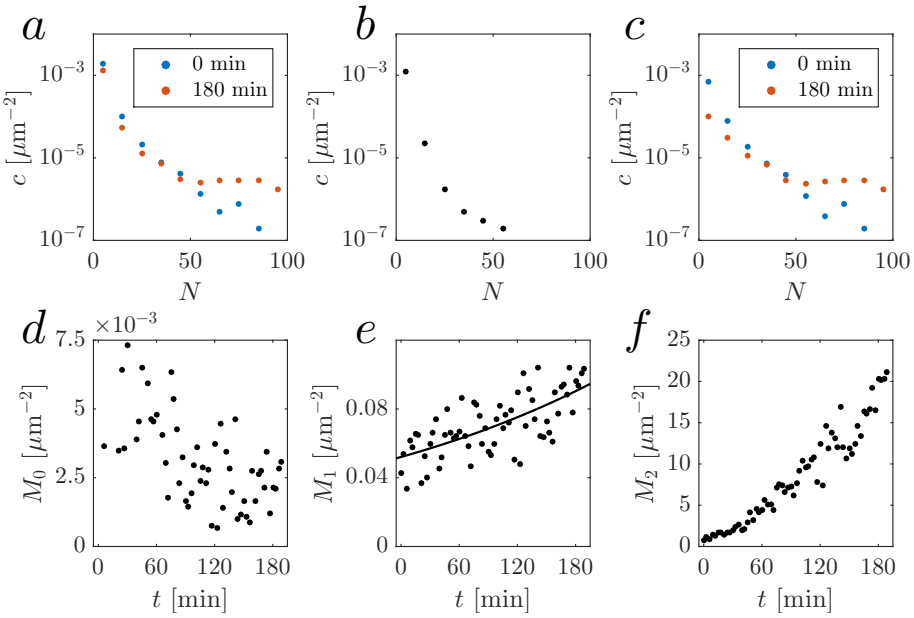

Figure 6.2: Surface density of colonies of different sizes. (a) Densities at two time points $t = 0$ min and $t = 180$ min. (b) Densities of non-moving aggregates. (c) Densities of moving aggregates for two times $t = 0$ min and $t = 180$ min. (d) Zeroth moment of the density of colonies, corresponding to the number of aggregates. (e) First moment of the densities of colonies, corresponding to the total number of cells. The black line describes exponential growth (see equation 6.4). (f) Second moment of the densities of colonies, corresponding to the with of the distribution.

We then compute the density of aggregates as a function of the numbers of cells within the aggregate, called $c(N, t)$ with the cell number N and the time t. To be more specific, the colony size density $c(N, t)$ is defined as the function describing the number of colonies consisting of N cells at time t, divided by the area of the substrate in which the colonies can be found.

The resulting densities of the initial state of the experiment and after three hours are shown in figure 6.2a, details of the computation are given in appendix F.4. We can also compute the density of the colony sizes for the fraction of aggregates which do not move during the experiment (see figure 6.2b). The difference between these two densities gives us the density of aggregates that are moving on a substrate, shown in figure 6.2c. As one can see, due to the subtraction of aggregates that were not moving, the difference of the density of smaller aggregates changes considerably over time. For long times, it appears that smaller colonies become less likely, probably by incorporating them into larger microcolonies and due to cell divisions.

To quantify the time-dependent behavior of the density c of moving cells and colonies, we calculated the moments

$$M_i(t) = \sum_{N=1}^{\infty} N^i c(N, t), \tag{6.3}$$

where i is the order of the moment, N is the number of cells within the aggregate and t is the time. In figure 6.2d one can see that the zeroth

moment M_0 is decreasing with time. This results from the aggregation of colonies due to which two cells or colonies form one larger aggregate. The first moment M_1, shown in figure 6.2e, corresponds to the full number of cells, divided by the area of the substrate. Due to cell divisions, this number will increase exponentially. By fitting an exponential function of the form

$$M_1(t) = M_1^{(0)} \exp\left(\frac{t}{t_{div}}\right) \tag{6.4}$$

we can estimate the initial density of cells and colonies,

$$M_1^{(0)} = (0.04 \pm 0.01)\ \mu m^{-2}, \tag{6.5}$$

and the cell division time

$$t_{div} = (261 \pm 60)\ \text{min}. \tag{6.6}$$

This time is in the same order of magnitude as reported in the literature [107]. The second moment M_2, shown in figure 6.2f, corresponds to the width of the distribution and is increasing with time.

In the next section, we study these experimental observations with the help of the master equation of the colony size density and we show that aggregation of colonies is the central driving mechanism of the observed behavior of the colony size density and its moments.

6.2 THEORETICAL DESCRIPTION OF COLONY FORMATION

We now define a master equation, characterizing the temporal dynamics of the density $c(N,t)$, which, as defined in the previous section, is the number of colonies consisting of N cells at time t, divided by the area of the substrate. Such an approach has been extensively discussed in the literature, for example [130].

Our model is based on the following assumptions:

- The system is translationally invariant, allowing us to use $c(N,t)$ instead of $c(\mathbf{r},N,t)$ with the spatial coordinate $\mathbf{r}$.
- We only consider binary interactions of colonies. Higher order interactions will be ignored.
- The colony interactions are independent of their shape. For simplicity, we assume that all colonies have a spherical shape.

The master equation has the general form:

$$\frac{dc(N,t)}{dt} = C(N,t) + A(N,t) + F(N,t), \tag{6.7}$$

where $C(N,t)$ denotes proliferation, $A(N,t)$ aggregation and $F(N,t)$ fragmentation of colonies (see 6.3).

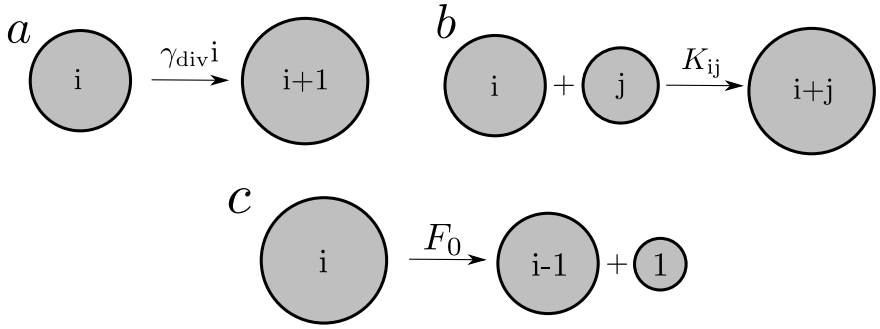

Figure 6.3: Sketch of the mechanisms that drive microcolony growth. (a) With the rate $\gamma_{div} i = i/t_{div}$ a colony of size i grows due to the division of one cell within the colony. (b) Colonies of size i and j merge irreversibly to a colony of size $i+j$ with the rate K_{ij}. (c) Fragmentation of a colony due to the separation of a single cell with the rate F_0.

Cell division

We assume that each cell divides with the rate γ_{div}. Then, the rate for which a colony, consisting of i cells, switches states $\{i\} \to \{i+1\}$ is given by $i\gamma_{div}$ (see figure 6.3a). This transition rate can be derived by considering the probability density function of the cell division time of a single cell, given by

$$p(t) = \gamma_{div} \exp\left(-t\gamma_{div}\right). \tag{6.8}$$

The probability that the division takes place after a time larger than a value t' is given by

$$P(t') = \int_{t'}^{\infty} dt\; p(t) \tag{6.9}$$

$$= \exp\left(-t'\gamma_{div}\right). \tag{6.10}$$

For i cells, the probability that none of the cells divide after time t' is given by

$$P_i(t') = P(t')^i. \tag{6.11}$$

Finally, the probability density function of times that any cell will divide is then given by

$$p_i(t') = -\dot{P}_i(t') \tag{6.12}$$

$$= \gamma_{div} i \exp\left(-t'\gamma_{div} i\right), \tag{6.13}$$

such that the rate of the transition is given by $i\gamma_{div}$.

The contribution of cell divisions to the master equation takes the form

$$C(N,t) = c(N-1,t)(N-1)\gamma_{div} - c(N,t)N\gamma_{div}. \tag{6.14}$$

Here, the first term is the gain term, corresponding to the transition $\{N-1\} \to \{N\}$. The second term is the loss term, describing the transition $\{N\} \to \{N+1\}$.

For the initial condition $c(N,0) = c_0\delta(N-1)$ with the delta function $\delta(x)$, we can write down the first three differential equations

$$\frac{dc(1,t)}{dt} = -c(1,t)\gamma_{div}, \tag{6.15}$$

$$\frac{dc(2,t)}{dt} = c(1,t)\gamma_{div} - c(2,t)2\gamma_{div}, \tag{6.16}$$

$$\frac{dc(3,t)}{dt} = c(2,t)2\gamma_{div} - c(3,t)3\gamma_{div} \tag{6.17}$$

and solve them

$$c(1,t) = c_0 \exp(-\gamma_{div}t), \tag{6.18}$$

$$c(2,t) = c_0 \exp(-\gamma_{div}t)\left[1 - \exp(-\gamma_{div}t)\right], \tag{6.19}$$

$$c(3,t) = c_0 \exp(-\gamma_{div}t)\left[1 - 2\exp(-\gamma_{div}t) + \exp(-2\gamma_{div}t)\right], \tag{6.20}$$

suggesting the general solution

$$c(N,t) = c_0 \exp(-\gamma_{div}t)\left[1 - \exp(-\gamma_{div}t)\right]^{N-1} \tag{6.21}$$

that also fulfills the system of differential equations. For this solution we see that

$$c(N) \geqslant c(N+1), \tag{6.22}$$

so that, for the initial condition $c(N,0) = c_0\delta(N-1)$, the maximum of the distribution is located at $N = 1$, independent of time.

It is also interesting to the study the first moments of the colony number density for cells that are only able to divide. The dynamics of such a system can be described by the master equation

$$\frac{dc(N,t)}{dt} = C(N,t). \tag{6.23}$$

The zeroth moment M_0 (see equation 6.3), corresponding to the number of aggregates divided by the area, then follows from

$$\begin{aligned}\frac{dM_0}{dt} &= \sum_{N=1}^{\infty} \frac{dc(N,t)}{dt} \\ &= \sum_{N=1}^{\infty} c(N-1,t)(N-1)\gamma_{div} - \sum_{N=1}^{\infty} c(N,t)N\gamma_{div} \\ &= \sum_{N=1}^{\infty} c(N,t)N\gamma_{div} - \sum_{N=1}^{\infty} c(N,t)N\gamma_{div} \\ &= 0.\end{aligned} \tag{6.24}$$

Thus, we see that M_0 is constant and the number of aggregates is conserved. This is a result of the proliferation, where we assume that no individual colonies or cells are getting created or destroyed.

The first moment, corresponding to the total number of all cells within the colonies per unit area is given by

$$\begin{aligned}\frac{dM_1}{dt} &= \sum_{N=1}^{\infty} N\frac{dc(N,t)}{dt}\\ &= \sum_{N=1}^{\infty} c(N-1,t)N(N-1)\gamma_{div} - \sum_{N=1}^{\infty} c(N,t)N^2\gamma_{div}\\ &= \sum_{N=1}^{\infty} c(N,t)(N+1)N\gamma_{div} - \sum_{N=1}^{\infty} c(N,t)N^2\gamma_{div}\\ &= \sum_{N=1}^{\infty} Nc(N,t)\gamma_{div}\\ &= \gamma_{div}M_1. \end{aligned} \tag{6.25}$$

The solution of this equation is given by

$$M_1(t) = M_1^{(0)}\exp(\gamma_{div}t), \tag{6.26}$$

$$M_1(0) = M_1^{(0)}. \tag{6.27}$$

Thus, the number of cells in the system increases exponentially with the rate γ_{div}, as expected for bacterial growth.

For the second moment we get

$$\begin{aligned}\frac{dM_2}{dt} &= \sum_{N=1}^{\infty} N^2\frac{dc(N,t)}{dt}\\ &= \sum_{N=1}^{\infty} c(N-1,t)N^2(N-1)\gamma_{div} - \sum_{N=1}^{\infty} c(N,t)N^3\gamma_{div}\\ &= \sum_{N=1}^{\infty} c(N,t)(N+1)^2N\gamma_{div} - \sum_{N=1}^{\infty} c(N,t)N^3\gamma_{div}\\ &= \sum_{N=1}^{\infty} (N+2N^2)c(N,t)\gamma_{div}\\ &= \gamma_{div}M_1 + 2\gamma_{div}M_2. \end{aligned} \tag{6.28}$$

The solution of this differential equation is given by

$$M_2(t) = \exp(2\gamma_{div}t)\left(M_2^{(0)} + M_1^{(0)}\right) - \exp(\gamma_{div}t)\,M_1^{(0)}, \tag{6.29}$$

$$M_2(0) = M_2^{(0)}. \tag{6.30}$$

As expected, the width of the density increases with time.

Aggregation

Microcolonies are moving on a substrate with the help of their pili (see chapter 3). When two colonies come close to each other, they will coalesce, forming a new larger colony (see chapter 4). This process

is one of the driving mechanisms of colony formation. In our master equation it is incorporated by

$$A(N,t) = \frac{1}{2}\sum_{i+j=N} K_{ij}c(i,t)c(j,t) - \sum_{i} K_{iN}c(N,t)c(i,t), \tag{6.31}$$

see [130]. The first term is the gain term, corresponding to the coalescence of two colonies $\{i\}+\{j\} \to \{N\}$, forming a colony of size N. The second term is the loss term, defining the transition $\{N\}+\{i\} \to \{N+i\}$.

Here, K_{ij} is the transition rate. In two dimensions $d = 2$, a particle that moves with a diffusion coefficient D hits a circle with radius R with the rate

$$K \propto DR^{d-2} = D, \tag{6.32}$$

as shown in [130, 131]. Thus, we can define the transition rate to be

$$K_{ij} = K_0\left(D_i + D_j\right), \tag{6.33}$$

with the proportionality constant K_0. Here, D_i is the diffusion coefficient of a colony, consisting of i cells.

In experiments it was shown that the diffusion coefficient of colonies on top of a glass surface decreases with increasing colony size [59]. Naively, one may assume that the diffusion coefficient could follow the Stokes-Einstein relation, describing the diffusion due to thermal brownian motion and given by

$$D = \frac{kT}{6\pi\eta R}, \tag{6.34}$$

where k is the Boltzmann constant, T is the temperature, η the viscosity of the fluid a spherical particle is moving in and R is the radius of this particle [132]. As shown in figure 6.4 it appears to decrease faster than predicted by this relation.

Instead, as one can see in figure 6.4, a function of the form

$$D_i = \begin{cases} \frac{0.47}{R_i}\ \frac{\mu m^3}{s}, & R_i \leqslant 1.5\ \mu m \\ \frac{0.70}{R_i^2}\ \frac{\mu m^4}{s}, & R_i > 1.5\ \mu m \end{cases}, \tag{6.35}$$

can describe the behavior of the diffusion coefficient of a colony moving on a glass substrate. The radius R_i of a colony consisting of i cells results from the proportionality of the cell number i to the volume of the colony $i \propto R_i^3$ (see appendix F.3.2). The the substrate of the presented assembly data is glass.

Due to the complex form of the rates K_{ij}, we cannot give an analytical expression for all moments of the system given by

$$\frac{dc(N,t)}{dt} = A(N,t). \tag{6.36}$$

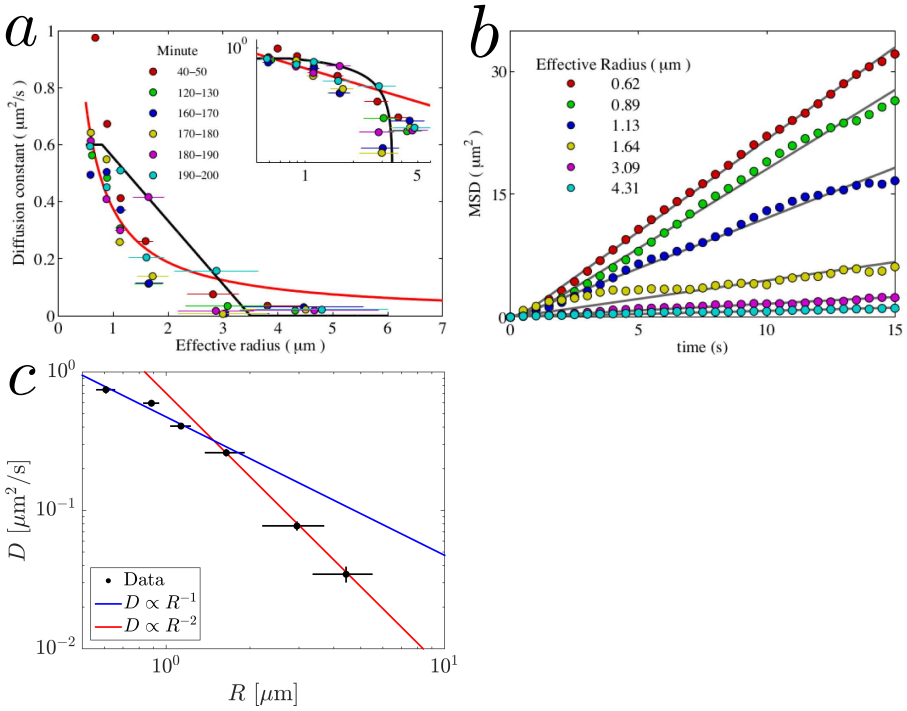

Figure 6.4: *In vitro* microcolony motility as a function of the colony size for colonies moving on a glass surface. Figures (a,b) and the underlying data of figure (c) were taken from [59]. (a) Diffusion coefficient of *in vitro* microcolonies moving on a substrate for different time points. (b) Mean squared displacement of microcolonies of different sizes. (c) Averaged Diffusion coefficient of microcolonies moving on a substrate. Here we combined the data for the different time points. As one can clearly see, the diffusion coefficient decreases faster than predicted by the Stokes-Einstein relation where $D \propto R^{-1}$.

Instead, we will draft an approach to compute the moments and discuss their general behavior. For the moments of order x we have

$$\begin{aligned}\frac{dM_x}{dt} &= \sum_{N=1}^{\infty} N^x \frac{dc(N,t)}{dt} \\ &= \sum_{N=1}^{\infty} \sum_{i+j=N} \frac{1}{2}(i+j)^x K_{ij} c(i,t) c(j,t) \\ &\quad - \sum_{N=1}^{\infty} \sum_{i=1}^{\infty} N^x K_{in} c(N,t) c(i,t) \\ &= \sum_{i=1}^{\infty} \sum_{j=1}^{\infty} \left[\frac{1}{2}(i+j)^x - j^x \right] K_{ij} c(i,t) c(j,t). \end{aligned} \tag{6.37}$$

For the zeroth moment, corresponding to the number of aggregates per unit area we get

$$\frac{dM_0}{dt} = -\sum_{i=1}^{\infty} \sum_{j=1}^{\infty} \frac{1}{2} K_{ij} c(i,t) c(j,t) \leqslant 0. \tag{6.38}$$

For $K_{ij} > 0$, the zeroth moment decreases due to the irreversible coalescence of colonies.

The derivation of the first moment follows from

$$\frac{dM_1}{dt} = \sum_{i=1}^{\infty} \sum_{j=1}^{\infty} \frac{1}{2}(i-j) K_{ij} c(i,t) c(j,t) = 0 \tag{6.39}$$

and vanishes due to the relation $K_{ij} = K_{ji}$. We do not consider any proliferation of the cells in this simplified system, thus the first moment must be constant.

The second moment will increase in time, as resulting from

$$\begin{aligned}\frac{dM_2}{dt} &= \sum_{i=1}^{\infty} \sum_{j=1}^{\infty} \left(\frac{i^2}{2} + ij - \frac{j^2}{2} \right) K_{ij} c(i,t) c(j,t) \\ &= \sum_{i=1}^{\infty} \sum_{j=1}^{\infty} ij K_{ij} c(i,t) c(j,t) \geqslant 0. \end{aligned} \tag{6.40}$$

Fragmentation

Next to mechanisms that lead to a growth of microcolonies, we also consider fragmentation, the separation of a single cell from a microcolony. Here, we consider the simplest case where each aggregate loses single cells with a constant rate F_0. This is incorporated in the master equation by

$$F(N,t) = F_0 \begin{cases} c(N+1,t) - c(N,t) & , N \geqslant 2 \\ c(2,t) + \sum_{k=2}^{\infty} c(k,t) & , N = 1 \end{cases}. \tag{6.41}$$

Aggregates consisting of more than one cell $N > 1$ have a gain term corresponding to the transition $\{N+1\} \to \{N\} + \{1\}$ and a loss term

corresponding to the transition $\{N\} \to \{N-1\}+\{1\}$. Single cells only have a gain term. Here it is important to notice that for the transition $\{2\} \to \{1\}+\{1\}$ two single cells are generated.

For equation 6.41 we can also compute general expressions of the moments, as given by

$$\begin{aligned}\frac{dM_x}{dt} &= \sum_{N=1}^{\infty} N^x \frac{dc(N,t)}{dt} \\ &= F_0 c(2,t) + F_0 \sum_{N=2}^{\infty} c(N,t) \\ &+ F_0 \sum_{N=2}^{\infty} N^x c(N+1,t) - F_0 \sum_{N=2}^{\infty} N^x c(N,t). \end{aligned} \tag{6.42}$$

For the first three moments we find

$$\frac{dM_0}{dt} = F_0 \sum_{N=2}^{\infty} c(N,t) \geqslant 0, \tag{6.43}$$

$$\frac{dM_1}{dt} = 0, \tag{6.44}$$

$$\frac{dM_2}{dt} = -2F_0 \sum_{N=2}^{\infty} c(N,t)(N-1) \leqslant 0. \tag{6.45}$$

While the total number of aggregates is increasing, no new cells are produced and the second moment is decreasing.

Solution of the master equation describing the dynamics of the colony size density

We were solving the master equation 6.7 numerically with an Euler algorithm and a time step $\Delta t = 0.02$ s. This time is small enough to guarantee that transitions where more than one cell divides within a colony, for example $\{N\} \to \{N+2\}$, are negligible. For the numerical solution we assumed that the maximal colony size is given by 3000 cells. We assume that initially we only start with single cells. In the experiment small aggregates have already formed, as can be seen in figure 6.2a, due to the time lag between the transfer of the cells on the glass slide and the beginning of the microscopy. Thus, we introduce a lag time $t_{lag} = 650$ s such that the time point $t = 0$ in the experiment corresponds to the time t_{lag} in the master equation. The initial density profile was chosen such that

$$c(N,0) = \begin{cases} 0.047\ \mu m^{-2}, & N = 1 \\ 0, & N > 1 \end{cases}. \tag{6.46}$$

We consider three different cases of colony growth of increasing complexity. The corresponding results are as shown in figure 6.5. First, we only considered cell divisions with the time $t_{div} = 238$ min. As shown in figure 6.5, in this case the zeroth and the second moment differ clearly from the experiment. Then, we included aggregation with the parameter $K_0 = 0.72$. In this case, the behavior of the

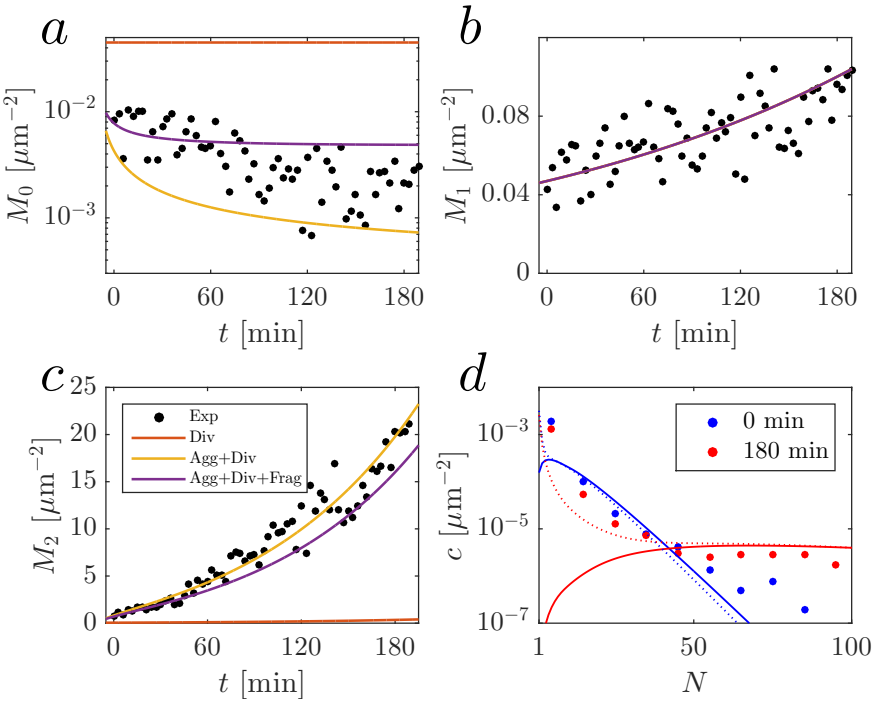

Figure 6.5: Surface density and moments of colonies of different sizes from the master equation. The times t were defined by the experiment, where $t = 0$ in the plots corresponds to $t = t_{lag}$ in the master equation. (a) The zeroth moment of the surface density, corresponding to the total number of aggregates per unit area. The black dots represent the experimental results for motile cells and colonies, the lines show the zeroth moment, as computed from the master equation 6.7 (the colors correspond to the legend of (c)). (b) First moment of the surface density, corresponding to the number of cells in the system. Independent of aggregation or fragmentation, the increase of the number of cells is solely influenced by cell divisions. (c) Second moment of the density, corresponding to its width. Here "Div" corresponds to the first case where we only consider cell divisions, "Agg+Div" corresponds to the case where we consider cell divisions and aggregation and "Agg+Div+Frag" additionally considers the fragmentation. Only the cases where we consider the aggregation of colonies are able to reproduce the experimental data. (d) Surface density of colonies consisting of N cells for different time points for the model. The points show the experimentally measured densities of moving aggregates, the solid lines correspond to the case "Agg+Div", the dotted line corresponds to "Agg+Div+Frag".

moments agrees with the experiment, but we observe a extinction of aggregates consisting of 1 to 10 cells for the time $t = 180$ min, which does not coincide with our experimental observations. By considering fragmentation with the rate $F_0 = 4 \times 10^{-3}$ Hz, we observe a qualitatively similar behavior of the moments and the colony size density for the solution of the master equation and the experiment. The chosen parameters for the division time t_{div} and the initial density $c(N, 0)$ are in agreement with the values measured experimentally in section 6.1. To find K_0 and F_0 we sampled over a wide range of values.

As one can see in figure 6.5d, for larger times the density of individual cells and small aggregates becomes smaller and larger aggregates become more likely. Due to the form of transitions that we consider for the master equation, the colony size density diverges towards an infinitely large microcolony. A process which we do not consider in our model, due to the lack of experimental data, is the apoptosis of cells, which may create a stationary state for $t \to \infty$. Such a process would introduce the destruction of cells and could, for example, be dependent on the size of the colonies.

To summarize, we can conclude that the interplay of aggregation, fragmentation and cell divisions drives the formation of bacterial microcolonies.

6.3 SUMMARY

By measuring the colony size surface density experimentally and comparing it to the predictions of a simple master equation, we were able to identify aggregation, fragmentation and proliferation as the main processes that govern the dynamics of bacterial colony self-assembly. We found that particularly aggregation and fragmentation seem to take a leading role in colony formation. A model in which colonies only grow by cell divisions is not able to reproduce the experimental data. Additionally, when we neglect fragmentation of colonies, we observe an extinction of the small aggregates that we do not detect in our experiments. The presented master equation offers a simple mathematical description of the dynamics of colony formation of *Neisseria gonorrhoeae*. It has only a small number of free parameters, the initial density of single cells $c(N, 0)$, the division time t_{div}, the fragmentation rate F_0 and the proportionality factor of the interaction kernel K_0. The initial density, the division time and the colony-size dependence of the diffusion coefficient can be estimated experimentally, leaving only two unknown parameter, F_0 and K_0.

7

SUMMARY AND OUTLOOK

SUMMARY OF THE THESIS

In this thesis, we have studied how type IV pili drive the dynamics of bacterial aggregates with the help of experiments and theory. We focused on different important aspects of bacterial dynamics, going from the motion of single cells on a substrate (see chapter 3), over the dynamics of cells within microcolonies and how they drive colony coalescence (see chapter 4 and chapter 5), up to the assembly of single cells to microcolonies consisting of up to thousands of cells (see chapter 6). To study the bacterial dynamics mediated by type IV pili, we developed a computational model (see chapter 2) and different more specialized mathematical models to study the motion of cells on a substrate (see section 3.1) and the assembly of microcolonies (see section 6.2).

In the following, we shortly want to repeat the main findings of the individual parts of the thesis:

- In chapter 3 we studied the motility of individual bacteria on a substrate, with the help of type IV pili. We showed that a wide range of previous experimental observations can be reproduced by our model. The substrate motion is driven by the collective interactions of multiple pili of a cell, causing persistent motion with characteristic lengths that can exceed the pili length. We show that this behavior is not necessarily caused, as previously suggested [34], by directional memory of the pili dynamics. Instead, persistent motion emerges from a tug-of-war of several pili.

- In chapter 4 we could show experimentally and by our computational model that the merging of colonies differs from simple viscous fluids. For bacterial microcolonies, the characteristic times of the bridge closure differ from the characteristic time of the relaxation of an ellipsoidal colony towards a spherical shape. We could provide experimental evidence to explain the coalescence, which is driven by a gradient of motility within the colony. While cells at the surface are highly motile, cells within the colony bulk exhibit a weak motility only. With the help of our computational model we found that besides the difference in motility, the colony possesses more fluid-like properties. We suggest that the motility gradient is a result of a spatial dependence of the cell density within the colony, differences of the dynamics of pili bindings and the forces mediated by pili.

- Next to the dynamics within colonies of wildtype cells, we also studied the direct role of how pili organize microcolonies by

studying mixtures of wildtype cells and different mutants (see chapter 5). The mutants possess different properties of their pilus apparatus, altering the force generation. While we observe qualitative differences to predictions of the differential adhesion hypothesis, previously applied to study the demixing of cell tissues, we presented a case of demixing where alterations of the force generation drive the sorting, instead of variations of the adhesive properties of cells.

- Besides the dynamics of single cells and colonies, in chapter 6 we were also studying the assembly of multiple microcolonies. By comparing experimental data of the colony size density to an mathematical model, we could identify three processes that govern the assembly of bacterial aggregates: aggregation, fragmentation and proliferation. We found aggregation to be the main driving process of formation of large colonies. Additionally, fragmentation is needed to generate a small population of mobile single cells, as observed in experiments.

This thesis offers a new point of view how cells move on a substrate with the help of pili and how pili are involved in the formation and dynamics of bacterial aggregates. With the help of computational and mathematical models we were able to study and explain a wide range of experimental observations (from the motion of single cells, over the dynamics of microcolonies and up to the assembly of multiple colonies).

We have shown that pili-mediated forces highly affect the dynamics of bacterial cells and colonies. For example, such processes can lead to very complex behavior, as we could show for the motility of individual cells within microcolonies. We observed highly motile cells on the surface and weakly moving cells within the bulk of a colony (see chapter 4). Such differential behavior can be interpreted as the first step towards multicellular behavior (see section 1.3.2), where we first do not see variations in the genetic properties of the cells, but instead differences have a purely mechanical origin. These mechanical cues may then affect the gene expression of cells [133]. First experimental evidence pointing in this direction is shown in Pönisch et al. [124], where we observed that the gradient of motility in *N. gonorrhoeae* can be correlated with the expression of genes connected to the production of pilE, the subunits of a pilus, 7 hours after assembly. In the future, it will be interesting to apply the methods of cell rheology [134] to study the feedback of mechanical cues with the expression of a wide variety of genes connected to the pilus apparatus.

FUTURE DIRECTIONS

In the following, we will point towards multiple further directions of research for which this thesis may provide important building blocks:

- In this thesis, we study bacteria of *Neisseria gonorrhoeae* as model organism to investigate how pili mediate the dynamics of bacte-

rial cells and aggregates. Many other bacteria also utilize pili to induce motion on a substrate or the formation of microcolonies. One example of such a bacterium is *Neisseria meningitidis*, a bacterium that is found in the nasopharynx of roughly 10 % of the human population [135] and is the causative agent of meningitis, responsible for 73300 deaths in 2015 [79]. The bacteria possess a geometry identical to *Neisseria gonorrhoeae*, but have more pili and are more motile [24]. Another bacterium that uses pili for motion on a substrate is *Pseudomonas aeruginosa*. The pili of these rod-like cells are only located at the poles of the bacteria. With the help of our computational model, we can study the role of such geometrical differences. For example, *P. aeruginosa* cells exhibit two different modes of motility, dependent on the orientation of the cell relative to the substrate [26, 136–140].

- While we only studied the motion of single cells on a substrate within this thesis, the presented computational and mathematical models can also be applied to study the motion of bacterial aggregates over a substrate. Experimentally, a peculiar behavior of the diffusion coefficient depending on the colony radius was observed (see figure 6.4) where coefficient decreases rapidly with increasing colony size. The origin of this behavior remains to be unraveled.

- In section 4.3 we were discussing a discrepancy between our simulations of the internal dynamics and coalescence of microcolonies and the experimental results and concluded that this may result from a simplification of our computational model in which we only consider binary interactions of pili. In the future, it will be interesting to include the dynamics of the pili network wrapping around the cells within a colony, as seen in figure 1.5a. Such a network will reduce the mobility of cells within the bulk and on the surface of a colony.

- While we believe that our computational model offers a new tool to study bacterial dynamics, we suggest that it can also be applied to discover new approaches for the treatment of microbial diseases. By understanding the formation of microcolonies, a fundamental step in the infection process of *Neisseria gonorrhoeae*, we may be able to find ways to manipulate the assembly. For example, microbeads with a coating to which pili can attach, would alter the ability of the cells to generate forces and could help to reduce their survivability.

CONCLUDING REMARKS

In this thesis we have shown that mechanical forces, generated by type IV pili, play a fundamental role during the formation and dynamics of bacterial microcolonies, the precursors of biofilms. Experiments were studied hand in hand with theory to provide comprehensive understanding of such early biofilms. We hope that such an

interdisciplinary approach will bring further new results on the role of biophysical processes in the formation of biofilms and the adjacent fields of multicellularity and development.

A

DETAILS OF THE SIMULATION MODEL

In the simulation, we do not create or destroy pili every time step, but only every $\Delta t_{dyn} = 0.02$ s. Furthermore, within the simulation the binding and unbinding of pili is also checked every Δt_{dyn}. Due to the introduction of Δt_{dyn}, we are able to increase the simulation speed considerably, without observing a qualitative difference in the outcome. This is valid as long as the binding, unbinding and pilus creation times are larger than Δt_{dyn}. This is not the case for the *fast* parameter set (see table 3.1), for which we chose $\Delta t_{dyn} = 2.5 \times 10^{-6}$ s or smaller values. Simulations for different values of Δt_{dyn} revealed no qualitative difference.

A.1 GEOMETRY OF THE CELLS AND FREE PILI DYNAMICS

The start and end points of pilus k are given by the position vectors $\mathbf{r}_k^{(s)}$ and $\mathbf{r}_k^{(e)}$. New pili are created on the surface of the cocci and need to fulfill the conditions $|\mathbf{r}_i^{(a)} - \mathbf{r}_k^{(s)}| \geqslant R$ and $|\mathbf{r}_i^{(b)} - \mathbf{r}_k^{(s)}| \geqslant R$, where $\mathbf{r}_i^{(a)}$ and $\mathbf{r}_i^{(b)}$ are the centers of the two cocci (a) and (b) of cell i and R is the radius of the cocci.

When a free pilus of length $l_k^{(free)}$ emerges from the surface of the cell, the position of its end point is given by

$$\mathbf{r}_k^{(e)} = \mathbf{r}_k^{(s)} + l_k^{(free)} \frac{\mathbf{r}_k^{(s)} - \mathbf{r}_i^{(j)}}{R} \tag{A.1}$$

where $\mathbf{r}_i^{(j)}$ is the position of the coccus from which the pilus emerges from. The contour length $l_k^{(cont)}$ of the pilus k is given by

$$l_k^{(cont)} = |\mathbf{r}_k^{(s)} - \mathbf{r}_k^{(e)}|. \tag{A.2}$$

When a pilus is protruding or retracting, the length of the free pilus changes, according to

$$l_k^{(free)}(t + \Delta t) - l_k^{(free)}(t) = v_{pro}\Delta t \tag{A.3}$$

$$l_k^{(free)}(t + \Delta t) - l_k^{(free)}(t) = -v_{ret}\Delta t. \tag{A.4}$$

When a pilus k hits the substrate, its end point will not enter the substrate, but slide along its surface along the same $x-y-$direction as before the collision with the $z-$component being 0. In this case, the length of the pilus is the same as the free length $l_k^{(free)}$.

A.2 BINDING OF PILI TO OTHER PILI

In order to describe the binding of two pili in three-dimensional space, we consider thermal fluctuations of a semiflexible polymer.

The cone-like volume of a pilus results from the beam equation of a semi-flexible rod [94]:

$$d_{beam}(l) = \sqrt{\frac{l^3}{3l_{pers}}}, \tag{A.5}$$

where l is the distance of pilus k from its start point $\mathbf{r}_k^{(s)}$. The shape of such a beam is shown in figure 2.1C.

The binding of two pili is modeled by randomly picking a free pilus k with a rate $\gamma_{att,pp}$ that is described as the cone. This pilus checks with rate $\gamma_{att,pp}$ whether it can bind to any surrounding pilus within the cone. If there is an available pilus, both will bind, as long as the computed binding point is not further away from the pilus start point than its free length $l_k^{(free)}$. In general, the resulting distance between the binding point and the start point will be smaller than the free lengths of the pili. The difference of the lengths, called the tail length $l_k^{(tail)}$, is saved as long as the pili are attached to each other. When both pili detach again, the tail length will be added back to the free length of the pilus, so that it will have a new length $l_k^{(free)} + l_k^{(tail)}$.

A.3 FORCES AND MOTILITY

A.3.1 *Excluded volume forces*

If the coccus j of a cell overlaps with the substrate with the distance Δd_{ov}, a volume exclusion force is generated. This force points in the normal direction of the substrate (here in the $z-$direction $\mathbf{e}_z$, see figure 2.1 and 2.2A) and is given by

$$\mathbf{F}_j^{(cs)} = k_{cs} \Delta d_{ov} \mathbf{e}_z, \tag{A.6}$$

where k_{cs} is the excluded volume spring constant. The force acts on the point where the coccus position is projected on top of the substrate (x and y component is the same as for the coccus position, the z-component is set to 0). For a high excluded volume constant k_{cs} this is valid, because the cell will only weakly intersect with the substrate.

If two cells i and j overlap, such that the distance of their cocci is smaller than the cocci diameter $2R$, a repulsive force is generated (see figure 2.2B), given by

$$\mathbf{F}_{ij}^{(cc)} = -k_{cc} \left(2R - |\mathbf{r}_{ij}|\right) \frac{\mathbf{r}_{ij}}{|\mathbf{r}_{ij}|}, \tag{A.7}$$

where $\mathbf{r}_{ij}$ is the vector point from the coccus of cell i to the coccus of cell j and k_{cc} is the excluded volume spring constant.

A.3.2 *Pili forces*

When a pilus k is bound to the substrate, it creates a force according to

$$\mathbf{F}_k^{(ps)} = \max\left[0, k_{pili}\left(l_k^{(cont)} - l_k^{(free)}\right)\right] \frac{\mathbf{r}_k^{(se)}}{|\mathbf{r}_k^{(se)}|} \tag{A.8}$$

with the pilus contour length $l_k^{(\mathrm{cont})}$, its free length $l_k^{(\mathrm{free})}$, the spring constant k_{pili} and $\mathbf{r}_k^{(\mathrm{se})} = \mathbf{r}_k^{(\mathrm{e})} - \mathbf{r}_k^{(\mathrm{s})}$ being the vector pointing from the pilus start point to its end point.

For a pilus k attached to another pilus j the force is given by

$$\mathbf{F}_k^{(\mathrm{pp})} = \max\left[0, k_{\mathrm{pili}}\left(l_k^{(\mathrm{cont})} - l_k^{(\mathrm{free})} - l_j^{(\mathrm{free})}\right)\right] \frac{\mathbf{r}_k^{(\mathrm{se})}}{|\mathbf{r}_k^{(\mathrm{se})}|}. \tag{A.9}$$

If two pili bind to each other, we set the end point of pilus k to the start point of pilus j. Then, $\mathbf{r}_k^{(\mathrm{se})}$ is the vector pointing from the start point of pilus k to the start point of pilus j and the contour length of the pilus k is the distance between these start points. Thus, the force is computed by subtracting the sum of the free lengths of the two pili $l_k^{(\mathrm{free})} + l_j^{(\mathrm{free})}$ from the contour length.

Here, it is important to highlight that the spring constant k_{pili} of the pilus does not depend on its length. This is a valid approximation, as long as the spring constant is large and only small displacements, relative to the average pili length, are encountered. The spring constant only affects the time a pilus needs to reach the stalling force, but does not affect the value of the force the pilus finally reaches. This simplification was introduced in order to increase the computational speed of the simulation, but creates a problem for short pili whose contour lengths $l_k^{(\mathrm{cont})}$ are no longer able to reach the stalling force. To mitigate this issue, pili having a contour length smaller than $l_k^{(\mathrm{cont})} < F_{\mathrm{stall}}/k_{\mathrm{pili}}$ always generate the stalling force in our simulation. This is motivated by the fact that short pili will have a very large spring constant. For large values of the spring constant the relaxation time of the force is small (see section D.1).

B

EXPERIMENTAL PROTOCOLS

The experiments were performed in the lab of Nicolas Biais (Brooklyn College, City University of New York) by Wolfram Pönisch, Khaled Alzurqa, Hadi Nasrollahi and Nicolas Biais. The protocols were taken from [124].

B.1 BACTERIA STRAINS AND GROWTH CONDITIONS

The wild-type (WT) strain used in this study is MS11. The ΔpilT mutant was obtained by an inframe allelic replacement of the pilT gene by a Kanamycin resistance cassette. Fluorescent proteins (YFP, mCherry or tdTomato) driven by a consensus promoter were incorporated by allelic replacement together with an antibiotic marker (either Kanamycin or Chloramphenicol). Similarly mCherry driven by the reporter of the pilin gene (370 bp before the beginning of the starting ATG of the pilin ORF) was incorporated by allelic replacement together with a Chloramphenicol maker. Bacteria were grown on GCB-medium base agar plates supplemented with Kellog's supplements at 37°C and 5 % CO_2. 80 μg/ml of Kanamycin or 7 μg/ml of Chloramphenicol were added when growing mutants with the corresponding antibiotic resistance cassette. Cells were streaked from frozen stock allowed to grow for 24 hours and then lawned onto identical agar plates and used after a 16 to 20 hour growth period.

B.2 COLONY FORMATION

Bacteria from lawns on agar plates were resuspended in 1 ml of GCB medium at an optical density of OD = 0.7. 100μl of the suspension was added in the well of the 6 well plate containing 2 ml of GCB medium with a BSA coated coverglass (round 25 mm diameter coverglasses (CS-25R) Warner Instruments) at the bottom or without. The 6 well plate was centrifuged at 1600xg in a swinging bucket in an 5810R centrifuge (Eppendorf) for 5 minutes resulting in single bacteria uniformly coating the bottom of the well. For direct imaging the coverglass were transferred to an observation chamber (attofluor cell chamber, Thermo Fisher Scientific). In the case of mixture the suspension at OD = 0.7 of both components of the mixture were prepared and a new 1 ml was prepared by the proper ratio of the two suspension. 100 μl of that new suspension was used similarly to what was described previously.

B.3 MICROSCOPY AND COALESCENCE EXPERIMENTS

All movies were obtained on a Nikon Ti Eclipse inverted microscope equipped for epifluorescence and DIC microscopy and with an optical tweezers setup all under an environmental chamber maintaining temperature, humidity and C. The objective used is a 60X plan Apo objective. The camera used were either a sCMOS camera (Neo, Andor) or a CMOS USB camera (DCC1240M, Thorlabs). 1Hz fluorescent movies and 0.1Hz DIC movies of either microcolony merger or follow up of single cell motility were taken for further analysis. In the case of microcolony merger, microcolonies were preformed and were brought into contact either by optical tweezers or hydrodynamical flow.

C

GEOMETRIC ESTIMATION OF THE PARAMETERS OF THE STOCHASTIC MODEL OF CELL MOTION ON A SUBSTRATE

By considering geometric features of a spherical cell and the known dynamics of type IV pili system we can estimate the values of the parameters of the stochastic model. In particular, we estimate the attachment rate γ_{att} and the average pili length, projected on the substrate L.

C.1 RATIO OF ATTACHING PILI

The geometry of the cell is illustrated in figure C.1a. In this model we assume that cells can be described by spheres with radius R. The z-position of the cell center is chosen to be the same as the radius R. Thus, the cell is only able to move in the $x-y-$plane. For now, the pili are modeled as lines with length l protruding perpendicular from the surface of the spherical cell. The position from which a pilus emerges can be defined by an angle θ, assuming that we have a rotational symmetry around the z-axis. Later, we will only consider those pili that are able to attach to the surface, which is true for $\theta \in \left(\frac{\pi}{2}, \pi\right]$. The pili have an exponential length distribution given by

$$p_c(l) = \frac{1}{l_c} \exp\left(-\frac{l}{l_c}\right) \tag{C.1}$$

with a characteristic pili length l_c [27]. A pilus can attach to the substrate, if its length is larger than its minimal length

$$l_{min} = -\frac{R}{\cos\theta} - R. \tag{C.2}$$

which corresponds to the length of the line between the pilus start point and the intersection point with the $x-y-$axis for $z = 0$ (see figure C.1).

The ratio of all pili longer than this length determines the fraction of pili that are long enough to bind to the surface stochastically with a rate γ_{att}. The probability density function of the time of attachment is then given by

$$p_{att}(t) = \gamma_{att} \exp\left(-t\gamma_{att}\right) \tag{C.3}$$

with the time t. A pilus, thats length l results from the probability density function $p_c(l)$, protrudes until it reaches the minimal pili length l_{min}, intersects with the substrate and continues its protrusion for the length $l - l_{min}$. Then it starts to retract over the same distance as the protrusion. Thus, the pilus tip, which is responsible for the binding to the substrate, can bind to the substrate along the length $l - l_{min}$

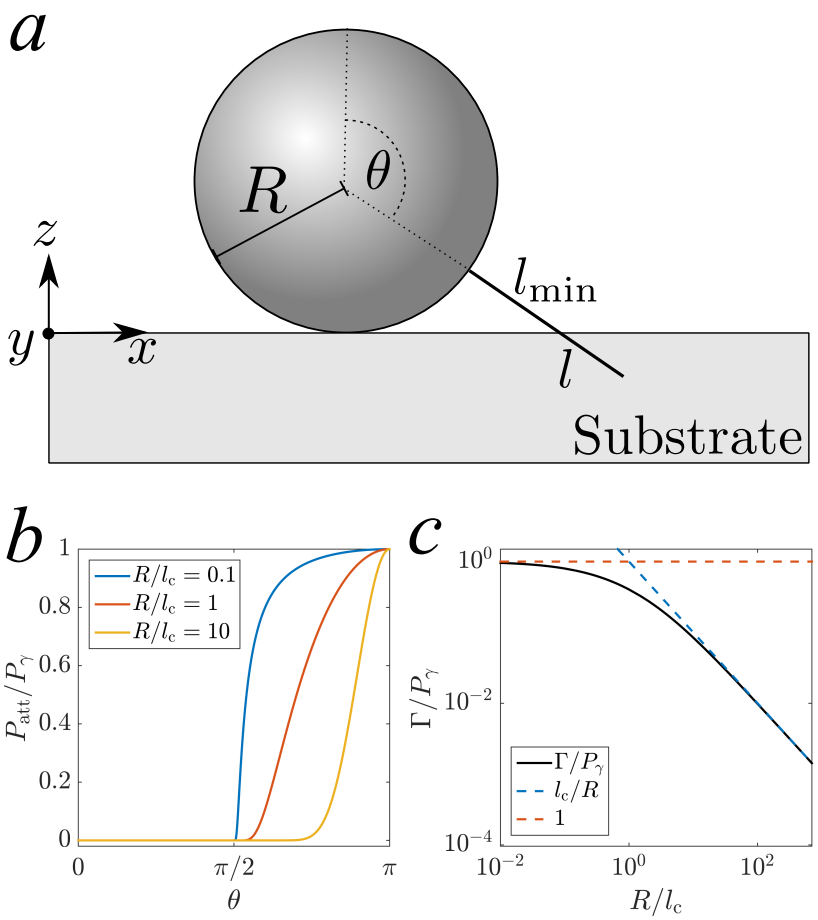

Figure C.1: (a) Geometry of the system. The pili protrude perpendicular from the surface of a spherical cell of radius R. The point from where a pilus emerges is defined by an angle θ. Pili that reach a length l larger than the minimal length l_{min} are able to intersect with the substrate and can bind to it. (b) Attachment probability $P_{att,\theta}$ of pili emerging from the surface of a sphere (see equation C.5). (c) Ratio of attached pili Γ as a function of the cell radius R (see equation C.6) and scalings for large and small cell radii R.

for the protrusion and along the same length for the retraction. The protrusion and retraction speed have the same value v_0. This is motivated by experimental measurements that show that the values of both speeds are in the same order of magnitude [23]. The full process of protrusion and retraction takes the time $2(l - l_{min})/v_0$, where the 2 results from the cycle of protrusion and retraction. The attachment probability of the pilus tip during this time is given by

$$\begin{aligned} P_{att,min} &= \int_0^{2(l-l_{min})/v} dt\ p_{att}(t) \\ &= 1 - \exp\left[-2\left(l - l_{min}\right)/l_{att}\right], \end{aligned} \tag{C.4}$$

where we define the length scale of attachment $l_{att} = v_0 / \gamma_{att}$. Considering this effect, we can compute the attachment probability $P_{att,\theta}$ of a pilus emerging from the cell surface from a point defined by the angle θ. Therefore, we include its length distribution p_c, so that

$$\begin{aligned} P_{att,\theta} &= \int_{l_{min}}^{\infty} dl\ p_c\left(l\right) P_{att,min}\left(l\right) \\ &= P_\gamma \exp\left[\frac{R}{l_c}\left(1 + \frac{1}{\cos\theta}\right)\right] \end{aligned} \tag{C.5}$$

with the prefactor $P_\gamma = 2l_c\gamma_{att}/\left(v_0 + 2l_c\gamma_{att}\right)$. For pili that do not point towards the substrate, the attachment probability is 0, corresponding to $P_{att,\theta}(\theta \leqslant \pi/2) = 0$. The probability $P_{att,\theta}$ is shown in figure C.1b. We assume that the ratio of attached pili, given in equation C.5, is equivalent to a density on the surface of a spherical cell with radius R. From this equation we want to compute the total number of pili that intersect with the substrate and bind to it. The total number of attached pili is given by an integration of this density over the surface of the spherical cell (and by considering the pili surface density ρ_p), so that

$$\begin{aligned} N_{att} &= \rho_p \int_A dA\ P_{att,\theta} \\ &= N_{pili} P_\gamma \left[1 + \frac{R}{l_c}\exp\left(\frac{R}{l_c}\right) \mathrm{Ei}\ \left(-\frac{R}{l_c}\right)\right] \end{aligned} \tag{C.6}$$

with the exponential integral function, defined as

$$\mathrm{Ei}\left(x\right) = -\int_{-x}^{\infty} dt\ \frac{\exp\left(-t\right)}{t}, \tag{C.7}$$

and the total number of pili of the lower half sphere of the cell, given by

$$N_{pili} = 2\pi\rho_p R^2. \tag{C.8}$$

Furthermore, we can rewrite $P_\gamma = 2l_c/(2l_c + l_{att})$ with the characteristic length l_{att} of the Poisson process characterizing the attachment to the substrate.

The fraction of attached pili is now given by

$$\Gamma = \frac{N_{att}}{N_{pili}} = P_\gamma \left[1 + \frac{R}{l_c}\exp\left(\frac{R}{l_c}\right) \mathrm{Ei}\ \left(-\frac{R}{l_c}\right)\right]. \tag{C.9}$$

For small cell radii it converges towards

$$\Gamma(R \ll 1) = P_\gamma, \tag{C.10}$$

and for large cell radii it exhibits a scaling

$$\Gamma(R \gg 1) = P_\gamma \frac{l_c}{R}. \tag{C.11}$$

We can give a simple argument why the ratio is decreasing with R^{-1} for large cells. The total number of pili is proportional to the cell surface, thus it follows $\propto R^2$. For large cells we can assume that only those pili will attach to the substrate, for which the distance of the start point is not larger than a constant value h. The surface area of the spherical cap of a sphere with radius R and a cap height h is given by $2\pi Rh$, thus it is proportional to R. By dividing the surface area of the cap by the surface area of the sphere, we get a ratio that is proportional to R^{-1}. For very small cells, the radius R is comparable to h, thus all pili (at least of the lower half sphere) can attach to the substrate and both areas are then proportional to R^2, making the ratio constant.

C.2 EFFECTIVE PILI ATTACHMENT RATE

As computed in the last subsection, the ratio Γ defines the probability that a pilus, emerging from the surface of a spherical cell, will attach to the substrate. In order to attach to the substrate, it first needs to grow for a time t_{min} until it reaches the length l_{min} (see equation C.2). When it reaches the surface, it will bind to the surface with a time resulting from the binding rate γ_{att}. We assume that on average a pilus will only attach ones to the substrate. In order to be able to attach to the substrate, a pilus, protruding with the velocity v_0, must reach a length l_{min} before it is long enough to hit the substrate (see equation C.2) and would be able to attach to it. This corresponds to a time $t_{min} = l_{min}/v_0$. Thus, the attachment rate of a pilus, emerging from a point defined by the angle θ (see figure C.1) is then given by

$$\gamma_\theta = \frac{1}{t_{min}(\theta) + t_{att}} = \frac{v_0}{l_{min}(\theta) + l_{att}} \tag{C.12}$$

Here, l_{min} was defined in equation C.2 and the characteristic attachment length is given by $l_{att} = v_0 t_{att} = v_0/\gamma_{att}$. By integrating over the spherical shape of the cell, we can compute the mean attachment rate of all pili, given by

$$\begin{aligned}\langle\gamma_\theta\rangle_{Sphere} &= \frac{\int dA\, \gamma_\theta}{\int dA} \\ &= v_0 \frac{l_{att} - R\left[1 + \ln\left(\frac{l_{att}}{R}\right)\right]}{(l_{att} - R)^2}.\end{aligned} \tag{C.13}$$

If we now consider the fact that pili only attach to a substrate with a probability Γ and in every other case will only protrude and retract, but not attach, we get the effective rate

$$\gamma_{eff} = \Gamma\langle\gamma_\theta\rangle_{Sphere}. \tag{C.14}$$

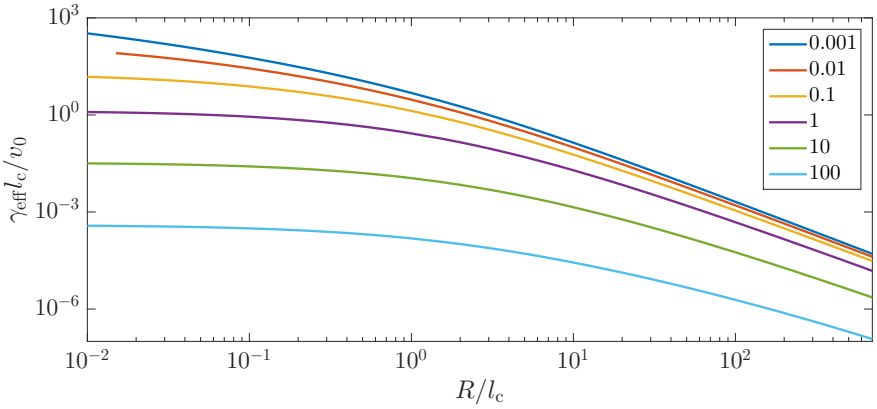

Figure C.2: Effective pili attachment rate cells of different sizes R and different attachment lengths l_{att}/l_c.

The behavior of the effective rate as a function of the cell size is shown in figure C.2.

C.3 LENGTH SCALE OF THE DISTANCE OF PILI START AND ATTACHMENT POINT

In the following we calculate the mean displacement a pilus, protruding from a spherical cell sitting on top of a surface, can mediate. This displacement corresponds to the distance between the attachment point of a pilus emerging from the surface of a cell of radius R and its anchor point at the cell surface, defined by the angle θ, projected onto the substrate. As depicted in figure C.3, we consider two cases: (i) pili emerging perpendicular from the cell surface and possessing a infinite pivotal stiffness, thus bending when they hit the surface, and (ii) sliding of a stiff pilus along the surface with a vanishing pivotal stiffness at the anchoring point.

Infinite pivotal stiffness of pili

In the first case we assume that a pilus possesses an infinite pivotal stiffness. Thus, it will always protrude from the cell with the same angle as given by the surface angle θ (see figure C.3a). When the pilus hits the surface, it bends and moves parallel to it. In this case, there are two distinct lengths that contribute to the distribution of attachment points on the surface (see figure C.3):

- The horizontal distance between the start point of the pilus and the intersection point between the pilus protruding perpendicular from the cell membrane and the substrate. This distance is given by

$$d_1(R, \theta) = -R \tan\theta - R \sin\theta. \tag{C.15}$$

- The second contribution d_2 results from the motion of the pilus end tip over the substrate until it starts to retract. At the same

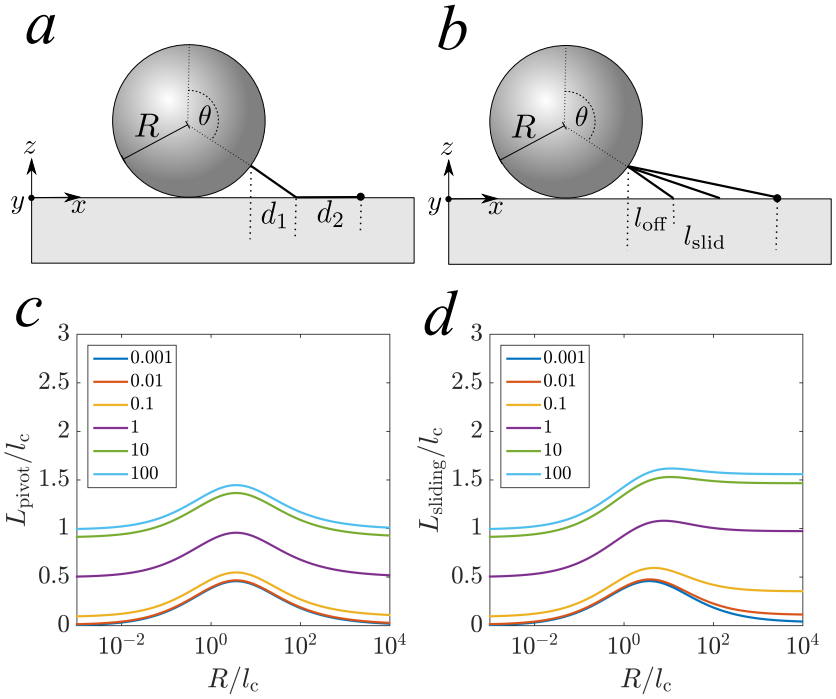

Figure C.3: Estimating the mean displacement mediated by pili to a cell moving over a substrate. (a) Geometry of the pilus binding model with infinite pivotal stiffness of the pilus emerging perpendicular from the surface of the cell. When a pilus is longer than the minimal length l_{min} it hits the surface and, due to the high pivotal stiffness, bends and moves parallel to the surface. (b) Geometry of the pilus binding model with pili sliding along the substrate. Here, we neglect the pivotal stiffness of the pili. Due to the sliding, they do not necessarily to protrude perpendicularly from the cell surface. (c) Cell size-dependence of the mean value of the displacement L_{pivot} for an infinite pivotal stiffness of pili growing from the cell surface for different values of l_{att}/l_c. (d) Cell size-dependence of the mean value of the distance $L_{sliding}$ for different values of l_{att}/l_c.

time it will bind to the substrate with the rate γ_{att}. Both processes are modeled as Poisson processes, that are characterized by the pilus tip, starting at the point $x = 0$ and moving with a constant velocity v_0. After the pilus reaches a length given by the exponential length distribution (see equation C.1) it retracts, switching its direction of motion until it reaches its start point again. During this protrusion and retraction, it is able to attach to the substrate as given in equation C.3.

In order to estimate the mean distance of this attachment point from its starting point, we first assume that we have a point wandering to the position $x = L$ and turning its direction of motion at this point. The probability density function $p_L(x)$ to find the tip of a pilus performing the forward and backward motion over the length L and binding to the point at the position x is given by

$$p_L(x) = \frac{\left[\exp\left(-\frac{x}{l_{att}}\right) + \exp\left(-\frac{2L-x}{l_{att}}\right)\right]}{l_{att} - l_{att}\exp\left(-\frac{2L}{l_{att}}\right)}, \tag{C.16}$$

where we define the characteristic attachment length $l_{att} = v_0/\gamma_{att}$. Due to the stochastic binding of the pilus tip with the attachment length l_{att}, not all pili will bind. The probability of a pilus to attach to the surface is given by

$$P_L = \int_0^{2L/v_0} dt\, p_{att} = 1 - \exp\left(-\frac{2L}{l_{att}}\right). \tag{C.17}$$

In the next step, we consider the exponential length distribution of the pili, instead of a fixed length L. The underlying probability density function is the pili length distribution p_c (see equation C.1), multiplied with the probability of attachment to the surface for a given length, P_L. We use this probability density function in order to compute the mean probability density function of the binding point distribution p_L, so that we get

$$p_2(x) = \frac{\int_L^\infty dL\, P_L(L) p_L(x, L) p_c(L)}{\int_0^\infty dL\, P_L(L) p_c(L)} = \frac{1}{l_{att,c}} \exp\left(-\frac{x}{l_{att,c}}\right) \tag{C.18}$$

where p_2 is the probability density function characterizing the distribution of the second length scale d_2 (see figure C.3a) and defining where a pilus tip exhibiting a cycle of protrusion and retraction and moving with a constant velocity v_0 over the surface will bind. Here we define

$$l_{att,c} = \frac{1}{1 + \frac{l_c}{l_{att}}} l_c. \tag{C.19}$$

In order to compute the probability density function of the attachment points for a given angle θ, defining from which point on the surface

of the cell a pilus emerges from, we need to combine $p_2(d_2)$ and d_1, so that we get

$$p_{1,2}(x,\theta) = \begin{cases} 0 & x < d_1(R,\theta) \\ p_2(x - d_1(R,\theta)) & x \geqslant d_1(R,\theta) \end{cases}. \tag{C.20}$$

Here, $x - d_1$ results from the fact that every pilus that attaches to the surface first needs to be longer than l_{min} (see equation C.2) and thus contributes a initial displacement, given by d_1. The mean distance is given by

$$\langle x \rangle_{p_{1,2}} = d_1(R,\theta) + l_{att,c} \tag{C.21}$$

where the mean is computed corresponding to the distribution $p_{1,2}$.

We compute the mean distance by taking $\langle x(\theta) \rangle_{p_{1,2}}$ and averaging this value over the cell surface. Therefore, we need to consider the probability of pili to attach to the surface $P_{att,\theta}$ for a given angle θ, as given in equation C.5 and integrate over the surface of the spherical cell. This is given by

$$L_{pivot} = \frac{\int dA\ \langle x \rangle_{p_{1,2}} P_{att,\theta}(\theta)}{\int dA\ P_{att,\theta}(\theta)} = \frac{\int dA\ d_1(R,\theta) P_{att,\theta}(\theta)}{\int dA\ P_{att,\theta}(\theta)} + l_{att,c} \tag{C.22}$$

and solved numerically (see figure C.3c). The first term is a result of the geometry of the cell, the second term is a result of the stochastic binding of the pilus tip.

Sliding of the pilus tip along the substrate

In the case of sliding the pilus possesses a negligible pivotal stiffness while protruding from the surface of the cell, but an infinitely large bending stiffness (see figure C.3b). The projected distance between the start point and the end point of a pilus is then given by

$$l_{slid} = \sqrt{(l_{min} + l)^2 - h^2} \tag{C.23}$$

with l_{min} being the minimal distance the pilus needs to reach the surface (see equation C.2). Here, $l > l_{min}$ and the height of the start point is given by

$$h = R + R\cos\theta, \tag{C.24}$$

where the angle θ defines from which point on the cell surface the pilus is emerging from.

We define a weight function from the probability distribution of the attachment points (see equation C.3) and multiply it by the probability for pili emerging from a point, defined by the radius R and the angle θ (see equation C.5). Then, we integrate over the surface of the cell S:

$$L_{sliding}(R) = \frac{\int dS\ \int_{l_{min}(R,\theta)}^{\infty} dl'\ l_{slid}(R,l',\theta) p_{1,2}(R,l',\theta) P_{att,\theta}(R,\theta)}{\int dS\ \int_0^{\infty} dl'\ p_{1,2}(R,l',\theta) P_{att,\theta}(R,\theta)}. \tag{C.25}$$

Equation C.25 has been solved numerically, with results depicted in figure C.3d.

D

SOLUTIONS FOR SIMPLIFIED MODELS OF PILI-MEDIATED CELL MOTION

D.1 PILI FORCES IN A SIMPLIFIED ONE-DIMENSIONAL SYSTEM

In this chapter we want to study a simplified one-dimensional system in order to learn about how pili build up a pulling force and how these forces are translated into the motion of the corresponding cell/microcolony.

In the system we want to study (see figure D.1), a cell possesses N_l pili on its left side and N_r pili on its right side. These pili are modeled as Hookean springs with a spring constant k_{pili} and have a contour length L_l and L_r, giving the length between the anchor point of the pilus (the point where it is attached to the cell) and its attachment point at the left or right side, for example to walls. If the same pilus would not be attached to the wall, its length, defined by l_l or l_r, could be different from the contour length. The force such a pilus produces is given by

$$F_l = k_{pili}\,(L_l - l_l)\,, \tag{D.1}$$

$$F_r = k_{pili}\,(L_r - l_r)\,. \tag{D.2}$$

The total force acting on the cell is then given by

$$F_{tot} = -N_l F_l + N_r F_r. \tag{D.3}$$

Here, we assume that k_{pili} is not dependent on the length of the pili. In such a one-dimensional system we define the position x_c of a cell by the length of the pili, such that

$$\dot{L}_l = \dot{x}_c, \tag{D.4}$$

$$\dot{L}_r = -\dot{x}_c. \tag{D.5}$$

Additionally, we can also express the velocity of the cell by considering the translational mobility μ_{trans}:

$$\dot{x}_c = \mu_{trans} F_{tot}. \tag{D.6}$$

By considering the stalling of pili, we define the force-dependence of the free length of pili (see equation 2.3):

$$\dot{l}_l = -\max\left[0,\ v_{ret}\left(1 - \frac{F_l}{F_{stall}}\right)\right], \tag{D.7}$$

$$\dot{l}_r = -\max\left[0,\ v_{ret}\left(1 - \frac{F_r}{F_{stall}}\right)\right], \tag{D.8}$$

with the retraction velocity v_{ret} and the stalling force F_{stall}. By combining all these equations, we can write

$$\begin{aligned}\dot{F}_l = &-k_{pili}\mu_{trans}N_l F_l + k_{pili}\mu_{trans}N_r F_r \\ &+ k_{pili}v_{ret}\max\left[0,\ 1 - \frac{F_l}{F_{stall}}\right]\end{aligned} \tag{D.9}$$

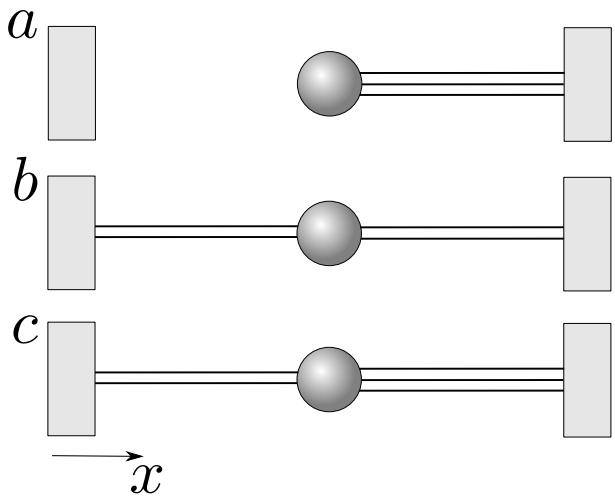

Figure D.1: Estimating the time-dependent force of pili in a simplified one-dimensional system. (a) Pili are only attached to one side. (b) The same number of pili is attached on both sides. (c) Different number of pili attached on both sides.

and

$$\dot{F}_r = k_{pili}\mu_{trans}N_lF_l - k_{pili}\mu_{trans}N_rF_r + k_{pili}\nu_{ret}\max\left[0,\ 1-\frac{F_r}{F_{stall}}\right]. \tag{D.10}$$

Together with the initial conditions

$$F_l(0) = 0, \tag{D.11}$$

$$F_r(0) = 0 \tag{D.12}$$

we solve this system of ordinary differential equations in the following subsections.

We assume that the length of the pilus is very long, such that we can neglect cases in which it would reach a free length $l_l < 0$ or $l_r < 0$.

D.1.1 *Pili only attached to one side*

Here, we assume that pili are only attached to the right side (see figure D.1a), so that we have to solve the ordinary differential equation

$$\dot{F}_r = -k_{pili}\mu_{trans}N_rF_r + k_{pili}\nu_{ret}\left(1-\frac{F_r}{F_{stall}}\right),$$

with $F_r(0) = 0$. The solution is given by

$$F_r = F_{single}\left[1-\exp\left(-\frac{t}{\tau_{single}}\right)\right], \tag{D.13}$$

where

$$F_{single} = \frac{F_{stall}}{1+\frac{F_{stall}\mu_{trans}N_r}{\nu_{ret}}}, \tag{D.14}$$

$$\tau_{single} = \frac{F_{stall}}{k_{pili}\left(F_{stall}N_r\mu_{trans}+\nu_{ret}\right)}. \tag{D.15}$$

The velocity of the cell is then given by

$$v = \mu_{trans} N_r F_r = v_{single} \left[1 - \exp\left(-\frac{t}{\tau_{single}} \right) \right], \tag{D.16}$$

with

$$v_{single} = \frac{v_{ret}}{1 + \frac{v_{ret}}{F_{stall} N_r \mu_{trans}}}. \tag{D.17}$$

The force F_{single} fulfills $0 \leqslant F_{single} < F_{stall}$ and the cell velocity v_{single} fulfills $0 \leqslant v_{single} < v_{ret}$ for a finite number of attached pili on one side of the cell.

D.1.2 *Similar number of pili on both sides*

In the case of equal number of pili on both sides (see figure D.1b), the forces on both sides are equal $F_l = F_r$ and the ordinary differential equations have the form

$$\dot{F}_l = k_{pili} v_{ret} \max\left[0,\ 1 - \frac{F_l}{F_{stall}} \right], \tag{D.18}$$

$$\dot{F}_r = k_{pili} v_{ret} \max\left[0,\ 1 - \frac{F_r}{F_{stall}} \right]. \tag{D.19}$$

Then, the forces behave as

$$F_l = F_r = F_{stall} \left[1 - \exp\left(-\frac{t}{\tau_{equal}} \right) \right], \tag{D.20}$$

where

$$\tau_{equal} = \frac{F_{stall}}{k_{pili} v_{ret}}. \tag{D.21}$$

It is important to note that the forces are no longer dependent on the number of pili. Additionally, the velocity of the cell is $v = 0$.

D.1.3 *Different number of pili on both sides*

For an unequal case of pili binding on both sides of the cell (see figure D.1c), we need to solve the equations D.9 and D.10. Here, we assume that $N_l < N_r$. In this case, the pili on the left side will reach a force that will be larger than the stalling force and will no longer be able to reduce their free pili length l_l.

Initially the pili follow the set of ordinary differential equations

$$\dot{F}_l = k_{pili} \left[\mu_{trans} \left(-N_l F_l + N_r F_r \right) + v_{ret} \left(1 - \frac{F_l}{F_{stall}} \right) \right] \tag{D.22}$$

and

$$\dot{F}_r = k_{pili} \left[\mu_{trans} \left(N_l F_l - N_r F_r \right) + v_{ret} \left(1 - \frac{F_r}{F_{stall}} \right) \right]. \tag{D.23}$$

The solution is

$$F_l(t) = F_{l,o} - F_{l,1} \exp\left(-\frac{t}{\tau_1}\right) - F_2 \exp\left(-\frac{t}{\tau_2}\right), \tag{D.24}$$

$$F_r(t) = F_{r,o} - F_{r,1} \exp\left(-\frac{t}{\tau_1}\right) - F_2 \exp\left(-\frac{t}{\tau_2}\right) \tag{D.25}$$

with

$$F_{l,o} = \frac{F_{stall}\left(2F_{stall}N_r\mu_{trans} + v_{ret}\right)}{F_{stall}\left(N_l + N_r\right)\mu_{trans} + v_{ret}}, \tag{D.26}$$

$$F_{l,1} = \frac{2F_{stall}N_r}{N_l + N_r}, \tag{D.27}$$

$$F_2 = \frac{F_{stall}\left(N_l - N_r\right)v_{ret}}{\left(N_l + N_r\right)\left[F_{stall}\left(N_l + N_r\right)\mu_{trans} + v_{ret}\right]}, \tag{D.28}$$

$$F_{r,o} = \frac{F_{stall}\left(2F_{stall}N_l\mu_{trans} + v_{ret}\right)}{F_{stall}\left(N_l + N_r\right)\mu_{trans} + v_{ret}}, \tag{D.29}$$

$$F_{r,1} = \frac{2F_{stall}N_l}{N_l + N_r}, \tag{D.30}$$

$$\tau_1 = \frac{F_{stall}}{k_{pili}v_{ret}}, \tag{D.31}$$

$$\tau_2 = \frac{F_{stall}}{k_{pili}\left[F_{stall}\left(N_l + N_r\right)\mu_{trans} + v_{ret}\right]}. \tag{D.32}$$

Here, τ_1 corresponds to the time scale observed for the motion of a cell if the same number of pili are attached on both sides. The time τ_2 corresponds to the time for the case that all pili are only attached on one side. Then, the velocity of the cell is given by

$$\begin{aligned} v(t) &= \mu_{trans}(-N_lF_l + N_rF_r) \\ &= v_0\left[1 - \exp\left(-\frac{t}{\tau_2}\right)\right], \end{aligned} \tag{D.33}$$

with

$$v_0 = \frac{F_{stall}\left(N_r - N_l\right)\mu_{trans}v_{ret}}{F_{stall}\left(N_l + N_r\right)\mu_{trans} + v_{ret}}. \tag{D.34}$$

These equations are correct until the first pili, for $N_l < N_r$ the pili on the left side, reach the stalling force F_{stall} at the time t_{stall}. This time needs to be computed numerically. Then, the ordinary differential equations have the form

$$\dot{F}_l = k_{pili}\mu_{trans}\left(-N_lF_l + N_rF_r\right) \tag{D.35}$$

and

$$\dot{F}_r = k_{pili}\left[\mu_{trans}\left(N_lF_l - N_rF_r\right) + v_{ret}\left(1 - \frac{F_r}{F_{stall}}\right)\right], \tag{D.36}$$

and the initial conditions

$$F_l(t_{stall}) = F_{stall}, \tag{D.37}$$

$$F_r(t_{stall}) = F_{right,trans}. \tag{D.38}$$

Here, $F_{right,trans}$ needs to be computed numerically from equation D.23. Again, the solution has a form

$$F_l(t) = F_{l,3} - F_{l,4}\exp\left(-\frac{t-t_{stall}}{\tau_4}\right) - F_{l,5}\exp\left(-\frac{t-t_{stall}}{\tau_5}\right), \tag{D.39}$$

$$F_r(t) = F_{r,3} - F_{r,4}\exp\left(-\frac{t-t_{stall}}{\tau_4}\right) - F_{r,5}\exp\left(-\frac{t-t_{stall}}{\tau_5}\right), \tag{D.40}$$

with

$$F_{l,3} = \frac{N_r}{N_l}F_{stall}, \tag{D.41}$$

$$F_{r,3} = F_{stall}, \tag{D.42}$$

$$\tau_4 = \frac{2F_{stall}}{k_{pili}\left[F_{stall}\left(N_l+N_r\right)\mu_{trans}+\nu_{ret}-\nu_t\right]}, \tag{D.43}$$

$$\tau_5 = \frac{2F_{stall}}{k_{pili}\left[F_{stall}\left(N_l+N_r\right)\mu_{trans}+\nu_{ret}+\nu_t\right]}, \tag{D.44}$$

and where

$$\nu_t = \sqrt{\left[F_{stall}\left(N_l+N_r\right)\mu_{trans}+\nu_{ret}\right]^2 - 4F_{stall}N_l\mu_{trans}\nu_{ret}}. \tag{D.45}$$

Again, we compute the resulting velocity of the cell by

$$\begin{aligned}\nu(t) &= \mu_{trans}(-N_lF_l + N_rF_r)\\ &= \nu_4\exp\left(-\frac{t-t_{stall}}{\tau_4}\right) + \nu_5\exp\left(-\frac{t-t_{stall}}{\tau_5}\right).\end{aligned} \tag{D.46}$$

We will not give the analytical expression for $F_{l,4}$, $F_{l,5}$, $F_{r,4}$, $F_{r,5}$, ν_4 and ν_5 due to their long form. Where it is used, the exact expression is taken for further calculations.

D.2 CELL VELOCITY IN A SIMPLIFIED TWO-DIMENSIONAL MODEL

In the previous chapter we have shown that a cell, having pili attached at one particular side in a one-dimensional system, will be never able to move with velocities faster than the pilus retraction velocity ν_{ret} (see equation D.16 and equation D.17). Here, we want to show that in a two-dimensional system, this is not necessarily the case and a cell can move with velocities that are considerably higher.

Because we only want to show that such velocities can emerge in a two-dimensional system and do not want to focus on the exact values of these velocities, we will not present analytical calculations to get the expression of the velocities, but instead we point out the governing equations and present their numerical solution.

Here, we assume that a cell possesses two pili that are attached to a substrate such that initially the angle between them has a value of 90°. At the beginning, the contour length l_{cont} of the pili and their free length l_{free} (the length a pilus would have in equilibrium if it is

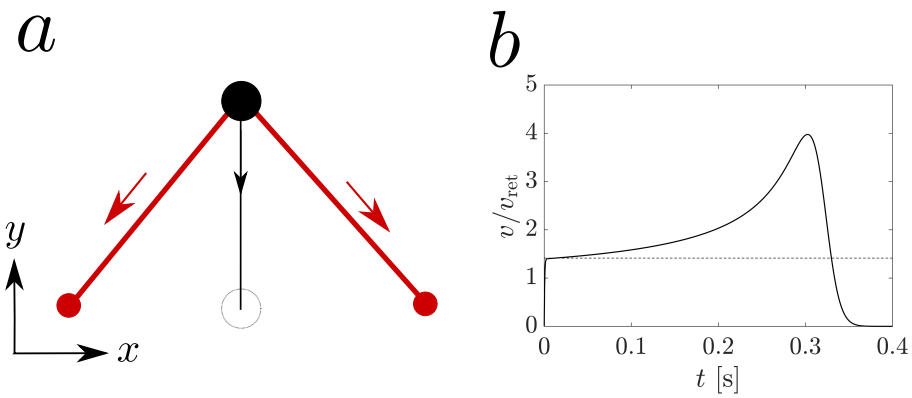

Figure D.2: Estimating the cell velocity in a simplified two-dimensional system. (a) Geometry of the simple two-dimensional model studied to show that pili-mediated motility can generate cell velocities considerably faster than the pilus retraction velocity. The black dot represents the cell, the red lines are the pili thats attachment points are given by the red dots. The cell will move until it reaches the position between the two pilus attachment points, highlighted by the dotted circle. (b) Ratio of the cell velocity v and the pilus retraction velocity v_{ret} as a function of time for the two-dimensional model (solid line). The dotted line represents $\sqrt{2}v_{ret}$, the absolute velocity of a particle moving with v_{ret} in x- and y-direction. Here, we picked $L = 2\ \mu m$, $v_{ret} = 2\ \mu m/s$, $F_{stall} = 180\ pN$, $k = 2000\ pN/\mu m$ and $\mu_{trans} = 1\ \mu m/(pN\ s)$.

not attached to the substrate) is given by L. Then, both pili start to retract with the velocity v_{pili}, where the pilus velocity v_{pili} depends on its force F by

$$v_{pili} = \frac{dl_{free}}{dt} = -\max\left[0,\ v_{ret}\left(1 - \frac{F}{F_{stall}}\right)\right], \tag{D.47}$$

with the stalling force F_{stall} (see equation 2.3). Additionally, we assume that the pili are Hookean springs with a spring constant k_{pili}. Then, the pilus force is given by

$$F = k_{pili}\left(l_{cont} - l_{free}\right), \tag{D.48}$$

pointing in the direction of the pilus attachment point emerging from the surface of the cell. The resulting force of the cell $F_{tot,y}$, pointing due to the symmetry of the system (as shown in figure D.2a) in the y-direction and being the sum of the y-components of the pilus forces is then affecting the motion of the cell in the overdamped regime,

$$v = \mu_{trans} F_{tot,y}, \tag{D.49}$$

with the translational mobility μ_{trans}. If we solve this system numerically, we observe cell velocities v that have values that are considerably higher than the pilus retraction velocity v_{ret} (see figure D.2b). This velocity can be also higher than $\sqrt{2}v_{ret}$, which is the absolute velocity of a cell moving with v_{ret} in the x- and the y-direction.

When we observe the trajectory of the cell we see that it moves from its start point to the point where it is right in between the two

pilus attachment points (see figure D.2a). Along this trajectory, the cell follows a velocity profile that is shown in figure D.2b. As one can see, it clearly reaches velocities that are up to four times higher than the pilus retraction velocity v_{ret}. This behavior originates from geometric effects where only a short retraction of the pili can correspond to a large displacement of the cell. Finally, the cell velocity converges towards $v = 0$, corresponding to the point where the cell is trapped between the two pili attachment points.

E

IMAGE ANALYSIS OF EXPERIMENTAL DATA

E.1 EDGE DETECTION OF MICROCOLONIES

In order to detect the edges of single colonies and the merger from DIC data the same algorithm was used (see figure E.1). Initially, we computed the first derivatives of intensities in x- and y-direction of a Gaussian filtered image (see figure E.1B), computed its absolute value and thresholded the value (see figure E.1C). Afterwards, we dilated and eroded the binary image, filled all remaining holes and removed small objects (see figure E.1D and E.1E). For all steps internal functions of Matlab were used.

E.2 BRIDGE HEIGHT AND AXIS RATIO OF COALESCING MICROCOLONIES

We analyzed 28 DIC movies of coalescing microcolonies in total that were provided by Nicolas Biais (Brooklyn College, City University of New York).

In order to fit an ellipse to two coalescing colonies, their binary shape was computed as described in appendix E.1. In order to compute the binary shape of the colonies, we computed the central moments of the binary image (see [141]), what allowed us to estimate the orientation of the colonies, the size of its long and short axis, and the ratio of them.

In order to compute the height of the bridge that forms between coalescing colonies, we rotated the binary image such that the colonies were oriented along the x-axis and calculated the COM of the

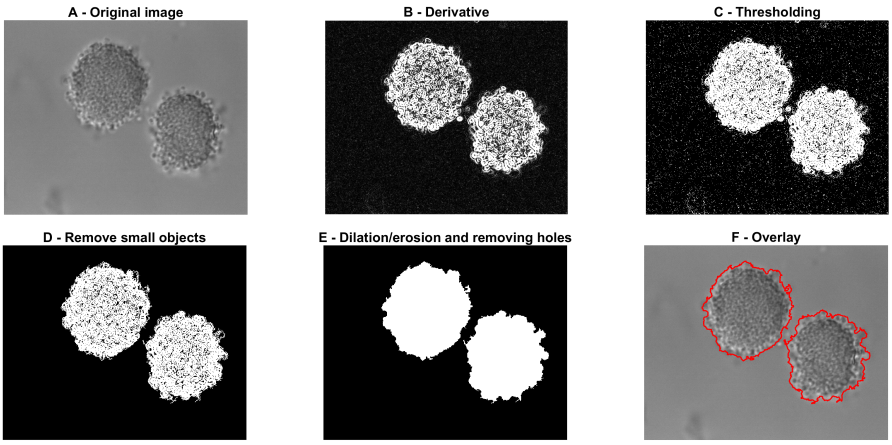

Figure E.1: Steps of the algorithm used to extract the edges of colonies from DIC images.

combined regions. Afterwards, we moved a line of length L centered around the center such that it moved perpendicular to the axis connecting the two colonies. The bridge was defined as the range for which the whole line could be found inside of the colony region. L was chosen to be small enough to be not affected by the elliptical shape of the colonies. For the late coalescence the results were compared to the short axis of the ellipse and exhibits qualitative agreement.

E.3 DETECTION OF INDIVIDUAL CELLS WITHIN MICROCOLONIES

We analyzed 40 individual colonies in total and tracked the cells within them.

In order to track single cells from the fluorescence images, we first computed the center of the binary shape computed from the DIC images of the microcolonies (see appendix E.1). These data had a recording frequency of 0.1 Hz. In order to know the position for all images of the fluorescence channel, that were recorded with a frequency of 1 Hz, we performed a cubic spline data interpolation on the x- and y-component on the colony center. This way, we could correct the centers of the colonies in the fluorescence images, in order to reduce effects of colony translations.

Before we tracked the individual cells within a colony, we computed the background of the images by applying a large scale Gaussian filter and subtracted its values from the image. Afterwards, we used a smaller Gaussian filter for smoothing of the fluorescence image. In order to track single cells in fluorescence images of microcolonies we used the detection and tracking algorithm developed by Blair et al [142].

E.4 IMAGE ANALYSIS OF COLONY ASSEMBLY EXPERIMENTS

We analyzed data, contributed by Nicolas Biais (Brooklyn College, New York) and analyzed by Yen Ting Lin (Los Alamos National Laborator, USA), Johannes Taktikos and Christoph Weber (Harvard University, USA). The data consisted of binary images of the detected edges of bacterial aggregates that were forming on top of the substrate. In total 20 movies, each of a duration of up to 189 minutes, were analyzed. To compute the fraction of cells that were not moving for the complete experiment, we summed all single binary images of the individual experiments. Then, we thresholded the summed image, by setting all those pixel to 1 that also had value 1 in more than 85 % of the single image and all other pixels to 0.

To compute the numbers of cells from the binary images, we computed the area of the individual regions (corresponding to cells or colonies) and estimated the cell number from the area. Therefore, we assumed that aggregates have a shape close to a sphere and the number of cells is proportional to the volume of the colony. For aggregates that had a average cell number below 1, we set $N = 1$.

To compute the substrate density of colonies as a function of the number of cells in the aggregate, we generated a histogram of colony sizes with a bin size of $\delta N = 10$. The moments of the substrate density were estimated from a similar histogram, but with bin size of $\delta N = 1$ cell.

F

SIMULATION DETAILS AND DATA ANALYSIS

The described protocols describe how we initialized and analyzed the simulations of the computational model and give information about the technical implementation of the simulation. The protocols were previously published in the supplemental document of Pönisch et al. [60].

The time steps used in the simulation are given in table F.1, if not stated otherwise.

F.1 SINGLE CELL MOTILITY

We place an individual cell on top of substrate with a distance similar to the cell radius and random cell orientation. For the first 2 seconds of the simulations the cells only interact via the repulsive excluded volume interactions to remove overlaps of the randomly distributed cells and the substrate. After this time we turned on the production and dynamics of pili. To reduce the impact of the initial condition on our results we simulated a time span of 30 minutes and analyzed the last 20 minutes. For every parameter set we analyzed the trajectories of 100 cells and sampled over the parameter set given in table F.2.

Differently to the parameters given in table 2.1 we were using higher mobilities $\mu_{trans} = 10\ \mu m/(pN\ s)$ and $\mu_{trans} = 20\ (\mu m\ pN\ s)^{-1}$ when we studied the parameter set *fast*. This mobilities correspond to the friction of water and guarantee that the force a pilus needs to generate to move a cell with its characteristic velocity v_{ret} is not artificially increased. For this parameter set we picked $\Delta t = \Delta t_{dyn} = 1 \times 10^{-6}$ s.

The parameter sets over which we sampled are given in table F.2.

For studying the dependence of the motility on the number of pili we fixed the maximal number of pili N_{pili} and set the pilus production rate to infinity (see chapter 2.1).

The diffusion coefficient D of the cells were determined from the mean-squared-displacement

$$\langle (\mathbf{r}(t + \Delta t) - \mathbf{r}(t))^2 \rangle_t = 4D\Delta t, \tag{F.1}$$

PARAMETER	VALUES
Time Step Δt [s]	5×10^{-6}
Time step of pili dynamics Δt_{dyn} [s]	2×10^{-2}

Table F.1: Time steps of the simulation.

PARAMETER	VALUES
Pili-substrate detachment force $F_{d,ps}$ [pN]	$10, 20, 30, 180, 300$
Pili-substrate detachment time $t_{d,ps}$ [s]	$5, 10, 30, 60$
Pili-substrate binding rate γ_{att} [Hz]	$0.5, 1, 2, 15$

Table F.2: Sampled parameters for the single cell motility simulations.

PARAMETER	VALUES
Cell number per colony N	1000
Pili-pili detachment force $F_{d,pp}$ [pN]	$120, 180, 240, 300, 360$
Pili-pili detachment time $t_{d,pp}$ [s]	$5, 20, 30, 40, 50, 60, 70$
Pili-pili binding rate $\gamma_{att,pp}$ [Hz]	$0.25, 0.5, 2$

Table F.3: Sampled parameters for the coalescence of colonies.

where $\mathbf{r}(t)$ denotes the center of the projected two-dimensional cell $\mathbf{r}(t)$. In order to compute the velocity at time t of a cell or colony moving along the trajectory $\mathbf{r}(t)$ we computed the displacement

$$\Delta\mathbf{r}(t) = \mathbf{r}(t + \Delta t) - \mathbf{r}(t) \tag{F.2}$$

and set the velocity $\mathbf{v}(t) = \Delta\mathbf{r}(t)/\Delta t$ with $\Delta t = 0.5$ s. This value is in the same order of magnitude as those used in experiments [27, 28]. Additionally, we computed the velocity autocorrelation

$$\langle \mathbf{v}(t + \Delta t)\mathbf{v}(t)\rangle_t = v_{char}^2 \exp\left[-\frac{t}{t_{char}}\right], \tag{F.3}$$

where $\mathbf{v}(t)$ is the time-dependent velocity of the cell.

F.2 COLONY COALESCENCE

We initialized two colonies by randomly distributing N cells (with random orientations) per colonies in two sphere with a radius of $0.85\ N^{1/3}$ μm and distances slightly larger than the sum of the radii of the colonies. For the first 2 seconds we only activated the excluded volume forces in order to remove overlaps of the cells. For the following 100 s we only allowed pili interactions between the cells of the individual colonies in order to create stable colonies. After this time we activated the interactions of pili of both colonies so that the coalescence could start. We simulated the *in silico* colonies for 30 minutes and analyzed the colonies starting from 60 seconds. For every parameter set we analyzed a single coalescence event (see table F.3). For those sets that are presented in table 4.2 and for studying the size-dependence of the coalescence we analyzed at least 14 different realizations.

In order to compute the height of the bridge forming between two colonies and the properties of an ellipse fitted to their shape, we pro-

jected the diplococcus shape of the individual cells onto a plane parallel to the axis between the centers of the two colonies. From the projection of the individual cells we can compute the envelope of the two colonies. In order to compute the bridge height we defined a line of length 1 μm centered around the COM of the projected envelope and parallel to the axis connecting the centers of the two colonies. We moved this line perpendicular to the axis between the colony centers and defined the height of the bridge as the range for which the whole line is inside of the colony envelope. The length of the line was chosen to be small enough so that it was not affected by the circular shape of the projection and large enough so that the effects of the fluctuations of single cells close to the surface of the colonies were reduced. For the late coalescence the results were compared to the short axis of the ellipse. By computing the central moments of the projected two-dimensional area of the microcolonies we were able to compute the properties of the ellipse as explained in [141]. This method allowed us to measure the bridge height and the ellipse properties in a similar manner to the analysis of experimental data.

F.3 FREE SINGLE COLONY

The details of the simulation were previously published in [60].

We initialized a colony by randomly distributing 1700 cells (with random orientations) in a sphere with radius of approximately 10 μm. For the first 2 seconds we only activated the excluded volume forces in order to remove overlaps of the cells. After this time we switched on the production and the dynamics as described in the main text (see section 2). We simulated *in silico* colonies for 30 minutes and analyzed the properties of the colonies for the last 20 minutes. For every parameter set (see table F.4) we analyzed a single colony. For those sets that are presented in the paper we analyzed 10 different realizations.

For the computation of the mean radius of a colony, we projected the diplococcus shape of all individual cells onto the substrate. From the area of the resulting projected colony shape, we could compute the colony radius from the relation $A = \pi R^2$.

To compute the diffusion coefficients of cells within a microcolony as a function of their distance from the COM of the microcolony we introduced multiple shells defined by a minimal distance d_{min} and a maximal distance d_{max} from the center of the microcolony. Afterwards, we picked those parts of the trajectory for which the cells solely moved inside of a single shell for at least 10 s. From these trajectories we computed the time-averaged mean squared displacement (which was additionally averaged over all cells) and estimated the diffusion coefficients. In a similar manner we computed the MSRD. In order to mimic the experimental data, where cells were only tracked in the midplane, we were only picking cells ± 1 μm from the z-position of the center of the colony and computed the MSRD of their x- and y-position. Additionally, we only computed the MSRD for cells that

PARAMETER	VALUES
Cell number N	5, 10, 25, 50, 100, 300, 800, 1600, 1700
Pili-pili detachment force $F_{d,pp}$ [pN]	120, 180, 240, 300, 360
Pili-pili detachment time $t_{d,pp}$ [s]	5, 20, 30, 40, 50, 60, 70
Pili-pili binding rate $\gamma_{att,pp}$ [Hz]	0.25, 0.5, 2

Table F.4: Sampled parameters for the internal dynamics of colonies.

have at least a distance of 5 μm, so that we could reduce correlations due to direct pili-pili-interactions.

In order to compute the pair correlation function of cells within the bulk, we computed the center points of the cells and their relative position to the center of the colony. For every cell we only consider the radius which is smaller than its distance to the mean surface of the colony.

In order to compute the diffusion coefficients of cells within a microcolony as a function of their distance from the COM of the microcolony we introduced multiple shells defined by a minimal distance d_{min} and d_{max} from the center of the microcolony. Afterwards, we picked those parts of the trajectory $\mathbf{r}_i(t)$ for which cell i solely moved inside of a single shell for at least 10s. From these trajectories we computed the time-averaged mean squared displacement (which was additionally averaged over all cells i) and estimated the diffusion coefficients D from the relation

$$\langle(\mathbf{r}_i(t+\Delta t)-\mathbf{r}_i(t))^2\rangle_{i,t} = 6D\Delta t. \tag{F.4}$$

The mean squared relative distance (see chapter G) was computed in a similar manner for pairs of cells that are in the same shell.

F.3.1 *Internal colony dynamics as a function of the excluded volume constant*

We computed the internal properties of individual colonies for strong pili-pili-interactions (see table 4.2) and different values of k_{cc} = 5000, 10000, 15000, 20000, 25000 pN/μm. The results are almost independent of the excluded volume constant for values larger than 10000 pN/μm. For softer cells the intersections of the cells are too strong and affect the result.

F.3.2 *Colony radius as a function of the cell number*

The number of cells N_{cells} within a microcolony of radius R is proportional to the volume of the colony. Thus, we can write

$$N_{cells} = \beta R^3. \tag{F.5}$$

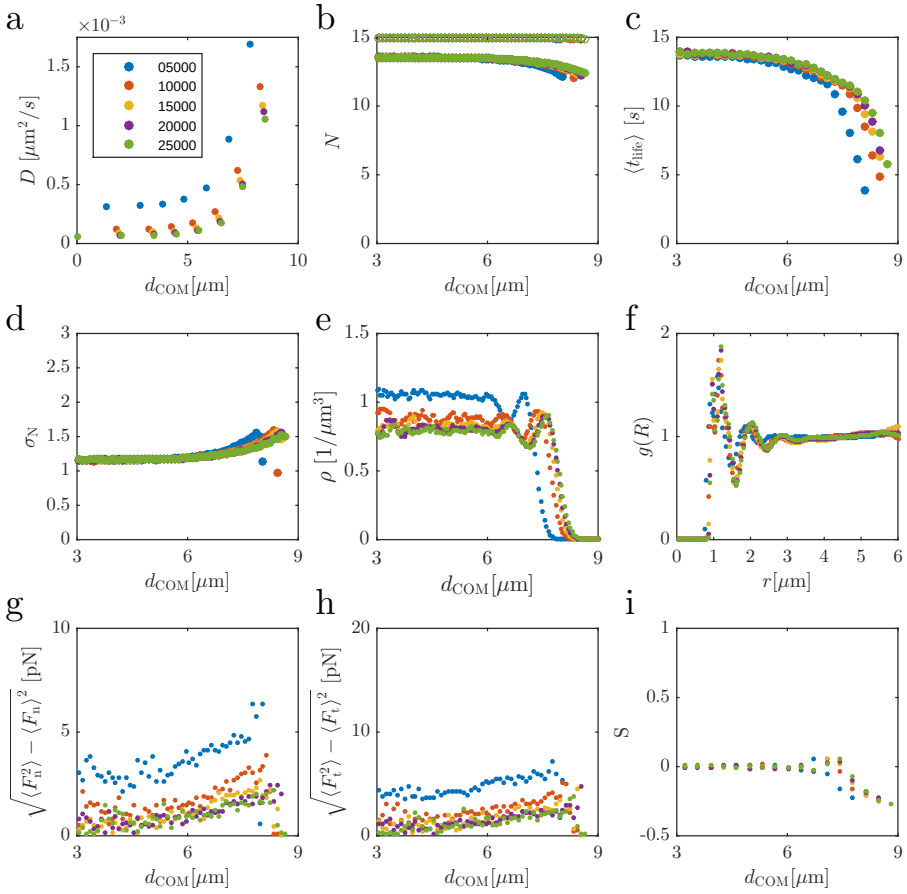

Figure F.1: Internal colony dynamics as a function of the excluded volume constant k_{cc} (in [pN/µm]). (a) Diffusion coefficient D of cells as a function of their distance from the center of the colony d_{com}. (b) Number of total pili (filled circles) and actively pulling pili (hollow circles) of a cell as a function of its distance from the colony center. (c) Life time of pili as a function of d_{com}. Standard deviation of pili as a function of d_{com}. (e) Spatial dependence of the cell number density of colony. (f) Pair correlation function for different values of k_{cc}. (g,h) Square root of the variance of tangential and normal forces for different values of k_{cc}. (i) Nematic order parameter of cells as a function of their distance from the center of the colony d_{com}.

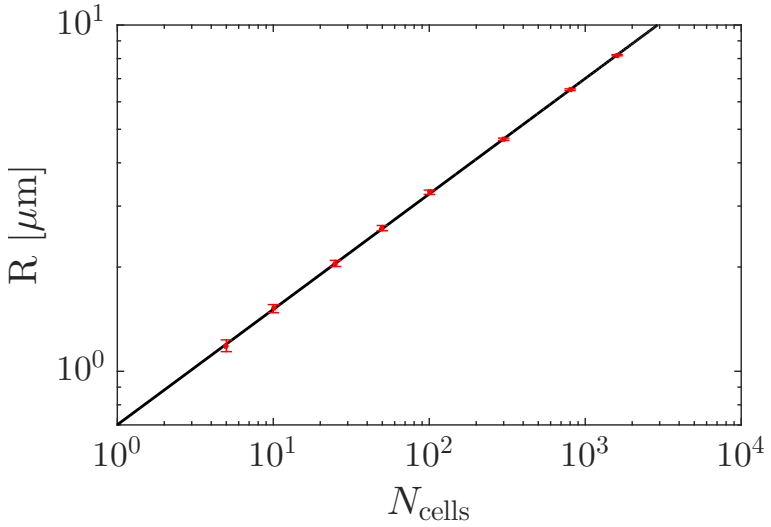

Figure F.2: Colony size as a function of cells within the colony. The radius was computed for spherical colonies simulated with the computational model presented in chapter 2 (see red dots). The colony radius corresponds to the radius of a circle having the same area as the envelope of the two-dimensional projection of a colony (see black line).

In order to determine the proportionality constant β, we used the computational model, presented in chapter 2 and found

$$\beta = (2.92 \pm 0.05)\,\mu\text{m}^{-3}, \tag{F.6}$$

depicted in figure F.2.

F.4 ASSEMBLY ON A SUBSTRATE

The suggested protocol was previously published in the supplementary information of [60].

We initialized 800 - 1200 randomly oriented cells on the substrate with a relative distance to each other that was similar to the cell radius. The cells were distributed in a 2 dimensional box with periodic boundaries and a final cell surface density of 0.62 cells/μm^2. Half of the cells had behaved normally (wildtype cells), the other half were chosen to be mutant cells. For the first two seconds cells only interact via excluded volume forces until all overlaps of the cells with each other and the substrate have vanished. After this time we switched on all pili-mediated interactions and all related interactions of the cells. We simulated a total duration of 60 minutes.

To define which cells are part of the surface and which cells are part of the bulk of a microcolony moving over a surface, we computed the alpha shape of the collection of cocci points of all cells [125, 126]. The underlying idea of this triangulation technique is the motion of a sensor sphere over the surface of the colonies and the individual cells. Such a sphere is not allowed to intersect the positions of the cocci. If any coccus of a cell is touched by such a sphere (thus laying on the surface of the sphere), the corresponding cell is defined to be

a surface cell. The only free parameter is the radius $R_\alpha = 1$ μm which is defined to be in the order of the cell sizes.

G

THE MEAN SQUARED RELATIVE DISTANCE (MSRD)

To estimate the diffusion coefficient of two particles randomly moving within an aggregate that is also performing a random motion, we define the so called mean squared relative distance (MSRD). The necessary calculations were published [143] and are presented in the following.

Two cells a and b at positions $\mathbf{r}_a(t)$ and $\mathbf{r}_b$ have the distance

$$d_{ab}(t) = |\mathbf{r}_a(t) - \mathbf{r}_b(t)|. \tag{G.1}$$

This quantity is independent of any translational or rotational motion of the aggregate in two dimensions. For this distance, we define the MSRD δ_{MSRD} as the squared mean of the change of the distance with time t:

$$\delta_{MSRD}(t) = \langle (d_{ab}(t) - d_{ab}(0))^2 \rangle. \tag{G.2}$$

A graphical representation of the quantities is shown in figure G.1.

G.1 DERIVATION OF THE ENSEMBLE - AND TIME - AVERAGED MSRD IN TWO DIMENSIONS

To calculate the ensemble-averaged MSRD, we first reduce the motion of two particles (given by $i = a, b$) to the motion of an individual particle. Here, the two particles exhibit a random motion without any boundary conditions. We assume that the central limit theorem is valid to characterize their motion [51]. The probability density functions of their positions (x, y), defined in cartesian coordinates, is then given by a Gaussian distribution

$$p_i(x, y, t) = \frac{1}{4\pi D_i t} \exp\left(-\frac{x^2 + y^2}{4 D_i t}\right), \tag{G.3}$$

with the diffusion coefficient D_i. The probability density function of the distance vector between these two particles, starting with an initial distance d_0 in $y-$direction, is then given by

$$\begin{aligned} p_{ab}(x, y, t) &= \iint dx' dy' \; p_a(x - x', y - y', t) p_b(x', y', t) \\ &= \frac{1}{4\pi D_{ab} t} \exp\left[-\frac{x^2 + (y - d_0)^2}{4 D_{ab} t}\right], \end{aligned} \tag{G.4}$$

corresponding to the probability density function of a Gaussian random walker that starts from the position $(0, d_0)$ and has a diffusion coefficient $D_{ab} = D_a + D_b$.

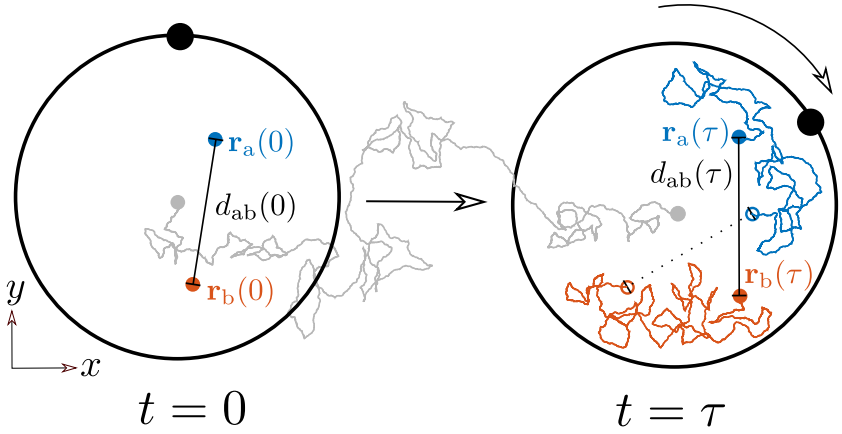

Figure G.1: Sketch of a simplified two-dimensional aggregate, adapted from [143]. Two particles are initially separated by a distance $d_{ab}(0)$. Within the time τ, they perform random motion in a circular domain (see solid lines). However, the aggregate itself is rotating (as marked by the black dot on the boundary of the domain) and its center of mass is also moving randomly (grey line). To quantify the diffusivity of particles, we follow their absolute relative distance as a function of time $d_{ab}(t)$, independent of the motion of the domain.

For $d_0 = 0$ the probability density function of the scalar distance d_{ab} of a Gaussian random walk is given by the Rayleigh distribution [144, 145],

$$p_{ray}(d_{ab}, t) = \frac{d_{ab}}{2D_{ab}t} \exp\left(-\frac{d_{ab}^2}{4D_{ab}t}\right), \tag{G.5}$$

with I_0 being the modified Bessel function of the first kind. For a initial distance d_0 larger than zero, the probability density function of the scalar distance d_{ab} is given by the Rice distribution [146],

$$p_{rice}(d_{ab}, t) = \frac{d_{ab}}{2D_{ab}t} \exp\left(-\frac{d_{ab}^2 + d_0^2}{4D_{ab}t}\right) I_0\left(\frac{d_{ab}d_0}{2D_{ab}t}\right). \tag{G.6}$$

This equation is regularly used in radar and sonar signal processing. In order to compute the MSRD, we compute the first two moments of this probability density function:

$$\begin{aligned}\langle d_{ab}(t)\rangle &= \frac{\sqrt{\pi}}{4\sqrt{D_{ab}t}} \exp\left[-\frac{d_0^2}{8D_{ab}t}\right] \\ &\quad \times \left[(d_0^2 + 4D_{ab}t) I_0\left(\frac{d_0^2}{8D_{ab}t}\right) + d_0^2 I_1\left(\frac{d_0^2}{8D_{ab}t}\right)\right] \qquad \text{(G.7)} \\ \langle d_{ab}^2(t)\rangle &= d_0^2 + 4D_{ab}t. \qquad \text{(G.8)}\end{aligned}$$

Here, $I_1(x)$ is the modified Bessel function of the first kind. Then, the ensemble-averaged MSRD is given by

$$\begin{aligned}\delta_{MSRD} &= \langle [d_{ab}(t) - d_{ab}(0)]^2 \rangle \\ &= \langle d_{ab}^2(t)\rangle - 2d_0\langle d_{ab}(t)\rangle + d_0^2 \qquad \text{(G.9)}\end{aligned}$$

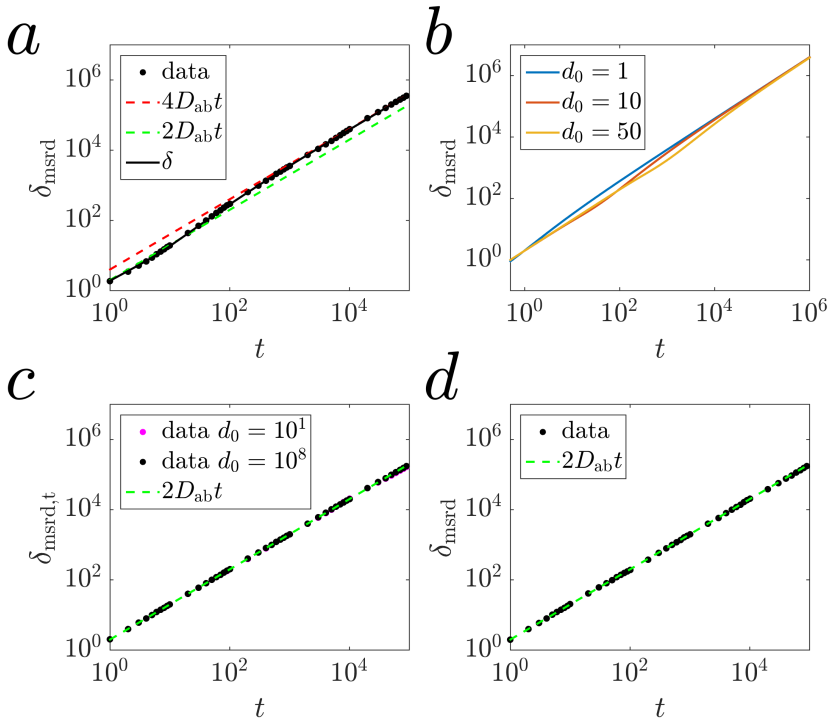

Figure G.2: Mean-squared relative distance for the random motion of two cells without boundary conditions. Here, $D_{ab} = D_a + D_b = 1$ is the sum of the diffusion coefficients of the individual trajectories. The figure was adapted from [143]. (a) Ensemble-averaged MSRD for $d_0 = 4$. For small times t the MSRD follows $2D_{ab}t$, for large times it follow $4D_{ab}t$. Additionally, equation G.9 predicts the behavior of the MSRD for all times. (b) Ensemble-averaged MSRD for different initial conditions d_0, as given by equation G.9. (c) Time-averaged MSRD for two particles with different initial distances d_0. In both cases the MSRD follows the function $2D_{ab}t$. (d) Ensemble-averaged MSRD for randomly picked initial values d_0.

where $d_{ab}(0) = d_0$. The behavior of this function (see equation G.9) is shown in figure (see figure G.2a). For $d_0^2 \ll D_{ab}t$ we can approximate

$$\delta_{MSRD} \simeq 4D_{ab}t \tag{G.10}$$

and for $d_0^2 \gg D_{ab}t$

$$\delta_{MSRD} \simeq 2D_{ab}t, \tag{G.11}$$

as can be seen in figure G.2a. While d_0 does not affect the behavior for large or small values of the time t (compared to d_0^2/D_{ab}), it affects the transition between these two limits, as can be seen in figure G.2b.

In order to compute the time-averaged MSRD, defined by

$$\delta_{MSRD,t}(\Delta t) = \langle (d_{ab}(t+\Delta t) - d_{ab}(t))^2 \rangle_t, \tag{G.12}$$

we first need to compute the sum of all density functions of distances for $t \in [0, T]$, given by

$$\tilde{p}_{rice} = \lim_{T\to\infty} \frac{\int_0^T dt\, p_{rice}(d,t)}{\int_0^T dt}. \tag{G.13}$$

With $u = t/T$, this equation can be substituted to

$$\tilde{p}_{rice} = \lim_{T\to\infty} \int_0^1 du\, \frac{d_{ab}}{2D_{ab}uT} \exp\left[-\frac{d_{ab}^2 + d_0^2}{4D_{ab}uT}\right] I_0\left(\frac{d_{ab}d_0}{2D_{ab}uT}\right) \tag{G.14}$$

For $T \to \infty$ the function within the integral converges

$$\lim_{T\to\infty} \frac{d}{2D_{ab}uT} \exp\left[-\frac{d^2 + d_0^2}{4D_{ab}uT}\right] I_0\left(\frac{dd_0}{2D_{ab}uT}\right) = 0. \tag{G.15}$$

An exchange of the limit and the integration is valid because the equation beneath the integral is uniformly convergent [147]. The resulting distribution is uniform, what tell us that all distances d are equally likely and there are no memory effects of the initial distance d_0.

In the next step we compute the mean of the MSRD $\delta_{MSRD}(d, \Delta t)$ for this uniform distribution, given by

$$\delta_{MSRD,t}(\Delta t) = \lim_{g\to\infty} \frac{\int_0^g dd\, \delta_{MSRD}(d, \Delta t)}{g} \simeq 2D_{ab}\Delta t. \tag{G.16}$$

Again, we use a substitution of the form $u = d/g$ to simplify the integral. The resulting function is visualized in figure G.2c.

We suggest that the difference of the ensemble-averaged and the time-averaged MSRD originates from the difference in the initial conditions of the random walks. While we picked the same initial condition d_0 for the computation of the ensemble-averaged MSRD, it follows from the definition of the time-averaged MSRD that the initial condition is constantly changing. This idea is supported by ensemble-averaging the MSRD of two simulated pairs of trajectories with randomly chosen initial distances d_0. Check the following section G.2 for more details of the simulation. Therefore, the start points of the random walks where chosen independently of each other such that they were randomly distributed within a circle of radius $R = 1000$. In this case, we observe that the MSRD shows the same behavior as the time-averaged one (see figure G.2d).

G.2 SIMULATION RESULTS

In order to study the behavior of the mean squared relative distance (MSRD), we simulated the trajectories of pairs of Gaussian random walks ($i = a, b$) with diffusion coefficients $D = D_a = D_b = 0.5$ (given as a unitless quantity) and an initial distance $d_0 = 4$. By computing the scalar distance of the 2000 pairs of trajectories, defined in equation G.1, we can compute the MSRD in the ensemble average (see figure G.2a). We observe that the MSRD can be approximated by the equation $\delta_{MSRD} = 4Dt$ for small times t, and by $\delta_{MSRD} = 8Dt$ for large times, as predicted in the previous chapter.

The MSRD can also be computed by performing an time-average. Therefore, we computed two trajectories consisting of 10^7 individual steps, with equal properties as the trajectories simulated for the ensemble-average. In this case, the MSRD follows $\delta_{MSRD,t} = 4Dt$ and is independent of the initial distance d_0 (see figure G.2c).

G.3 EFFECTS OF RADIAL BOUNDARY CONDITIONS

Until now, we neglected the role of boundary conditions while studying the MSRD. In most cases, the cells will move within aggregates that are spatially confined, as in our case of bacterial microcolonies. Here, we consider the effects of boundaries by simulating the two-dimensional motion of the two Gaussian random walkers within a circle of radius $R = 200$ (see figure G.1) with reflective boundaries.

Our simulations show that the behavior of the ensemble- and time-averaged MSRD corresponds to the MSRD with free boundaries for values of the MSRD that correspond to values smaller than the radius R of the circle (see figure G.3). For larger values, the MSRD saturates towards the values $\delta_{Satur,e}$ for the ensemble average and $\delta_{Satur,t}$ for the time average, due to the limited size of the circle. In order to compute the values of $\delta_{Satur,e}$ and $\delta_{Satur,e}$, we suggest that for large times, the positions of two particles ($i = a, b$) within a circle of radius R are uncorrelated and homogeneously distributed

$$p_{circ}(\mathbf{r}_i) = \frac{1}{\pi R^2} \begin{cases} 1, & \mathbf{r}_i \leqslant R \\ 0, & \mathbf{r}_i > R \end{cases}. \tag{G.17}$$

The probability density function for two independent particles is then given by

$$p_{ab,circ}(\mathbf{r}_a, \mathbf{r}_b) = p_{circ}(\mathbf{r}_a) p_{circ}(\mathbf{r}_b). \tag{G.18}$$

To compute the ensemble averaged saturation value of the MSRD, $\delta_{Satur,e}$, we define the distance of the two particles in polar coordinates (R_1, ϕ_1) and (R_2, ϕ_2)

$$\begin{aligned} d_{ab} =& |\mathbf{r}_a - \mathbf{r}_b| \\ =& \sqrt{(R_1 \cos\phi_1 - R_2 \cos\phi_2)^2 + (R_1 \sin\phi_1 - R_2 \sin\phi_2)^2}, \end{aligned} \tag{G.19}$$

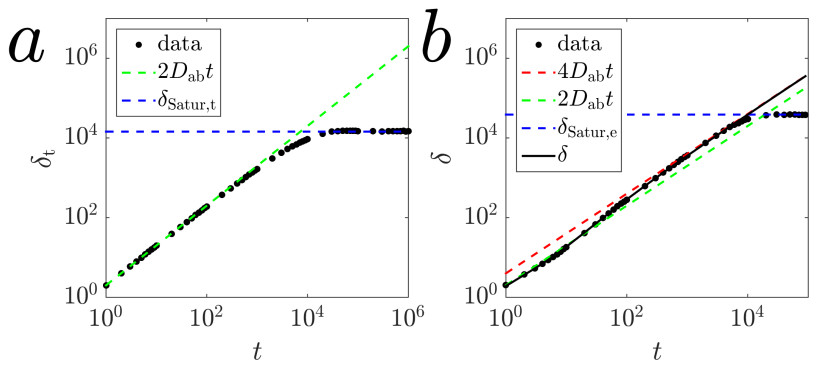

Figure G.3: Mean-squared relative distance for the random motion of two cells moving within a circle. (a) Time-averaged MSRD with the scaling $2D_{ab}t$ and the saturation MSRD $\delta_{Satur,t}$. (a) Ensemble-averaged MSRD following equation G.9 until the saturation MSRD $\delta_{Satur,e}$.

so that

$$\begin{aligned}\delta_{Satur,e}(R, d_0) =& \langle (d_{ab}(t) - d_{ab}(0))^2 \rangle_{p_{ab,circ}} \\ =& R^2 + d_0^2 - 2d_0 f,\end{aligned} \tag{G.20}$$

where

$$\begin{aligned}f(R) &= \frac{8}{\pi^2 R^4} \int_0^R dR_1 \int_0^R dR_2 \left[R_1 R_2 |R_1 - R_2| E\left(-\frac{4R_1 R_2}{(R_1 - R_2)^2} \right) \right] \\ &= \frac{8R}{\pi^2} \int_0^1 du_1 \int_0^1 du_2 \left[u_1 u_2 |u_1 - u_2| E\left(-\frac{4u_1 u_2}{(u_1 - u_2)^2} \right) \right] \\ &\simeq \frac{128}{45\pi^2} R\end{aligned} \tag{G.21}$$

and with $E(x)$ being the complete elliptic integral of x. Here, we define $d_{ab}(0) = d_0$. The integral was solved numerically and seems to be given by $16/45$.

The time-averaged saturation value of the MSRD is calculated by assuming that the initial positions of the particles are homogeneously distributed within the circle area A and thus we integrate

$$d_0 = |\mathbf{r}_{o,a} - \mathbf{r}_{o,b}| \tag{G.22}$$

over all positions of the two particles within the circle:

$$\begin{aligned}\delta_{Satur,t}(R) =& \int_A d\mathbf{r}_{o,a} \int_A d\mathbf{r}_{o,b}\ \delta_{Satur,e}(d_0) \\ =& 2R^2 - 2f^2.\end{aligned} \tag{G.23}$$

Again, the resulting value of the MSRD $\delta_{Satur,t}$ can be computed numerically.

The saturation values depend on the initial positions of the two particles for the ensemble-average and do not depend on the initial condition for the time average. They are shown in figure G.3.

H

LIST OF IMPORTANT SYMBOLS

CHAPTER 1

v	velocity of Brownian particle
v_0	initial velocity of Brownian particle
t	time
μ	friction
Γ	Langevin force
Γ_0	noise strength
k	Boltzmann constant
T	temperature
m	mass of the Brownian particle
x	position of the Brownian particle
D	diffusion coefficient of Brownian particle
P	probability of a particle to be at a point x at time t
p	probability to jump to the right
V	drift

CHAPTER 2

Δt	time step
R	cocci radius
d_{cocci}	cocci distance
$\mathbf{r}_i^{(a)}, \mathbf{r}_i^{(b)}$	positions of cocci a and b of cell i
$\mathbf{r}_i^{(com)}$	center of cell i
k_{cc}	cell-cell excl. vol. const.
$\mathbf{F}_{ij}^{(cc)}$	excl. vol. force due to overlap of cells i and j
k_{cs}	cell-sub. excl. vol. const.
$\mathbf{F}_j^{(cs)}$	excl. vol. force due to coccus j and substrate
$\mathbf{F}_k^{(ps)}, \mathbf{F}_k^{(pp)}$	pulling forces due to pilus k
μ_{trans}	translational mobility
μ_{rotat}	rotational mobility
l_{pers}	pilus persistence length
γ_{prod}	pili production rate
N_{max}	maximal pili number
v_{pro}	pili protrusion velocity
v_{ret}	pili retraction velocity
v_0	velocity of pilus
$l_k^{(cont)}$	contour length of pilus k
$l_k^{(free)}$	free length of pilus k
γ_{ret}	switching rate from protrusion to retraction
l_c	mean pili length
$\mathbf{r}_k^{(s)}$	start point of pilus k
$\mathbf{r}_k^{(e)}$	end point of pilus k
k_{pili}	pili spring constant
F_{stall}	pili stalling force
$F_{d,pp}$	pili-pili detachment force
$F_{d,ps}$	pili-sub. detachment force
$t_{d,pp}$	pili-pili detachment time
$t_{d,ps}$	pili-sub. detachment time
$\gamma_{att,pp}$	pili-pili binding rate
$\gamma_{att,ps}$	pili-sub. binding rate
$\gamma_{det}^{(sub)}$	pili-sub. detachment rate
$\gamma_{det}^{(pili)}$	pili-pili detachment rate
$\mathbf{F}_i^{(tot)}$	total force acting on cell i
$\mathbf{T}_i^{(tot)}$	total torque acting on cell i
$\mathbf{w}_i^{(tot)}$	angular velocity of cell i

CHAPTER 3

$F_{d,ps}^{(1)}, F_{d,ps}^{(2)}$	pili-sub. detachment forces
$t_{d,ps}^{(1)}, t_{d,ps}^{(2)}$	pili-sub. detachment times
$\gamma_{att,ps}$	pili-sub. attachment rate
μ_{trans}	translational mobility
μ_{rotat}	rotational mobility
$\gamma_{det}^{(sub)}$	pili-sub. detachment rate
N_{total}	complete number of pili of a cell
N_l, N_r	attached pili on the left and right side
P	probability of a motility state
T	transition matrix between motility states
N_{free}	number of non-attached pili
γ_{att}	effective attachment rate
F_{stall}	stalling force
k_{pili}	pilus spring constant
μ_{trans}	translational mobility
v_{ret}	pilus retraction velocity
v_c	velocity of the cell
L	mean displacement of a pilus
MSD	mean squared displacement
t	time
$\mathbf{r}$	position of the cell
d	dimensionality
D	diffusion coefficient
VACF	velocity autocorrelation function
v_{char}	characteristic velocity
t_{char}	correlation time
l_{char}	correlation length
$l_{xyz}^{(all)}$	contour length of a pilus
$l_{xy}^{(att)}$	length of an att. pilus projected on substrate

CHAPTER 4

t	time
h, h_1, h_2	bridge height
t_h, t_0, t_1, t_2	characteristic times of bridge closure
η	viscosity
χ	surface tension
h_0	relaxed bridge height
γ	ratio of short and long axis
a	short axis of ellipse
b, γ_h	long axis of ellipse
t_γ	relaxation time of axis ratio
β	initial axis ratio
δ_{MSRD}	mean squared relative distance
δ_{MSD}	mean squared displacement
d	scalar distance of two cells
D	diffusion coefficient
δ_0	offset of MSRD
$F_{d,pp}$	pili-pili detachment force
$t_{d,pp}$	pili-pili detachment time
$\gamma_{att,pp}$	pili-pili binding rate
D_0	offset of the diffusion coefficient within colony
D_r	magnitude of the motility gradient
l_D	char. length scale of gradient of motility
ρ	cell density
d_{com}	distance from the center of the colony
ω	width of the density profile
ρ_0	density within the colony bulk
S	nematic order parameter
α	cell orientation angle
$g(r)$	pair correlation function
R	final colony radius
ϕ	volume fraction of a colony
D_{eff}	effective diffusion coefficient
D_{aq}	diffusion coefficient of a solute in water
Δr	displacement

CHAPTER 6

t, t'	time
N	number of cells in colony
R	radius of colony
A	projected area of the colony
c	density of colonies of size N
M_i	ith moment of the density
t_{div}	division time of bacteria
γ_{div}	division rate of bacteria
$P_i(t)$	probability that i cells will not divide before time t
p_i	probability density function of division times of i cells
C	proliferation term
A	aggregation term
F	fragmentation term
K_{ij}	aggregation rate of colonies with i and j cells
D_i	diffusion coefficient of colony of i cells
K_0	aggregation proportionality constant
k	Boltzmann constant
T	temperature
η	viscosity
F_0	fragmentation rate

BIBLIOGRAPHY

[1]S. Macfarlane, A. McBain, and G. Macfarlane, "Consequences of biofilm and sessile growth in the large intestine," Adv. Dent. Res. **11**, 59–68 (1997).

[2]D. T. Andersen et al., "Discovery of large conical stromatolites in lake untersee, antarctica," Geobiology **9**, 280–293 (2011).

[3]E. Chicote et al., "Biofouling on the walls of a spent nuclear fuel pool with radioactive ultrapure water," Biofouling **20**, 35–42 (2004).

[4]P. Stoodley et al., "Biofilms as complex differentiated communities," Annu. Rev. Microbiol. **56**, 187–209 (2002).

[5]G. O'Toole, H. B. Kaplan, and R. Kolter, "Biofilm formation as microbial development," Annu. Rev. Microbiol. **54**, 49–79 (2000).

[6]H. C. Berg and R. A. Anderson, "Bacteria swim by rotating their flagellar filaments," Nature **245** (1973) 10.1038/245380a0.

[7]H. C. Berg, *Random walks in biology* (Princeton University Press, 1993).

[8]L. Turner, W. S. Ryu, and H. C. Berg, "Real-time imaging of fluorescent flagellar filaments," J. Bacteriol. **182**, 2793–2801 (2000).

[9]H. C. Berg, *E. coli in Motion* (Springer Science & Business Media, 2008).

[10]H. C. Berg, D. A. Brown, et al., "Chemotaxis in Escherichia coli analysed by three-dimensional tracking," Nature **239**, 500–504 (1972).

[11]R. H. Luchsinger, B. Bergersen, and J. G. Mitchell, "Bacterial swimming strategies and turbulence," Biophys. J. **77**, 2377–2386 (1999).

[12]G. M. Barbara and J. G. Mitchell, "Bacterial tracking of motile algae," FEMS Microbiol. Ecol. **44**, 79–87 (2003).

[13]Y. Magariyama et al., "Difference between forward and backward swimming speeds of the single polar-flagellated bacterium, Vibrio alginolyticus," FEMS Microbiol. Lett. **205**, 343–347 (2001).

[14]T. Nakai, M. Kikuda, and Y. Kuroda, "Speed, trajectory and increment in the number of cells of singly flagellated bacteria swimming close to boundaries," J. Biomed. Sci. Eng. **4**, 2–10 (2009).

[15]A. J. Merz and M. So, "Interactions of pathogenic neisseriae with epithelial cell membranes," Annu. Rev. Cell Dev. Bi. **16**, 423–457 (2000).

[16]R. Townsin, "The ship hull fouling penalty," Biofouling **19**, 9–15 (2003).

[17]B. W. Trautner and R. O. Darouiche, "Role of biofilm in catheter-associated urinary tract infection," Am J. Infect. Control **32**, 177–183 (2004).

[18]N. Verstraeten et al., "Living on a surface: swarming and biofilm formation," Trends Microbiol. **16**, 496 (2008).

[19]D. Kaiser, "Bacterial swarming: a re-examination of cell-movement patterns," Curr. Biol. **17**, R561–R570 (2007).

[20]T. Köhler et al., "Swarming of Pseudomonas aeruginosa is dependent on cell-to-cell signaling and requires flagella and pili," J. Bacteriol. **182**, 5990–5996 (2000).

[21]D. B. Kearns, "A field guide to bacterial swarming motility," Nat. Rev. Microbiol. **8**, 634–644 (2010).

[22]J. S. Mattick, "Type IV pili and twitching motility," Annu. Rev. Microbiol. **56**, 289–314 (2002).

[23]B. Maier, "The bacterial type IV pilus system–a tunable molecular motor," Soft Matter **9**, 5667–5671 (2013).

[24]J. Eriksson et al., "Characterization of motility and piliation in pathogenic Neisseria," BMC Microbiol. **15**, 92 (2015).

[25]A.-F. Imhaus and G. Duménil, "The number of Neisseria meningitidis type IV pili determines host cell interaction," EMBO J. **33**, 1767–1783 (2014).

[26]M. L. Gibiansky et al., "Bacteria use type IV pili to walk upright and detach from surfaces," Science **330**, 197–197 (2010).

[27]C. Holz et al., "Multiple pilus motors cooperate for persistent bacterial movement in two dimensions," Phys. Rev. Lett. **104**, 178104 (2010).

[28]V. Zaburdaev et al., "Uncovering the mechanism of trapping and cell orientation during Neisseria gonorrhoeae twitching motility," Biophys. J. **107**, 1523–1531 (2014).

[29]L. Craig, M. E. Pique, and J. A. Tainer, "Type IV pilus structure and bacterial pathogenicity," Nat. Rev. Microbiol. **2**, 363–378 (2004).

[30]J. Swanson, S. J. Kraus, and E. C. Gotschlich, "Studies on gonococcus infection," J. Exp. Med. **134**, 886–906 (1971).

[31]J. M. Skerker and H. C. Berg, "Direct observation of extension and retraction of type IV pili," P. Natl. Acad. Sci. USA **98**, 6901–6904 (2001).

[32]B. Maier et al., "Single pilus motor forces exceed 100 pN," P. Natl. Acad. Sci. USA **99**, 16012–16017 (2002).

[33]N. Biais et al., "Cooperative retraction of bundled type IV pili enables nanonewton force generation," PLoS Biol. **6**, e87 (2008).

[34]R. Marathe et al., "Bacterial twitching motility is coordinated by a two-dimensional tug-of-war with directional memory," Nat. Commun. **5**, 1–10 (2014).

[35]Y.-W. Chang et al., "Architecture of the type IVa pilus machine," Science **351**, aad2001 (2016).

[36]R. Kurre and B. Maier, "Oxygen depletion triggers switching between discrete speed modes of gonococcal type IV pili," Biophys. J. **102**, 2556–2563 (2012).

[37]R. Kurre et al., "Pilt2 enhances the speed of gonococcal type IV pilus retraction and of twitching motility," Mol. Microbiol. **86**, 857–865 (2012).

[38]M. J. Müller, S. Klumpp, and R. Lipowsky, "Tug-of-war as a cooperative mechanism for bidirectional cargo transport by molecular motors," P. Natl. Acad. Sci. USA **105**, 4609–4614 (2008).

[39]K. Lee et al., "The binding of Pseudomonas aeruginosa pili to glycosphingolipids is a tip-associated event involving the C-terminal region of the structural pilin subunit," Mol. Microbiol. **11**, 705–713 (1994).

[40]W. Y. Wong et al., "Structure-function analysis of the adherence-binding domain on the pilin of Pseudomonas aeruginosa strains PAK and KB7.," Biochemistry **34**, 12963–12972 (1995).

[41]H. Harvey et al., "Single-residue changes in the C-terminal disulfide-bonded loop of the Pseudomonas aeruginosa type IV pilin influence pilus assembly and twitching motility," J. Bacteriol. **191**, 6513–6524 (2009).

[42]C. L. Giltner et al., "The Pseudomonas aeruginosa type IV pilin receptor binding domain functions as an adhesin for both biotic and abiotic surfaces," Mol. Microbiol. **59**, 1083–1096 (2006).

[43]R. W. Heiniger et al., "Infection of human mucosal tissue by Pseudomonas aeruginosa requires sequential and mutually dependent virulence factors and a novel pilus-associated adhesin," Cell. Microbiol. **12**, 1158–1173 (2010).

[44]C. L. Giltner, Y. Nguyen, and L. L. Burrows, "Type IV pilin proteins: versatile molecular modules," Microbiol Mol. Biol. R. **76**, 740–772 (2012).

[45]J. D. Shrout, "A fantastic voyage for sliding bacteria," Trends Microbiol. **23**, 244–246 (2015).

[46]R. Fall, D. B. Kearns, and T. Nguyen, "A defined medium to investigate sliding motility in a Bacillus subtilis flagella-less mutant," BMC Microbiol. **6**, 31 (2006).

[47]R. Brown, "XXVII. A brief account of microscopical observations made in the months of June, July and August 1827, on the particles contained in the pollen of plants; and on the general existence of active molecules in organic and inorganic bodies," Philos. Mag. **4**, 161–173 (1828).

[48]A. Einstein, "Über die von der molekularkinetischen Theorie der Wärme geforderte Bewegung von in ruhenden Flüssigkeiten suspendierten Teilchen," Ann. Phys. **322**, 549–560 (1905).

[49]M. Von Smoluchowski, "Zur kinetischen Theorie der Brownschen Molekularbewegung und der Suspensionen," Ann. Phys. **326**, 756–780 (1906).

[50]H. Risken, *The Fokker-Planck Equation. Methods of Solution and Applications* (Springer Series in Synergetics, 1989).

[51]N. G. van Kampen, *Stochastic processes in physics and chemistry* (Elsevier, 1995).

[52]P. C. Bressloff, *Stochastic processes in cell biology*, Vol. 41 (Springer, 2014).

[53]S. Ramaswamy, "The mechanics and statistics of active matter," Annu. Rev. Condens. Matter Phys. **1**, 323–345 (2010).

[54]D. L. Higashi et al., "Dynamics of Neisseria gonorrhoeae attachment: microcolony development, cortical plaque formation, and cytoprotection," Infect. Immun. **75**, 4743–4753 (2007).

[55]J. W. Costerton, *The biofilm primer*, Vol. 1 (Springer Science & Business Media, 2007).

[56]K. P. Talaro and B. Chess, *Foundations in microbiology* (McGraw-Hill, 2015).

[57]E. R. Oldewurtel et al., "Differential interaction forces govern bacterial sorting in early biofilms," Elife **4**, e10811 (2015).

[58]A. Ward et al., "Solid friction between soft filaments," Nat. Mater. **14**, 583 (2015).

[59]J. Taktikos et al., "Pili-induced clustering of N. gonorrhoeae bacteria," PloS One **10**, e0137661 (2015).

[60]W. Pönisch et al., "Multiscale modeling of bacterial colonies: how pili mediate the dynamics of single cells and cellular aggregates," New J Phys **19**, 015003 (2017).

[61]R. D. Monds and G. A. O'Toole, "The developmental model of microbial biofilms: ten years of a paradigm up for review," Trends Microbiol. **17**, 73–87 (2009).

[62]S. M. Hinsa et al., "Transition from reversible to irreversible attachment during biofilm formation by Pseudomonas fluorescens WCS365 requires an ABC transporter and a large secreted protein," Mol. Microbiol **49**, 905–918 (2003).

[63]L. Hall-Stoodley, J. W. Costerton, and P. Stoodley, "Bacterial biofilms: from the natural environment to infectious diseases," Nat. Rev. Microbiol. **2**, 95–108 (2004).

[64]M. Klausen et al., "Involvement of bacterial migration in the development of complex multicellular structures in Pseudomonas aeruginosa biofilms," Mol. Microbiol. **50**, 61–68 (2003).

[65]J. W. Costerton et al., "Microbial biofilms," Annu. Rev. Microbiol. **49**, 711–745 (1995).

[66]C. Potera, "Antibiotic resistance: biofilm dispersing agent rejuvenates older antibiotics," Environ. Health Persp. **118**, A288 (2010).

[67]P Stoodley et al., "Biofilm material properties as related to shear-induced deformation and detachment phenomena," J. Ind. Microbiol. Biot. **29**, 361–367 (2002).

[68]A. Fonseca and J. Sousa, "Effect of shear stress on growth, adhesion and biofilm formation of Pseudomonas aeruginosa with antibiotic-induced morphological changes," Int. J. Antimicrob. Ag. **30**, 236–241 (2007).

[69]M. O. Elasri and R. V. Miller, "Study of the response of a biofilm bacterial community to UV radiation," Appl. Environ. Microb. **65**, 2025–2031 (1999).

[70]C. Matz et al., "Biofilm formation and phenotypic variation enhance predation-driven persistence of Vibrio cholerae," P. Natl. Acad. Sci. USA **102**, 16819–16824 (2005).

[71]L. S. Cairns, L. Hobley, and N. R. Stanley-Wall, "Biofilm formation by Bacillus subtilis: new insights into regulatory strategies and assembly mechanisms," Mol. Microbiol. **93**, 587–598 (2014).

[72]M. M. Harriott and M. C. Noverr, "Candida albicans and Staphylococcus aureus form polymicrobial biofilms: effects on antimicrobial resistance," Antimicrob. Agents Ch. **53**, 3914–3922 (2009).

[73]M. M. Harriott and M. C. Noverr, "Importance of Candida–bacterial polymicrobial biofilms in disease," Trends Microbiol. **19**, 557–563 (2011).

[74]T. Dalton et al., "An in vivo polymicrobial biofilm wound infection model to study interspecies interactions," PloS One **6**, e27317 (2011).

[75]H. Vlamakis et al., "Control of cell fate by the formation of an architecturally complex bacterial community," Gene. Dev. **22**, 945–953 (2008).

[76]Y Irie and M. Parsek, "Quorum sensing and microbial biofilms.," Curr. Top. Microbiol. **322**, 67 (2008).

[77]A. Persat et al., "The mechanical world of bacteria," Cell **161**, 988–997 (2015).

[78]W. H. Organization, "Emergence of multi-drug resistant Neisseria gonorrhoeae: threat of global rise in untreatable sexually transmitted infections," (2011).

[79]H. Wang et al., "Global, regional, and national life expectancy, all-cause mortality, and cause-specific mortality for 249 causes of death, 1980-2015: a systematic analysis for the global burden of Disease Study 2015," Lancet **388**, 1459–1544 (2016).

[80]M. Bender, "Ueber neuere Antigonorrhoica (insbes. Argonin und Protargol)," Archiv für Dermatologie und Syphilis **43**, 31–36 (1898).

[81]N. N. Horn et al., "Antimicrobial susceptibility and molecular epidemiology of Neisseria gonorrhoeae in Germany," Int. J. Med. Microbiol. **304**, 586–591 (2014).

[82]R. D. Kirkcaldy et al., "Trends in antimicrobial resistance in Neisseria gonorrhoeae in the USA: the Gonococcal Isolate Surveillance Project (GISP), January 2006–June 2012," Sex. Transm. Infect. **89**, iv5–iv10 (2013).

[83]M. Unemo and W. M. Shafer, "Antimicrobial resistance in Neisseria gonorrhoeae in the 21st century: past, evolution, and future," Clin. Microbiol. Rev. **27**, 587–613 (2014).

[84]R. D. Kirkcaldy, "Neisseria gonorrhoeae antimicrobial susceptibility surveillance - the gonococcal isolate surveillance project, 27 sites, United States, 2014," MMWR Surveill. Summ. **65**, 1–19 (2016).

[85]M. Ohnishi et al., "Is Neisseria gonorrhoeae initiating a future era of untreatable gonorrhea?: Detailed characterization of the first strain with high-level resistance to ceftriaxone," Antimicrob. Agents Ch. **55**, 3538–3545 (2011).

[86]M. M. Lahra, N. Ryder, and D. M. Whiley, "A new multidrug-resistant strain of Neisseria gonorrhoeae in Australia," New Engl. J. Med. **371**, 1850–1851 (2014).

[87]M. Unemo, D. Golparian, and B. Hellmark, "First three Neisseria gonorrhoeae isolates with high-level resistance to azithromycin in sweden: a threat to currently available dual-antimicrobial regimens for treatment of gonorrhea?" Antimicrob. Agents Ch. **58**, 624–625 (2014).

[88]H. Källström et al., "Membrane cofactor protein (MCP or CD46) is a cellular pilus receptor for pathogenic Neisseria," Mol. Microbiol. **25**, 639–647 (1997).

[89]A. J. Merz and M. So, "Attachment of piliated, Opa-and Opc- gonococci and meningococci to epithelial cells elicits cortical actin rearrangements and clustering of tyrosine-phosphorylated proteins.," Infect. Immun. **65**, 4341–4349 (1997).

[90]S. Lu et al., "Nanoscale pulling of type IV pili reveals their flexibility and adhesion to surfaces over extended lengths of the pili," Biophys. J. **108**, 2865–2875 (2015).

[91]H. W. de Haan, "Modeling and simulating the dynamics of type IV pili extension of Pseudomonas aeruginosa," Biophys. J. **111**, 2263–2273 (2016).

[92]W. J. Todd, G. Wray, and P. Hitchcock, "Arrangement of pili in colonies of Neisseria gonorrhoeae.," J. Bacteriol. **159**, 312–320 (1984).

[93]M. Klausen et al., "Biofilm formation by Pseudomonas aeruginosa wild type, flagella and type iv pili mutants," Mol. Microbiol. **48**, 1511–1524 (2003).

[94]J. Howard, *Mechanics of Motor Proteins and the Cytoskeleton* (Sinauer Associates, Inc., 2001).

[95]F. Jülicher, "Force and motion generation of molecular motors: A generic description," in *Transport and structure* (Springer, 1999), pp. 46–74.

[96]H. A. Kramers, "Brownian motion in a field of force and the diffusion model of chemical reactions," Physica **7**, 284–304 (1940).

[97]G. I. Bell et al., "Models for the specific adhesion of cells to cells," Science **200**, 618–627 (1978).

[98]E. M. Purcell, "Life at low reynolds number," Am. J. Phys. **45**, 3–11 (1977).

[99]H. H. Tuson et al., "Measuring the stiffness of bacterial cells from growth rates in hydrogels of tunable elasticity," Mol. Microbiol. **84**, 874–891 (2012).

[100]N. Biais et al., "Force-dependent polymorphism in type IV pili reveals hidden epitopes," P. Natl. Acad. Sci. USA **107**, 11358–11363 (2010).

[101]A. Beaussart et al., "Nanoscale adhesion forces of Pseudomonas aeruginosa type IV pili," ACS Nano **8**, 10723–10733 (2014).

[102]D. T. Gillespie, "A general method for numerically simulating the stochastic time evolution of coupled chemical reactions," J. Comput. Phys. **22**, 403–434 (1976).

[103]D. T. Gillespie, "Exact stochastic simulation of coupled chemical reactions," J. Phys. Chem.-US **81**, 2340–2361 (1977).

[104]J Frenkel, "Viscous flow of crystalline bodies under the action of surface tension.," J. Phys. **4**, 385–431 (1945).

[105]J. Eshelby, "Discussion of Paper by AJ Shaler," Trans. AIME **185**, 806 (1949).

[106]E. Flenner et al., "Kinetic Monte Carlo and cellular particle dynamics simulations of multicellular systems," Phys.l Rev. E **85**, 031907 (2012).

[107]B Westling-Häggström et al., "Growth pattern and cell division in Neisseria gonorrhoeae.," J. Bacteriol. **129**, 333–342 (1977).

[108]D. S. Martin, M. B. Forstner, and J. A. Käs, "Apparent subdiffusion inherent to single particle tracking," Biophys. J. **83**, 2109–2117 (2002).

[109]S. A. Safran, *Statistical thermodynamics of surfaces, interfaces, and membranes*, Vol. 90 (Perseus Books, 1994).

[110]P. M. Chaikin and T. C. Lubensky, *Principles of condensed matter physics* (Cambridge University Press, 2000).

[111]Y. Yang and B. B. Laird, "Thermodynamics and intrinsic structure of the Al–Pb liquid–liquid interface: a molecular dynamics simulation study," J Phys. Chem. B **118**, 8373–8380 (2014).

[112]P.-G. De Gennes and J. Prost, *The physics of liquid crystals* (Clarendon Press, 1995).

[113]J.-P. Hansen and I. R. McDonald, *Theory of simple liquids* (Elsevier, 1990).

[114]H. L. Weissberg, "Effective diffusion coefficient in porous media," J. Appl. Phys. **34**, 2636–2639 (1963).

[115]P. S. Stewart, "Diffusion in biofilms," J. Bacteriol. **185**, 1485–1491 (2003).

[116]L. G. Leal, *Advanced transport phenomena: fluid mechanics and convective transport processes* (Cambridge University Press, 2007).

[117]J. C. Mombach et al., "Rounding of aggregates of biological cells: experiments and simulations," Physica A **352**, 525–534 (2005).

[118]S. Douezan and F. Brochard-Wyart, "Active diffusion-limited aggregation of cells," Soft Matter **8**, 784–788 (2012).

[119]C. Stewart and P. Johnson, "Coalescence of viscoelastic latex particles," Macromolecules **3**, 755–757 (1970).

[120]S. Mazur and D. J. Plazek, "Viscoelastic effects in the coalescence of polymer particles," Prog. Org. Coat. **24**, 225–236 (1994).

[121]Y. Lin, C. Hui, and A Jagota, "The role of viscoelastic adhesive contact in the sintering of polymeric particles," J. Colloid. Interf. Sci. **237**, 267–282 (2001).

[122]R. Buscall et al., "Scaling behaviour of the rheology of aggregate networks formed from colloidal particles," J. Chem. Soc. Farad. T. 1 **84**, 4249–4260 (1988).

[123]P. Kollmannsberger and B. Fabry, "Linear and nonlinear rheology of living cells," Annu. Rev- Mater. Res. **41**, 75–97 (2011).

[124]W. Pönisch et al., "Pili mediated intercellular forces shape heterogeneous bacterial microcolonies prior to multicellular differentiation," arXiv preprint arXiv:1703.09659 (2017).

[125]N. Akkiraju et al., "Alpha shapes: definition and software," in Proceedings of the 1st international computational geometry software workshop, Vol. 63 (1995), p. 66.

[126]J. Liang et al., "Analytical shape computation of macromolecules: I. molecular area and volume through alpha shape," Proteins: Structure, Function, and Bioinformatics **33**, 1–17 (1998).

[127]P. L. Townes and J. Holtfreter, "Directed movements and selective adhesion of embryonic amphibian cells," J. Exp. Zool. Part A **128**, 53–120 (1955).

[128]M. S. Steinberg, "Reconstruction of tissues by dissociated cells," Science **141**, 401–408 (1963).

[129]M. S. Steinberg, "Differential adhesion in morphogenesis: a modern view," Curr. Opin. Genet. Dev. **17**, 281–286 (2007).

[130]P. L. Krapivsky, S. Redner, and E. Ben-Naim, *A kinetic view of statistical physics* (Cambridge University Press, 2010).

[131]S. Redner, *A guide to first-passage processes* (Cambridge University Press, 2001).

[132]G. K. Batchelor, *An introduction to fluid dynamics* (Cambridge University Press, 2000).

[133]A. Persat, "Bacterial mechanotransduction," Current opinion in microbiology **36**, 1–6 (2017).

[134]S. Bhat et al., "Viscoelasticity in biological systems: a special focus on microbes," in *Viscoelasticity - from theory to biological applications* (InTech, 2012).

[135]D. A. Caugant et al., "Asymptomatic carriage of Neisseria meningitidis in a randomly sampled population.," J. Clin. Microbiol. **32**, 323–330 (1994).

[136]L. L. Burrows, "Pseudomonas aeruginosa twitching motility: type IV pili in action," Annu. Rev. Microbiol. **66**, 493–520 (2012).

[137]J. C. Conrad et al., "Flagella and pili-mediated near-surface single-cell motility mechanisms in P. aeruginosa," Biophys. J. **100**, 1608–1616 (2011).

[138]Y. Brill-Karniely et al., "Emergence of complex behavior in pili-based motility in early stages of P. aeruginosa surface adaptation," Sci. Rep. **7**, 1–10 (2017).

[139]F. Jin et al., "Bacteria use type IV pili to slingshot on surfaces," P. Natl. Acad. Sci. USA **108**, 12617–12622 (2011).

[140]J. de Anda et al., "High-speed "4d" computational microscopy of bacterial surface motility," ACS Nano (2017) 10.1021/acsnano.7b04738.

[141]W. Burger and M. J. Burge, *Principles of digital image processing* (Springer, 2009).

[142]D. Blair and E. Dufresne, *The Matlab Particle Tracking Code Repository*, (2017) http://site.physics.georgetown.edu/matlab/.

[143]W. Pönisch and V. Zaburdaev, "Relative distance between tracers as a measure of diffusivity within moving aggregates," Eur. Phys. J. B. **91**, 27 (2018).

[144]P. Beckmann, "Rayleigh distribution and its generalizations," J. Res. Natl. Bur. Stand. D **9**, 927–932 (1962).

[145]M. Siddiqui, "Some problems connected with Rayleigh distributions," J. Res. Nat. Bur. Stand. D **60**, 167–174 (1962).

[146]N. Wax, *Selected papers on noise and stochastic processes* (Dover Publications, 1954).

[147]I. N. Bronshtein and K. A. Semendyayev, *Handbook of mathematics* (Springer Science & Business Media, 2013).

VERSICHERUNG

Hiermit versichere ich, dass ich die vorliegende Arbeit ohne unzulässige Hilfe Dritter und ohne Benutzung anderer als der angegebenen Hilfsmittel angefertigt habe; die aus fremden Quellen direkt oder indirekt übernommenen Gedanken sind als solche kenntlich gemacht. Die Arbeit wurde bisher weder im Inland noch im Ausland in gleicher oder ähnlicher Form einer anderen Prüfungsbehörde vorgelegt.
Die vorliegende Arbeit wurde im Zeitraum zwischen November 2013 und September 2017 unter der Betreuung durch Dr. Vasily Zaburdaev am Max-Planck-Institut für Physik komplexer Systeme in Dresden angefertigt.
Ich versichere, dass ich bisher keine erfolglosen Promotionsverfahren unternommen habe. Ich erkenne die Promotionsordnung der Fakultät der Mathematik und Naturwissenschaften der Technischen Universität Dresden an.

Dresden, 2018

Wolfram Pönisch